ABSTRACT

Title of Dissertation: THE IMPACT OF MARSH SILL LIVING SHORELINES ON COASTAL RESILIENCE AND STABILITY: INSIGHTS FROM MARYLAND'S CHESAPEAKE BAY AND COASTAL BAYS

Limin Sun, Doctor of Philosophy, 2024

Dissertation directed by: Dr. William Nardin, UMCES
Dr. Cindy M. Palinkas, UMCES

Climate change and coastal urbanization are accelerating the demand for strategies to reduce shoreline erosion and enhance coastal resilience to storms and sea-level rise. Generally adverse ecological impacts of hardened infrastructure (e.g., seawalls, revetments, and dikes) have led to growing interest in alternative solutions. Living shorelines, increasingly recognized as sustainable Natural and Nature-Based Features (NNBFs; or Nature-Based Solutions (NBSs)) for their dual benefits of stabilizing shorelines while preserving or restoring coastal habitats, represent a promising approach to shoreline stabilization. Marsh sill living shorelines (created marshes with adjacent rock sills) have been extensively constructed in the Chesapeake Bay, notably in Maryland. Despite their popularity, significant uncertainties remain regarding their effectiveness and resiliency, especially during high-energy events. This dissertation investigates the dynamics of marsh sill living shorelines in Maryland's Chesapeake Bay and Coastal Bays, aiming to fill knowledge gaps and inform effective shoreline stabilization strategies.

First, the dissertation examines marsh boundary degradation into open water during high-energy conditions, contrasting mechanisms between living shorelines and natural marshes. Field surveys and numerical modeling reveal that while natural marshes experience erosion through undercutting and slumping at the scarp toe, living shorelines degrade primarily through open-water conversion at the marsh boundary behind rock sills. Differences in sediment characteristics and vegetation between the two ecosystems drive variations in marsh boundary stability between them. Next, the study assesses the impacts of rock sill placement on sediment dynamics and shoreline stability, highlighting the role of tidal gaps in enhancing sediment flux to the marsh and increasing vertical accretion during high-energy events. Numerical modeling demonstrates that while continuous sills mitigate erosion at the marsh edge of living shorelines, they diminish sediment deposition on the marsh platform compared to segmented sills with tidal gaps. Finally, the research identifies key factors driving marsh boundary degradation that are needed to assess the stability of marsh sill living shorelines. Analysis of eco-geomorphic features and hydrodynamics across 18 living shoreline sites reveals that metrics such as the Unvegetated/Vegetated Ratio (UVVR) and sediment deposition rate often used to assess the resilience of natural marshes also apply to the created marshes of living shorelines. Multivariate analyses further reveal that the Relative Exposure Index (REI) and Gap/Rock (G/R) ratio are crucial predictors of shoreline stability in marsh sill living shorelines, and thus should be particularly considered in shoreline design. By integrating remote sensing, field observations, and numerical modeling, this dissertation advances the understanding of sediment dynamics and stability in living shorelines and provides actionable insights for effective shoreline design and management to promote coastal resilience.

# THE IMPACT OF MARSH SILL LIVING SHORELINES ON COASTAL RESILIENCE AND STABILITY: INSIGHTS FROM MARYLAND'S CHESAPEAKE BAY AND COASTAL BAYS

by

Limin Sun

Dissertation submitted to the Faculty of the Graduate School of the
University of Maryland, College Park, in partial fulfillment
of the requirements for the degree of
[Doctor of Philosophy]
[2024]

Advisory Committee:
Dr. William Nardin, Co-chair
Dr. Cindy M. Palinkas, Co-chair
Dr. Jeffery Cornwell
Dr. Lorie W. Staver
Dr. Karen L. Prestegaard, Dean’s Representative

# Acknowledgments

I am so grateful to my advisors, Dr. Cindy M. Palinkas and Dr. William Nardin, who inspired my work, and guided me through my PhD at the University of Maryland. Equal appreciation goes to all of my committee members, Dr. Jeffery Cornwell, Dr. Lorie W. Staver, Dr. Karen L. Prestegaard, and Dr. Neil K. Ganju.

A lot of thanks to graduate students and faculties from Horn Point Lab, including Iacopo Vona, Kerria Burns, Ben Malmgren, John McDonald, Meg Maddox, Erika Koontz, Anji Cooper, Julia Charest, Taylor Gordon, and Amanda Schwark for their help with the field surveys and sampling as well as associated laboratory analyses. I would also like to thank all the professors who shared their knowledge in my classes, the maintenance and administrative staff, as well as all the other HPL people who kindly helped me at work and in life.

Special thanks to my lovely roommates, Kerry, Squeaks, and Felina, and to Marshall, Riley, and Otto, who have made our home a place of warmth and companionship for the past three years.

To my dearest family and friends in China, your unwavering support means the world to me.

I deeply appreciate everyone who has been part of this journey.

# Table of Contents

# List of Tables

# List of Figures

Figure 2.5. Comparison of sediment characteristics (grain size, organic matter content, and $^{7}$Be-derived sediment deposition rate; a, b, and c) and vegetation characteristics (stem height, diameter and density; d, e, and f) between the living shoreline (red) and natural marsh (blue) from 2021 to 2022.

Figure 2.6. Comparison of measured and modeled hydrodynamic conditions, output from 23 February to 1 March 2023: (a) wind speed and direction, (b) measured water levels and astronomical tides at the Ocean City Inlet from NOAA station; (c) water level, (d) significant wave height (Hs), and (e) total suspended sediment concentration (SSC).

Figure 2.7. Spatial distribution of modeled hydrodynamic conditions and morphology change in the marsh along cross-section with distance to living shoreline marsh edge: (a) water level (m), (b) velocity (m/s), (c) bed shear stress ($N/m^2$), (d) cumulative erosion/sedimentation (m; negative is erosion and positive is deposition). Each circle is a data point and is transparent gray; darker colors indicate overlapping circles.

Figure 2.8. (a) Cumulative distribution of high-energy events during the simulation (proportion of time when the wind speed is higher than 8 m/s; arrows indicate the dominant wind direction at each high-energy event with north pointing upward); (b) Modeled results of cumulative sediment flux to marsh ($kg/m^2$; left y-axis) and erosion area ($m^2$; right y-axis) of the living shoreline marsh.

Figure 2.9. Scenario analysis of sediment dynamics in the living shoreline: total sediment flux to marsh (a) and cumulative erosion/deposition (b) with vary height of the rock sill to mean water level (-0.1 to -0.05 m); total sediment flux to marsh (c)

at CG, (e) Segmented sill living shoreline with fragmenting marsh at IC, (f) Segmented sill living shoreline with dune at AS. The green zone represents the unvegetated area, and the white zone indicates the vegetated area. Base satellite images are sourced from Google Earth Pro.

Figure 4.3. Sediment deposition rate (mm/y) in relation to (a) Elevation relative to Mean Sea Level (MSL, m), (b) Relative Tidal Marsh Elevation ($Z^*_{MHW}$, m), (c) Total Suspended Matter (TSM, mg/L), and (d) Unvegetated/Vegetated Ratio (UVVR). Different colors correspond to different rates of sea level rise (mm/y).

Figure 4.4. Relationship between functional marsh width ($W^*$, m) and the difference between the sediment deposition rate and the Rate of relative Sea-Level Rise (RSLR; mm/y). (a) Scatter plot illustrating the relationship between $W^*$ and the difference between the sediment deposition rate and RSLR. (b) Relationship between $W^*$ and the difference between the sediment deposition rate and RSLR when the sediment deposition rate exceeds the RSLR. (c) Relationship between $W^*$ and the difference between the sediment deposition rate and RSLR when the sediment deposition rate is below the RSLR. Different colors represent varying Gap/Rock ratios.

Figure 4.5. Non-metric multi-dimensional scaling analyses for 18 living shorelines with representative variables including Gap/Rock (G/R) ratio, Elevation relative to Mean Sea Level (m), Sand percentage (%), Relative Exposure Index (REI), Stem density (num/m$^2$), and Deposition rate (mm/y). * $p < 0.05$.

Figure S4.1. (a) Relationship between the Unvegetated/Vegetated Ratio (UVVR) and Sediment Deposition Rate (mm/y) excluding the outlier site, QL. (b) Relationship

between UVVR and Sediment Deposition Rate for sites with UVVR > 0. (c) Relationship between UVVR and Sediment Deposition Rate for sites with segmented sills. Different colors indicate different rates of sea level rise (mm/y).

Figure S4.2. (a) Non-metric multi-dimensional scaling analysis for 18 living shorelines with representative variables including Gap/Rock (G/R) ratio, Sand percentage (%), Relative Exposure Index (REI), Stem density (num/$m^2$), and Deposition rate (mm/y); (b) Non-metric multi-dimensional scaling analysis for 18 living shorelines with representative variables including Elevation relative to Mean Sea Level (m), Sand percentage (%), REI, Stem density (num/$m^2$), and Deposition rate (mm/y).

# List of Abbreviations

| | |
|---|---|
| ADCP | Acoustic Doppler Current Profiler |
| ANOSIM | Analysis of Similarity |
| AS | Assateague State Park |
| $A_v$ | Vegetated marsh area |
| BRT | Bagged regression tree |
| CG | Conrad Gordon |
| CPs | Check Points |
| DJI-P3P | DJI Phantom 3 Professional |
| DTMs | Digital Terrain Models |
| EC | Environmental Concern |
| $F_i$ | Effective fetch (m) for the i-th direction |
| FWHM | Full-Width Half-Maximum |
| Gap/Rock (G/R) ratio | The ratio of total gap length to total rock sill length |
| $G_b$ | The gap between breakwater units |
| GCPs | Ground Control Points |
| GNSS | Global Navigation Satellite System |
| GPS | Global Positioning System |
| HG | Hatton Garden |
| IC | Irish Creek |
| $L_b$ | Breakwater length |
| $L_s$ | Total length of the shorelines |

| | |
|---|---|
| $L_{sed}$ | Sediment-based lifespan |
| MD | Maryland |
| MG | Myrtle Grove |
| MHW | Mean High Water |
| MM | Maritime Museum |
| MODIS | Moderate Resolution Imaging Spectroradiometer |
| MSL | Mean Sea Level |
| MTL | Mean Tide Level |
| NAIP | National Agriculture Imagery Program |
| NBSs | Nature-Based Solutions |
| NIR | Near-infrared wavelengths |
| NMDS | Non-metric Multidimensional Scaling |
| NNBFs | Natural and Nature-Based Features |
| NOAA | National Oceanic and Atmospheric Administration |
| NP | Narrows Pointe |
| OP | Oppenheim |
| OT | Old Trinity Church |
| PC | Plaindealing Creek |
| $Q_b$ | Marsh sediment budget |
| QL | Queens Landing |
| $r$ or $R^2$ | Coefficient of determination |
| REI | Relative Exposure Index |
| RMSE | Root Mean Square Error |

| | |
|---|---|
| RSLR | Rate of relative Sea-Level Rise |
| RTK | Real-Time Kinematic |
| RU | Ruesch |
| SAV | Submersed Aquatic Vegetation |
| SD | San Domingo |
| SfM | Structure from Motion |
| SI | Sunset Island |
| SIMPER | Similarity Percentages |
| SSC | Suspended Sediment Concentration |
| TA | Tred Avon |
| $T_i$ | Proportion of time that the wind blew from the *i*-th direction |
| TSM | Total Sediment Matter |
| USGS | U.S. Geological Survey |
| UVVR | Unvegetated/Vegetated Ratio |
| VCR | Virginia Coast Reserve |
| $V_i$ | The average annual wind speed |
| VPs | Validation Points |
| $W^*$ | Functional Marsh Width |
| WHE | Wye House East |
| WHW | Wye House West |
| WVI | Wetland Vulnerability Index |
| $Z^*_{MHW}$ | Relative tidal marsh elevation |

# Chapter 1: Introduction

The degradation of coastal habitats and intensive urbanization along coastlines have accelerated the need for strategies to reduce shoreline erosion and enhance coastal resilience to storms and sea-level rise (Gittman et al., 2016; Kirezci et al., 2020). Traditional hardened structures, such as seawalls, revetments, and dikes, have been widely constructed for shoreline erosion control (Dugan et al., 2011), with 14% of the shorelines in the continental US having been hardened by 2005 (Gittman et al., 2015). In the Chesapeake Bay, where the relative sea level rise (4.5-6.1 mm/y) exceeds the global average (Ezer, 2023), approximately 25% of coastal shorelines were hardened by the early to mid-2000s, with some sub-watersheds having over 50% hardened shorelines (Patrick et al., 2014). However, these structures are costly to maintain and can negatively impact intertidal and nearshore habitats (Bilkovic and Mitchell, 2013; Prosser et al., 2018). Negative effects include the elimination of habitat connectivity across the land-water interface (Isdell et al., 2015), wave reflection and associated scouring (Nordstrom and Jackson, 2012), increased water depth (Dugan et al., 2011), sediment starvation, and loss of intertidal habitat (Mariotti and Carr, 2014; Currin et al., 2015). These impacts contribute to reduced water quality, wetland habitat, fisheries, and wildlife (Currin, 2019), prompting growing interest in exploring alternative solutions.

### *1.1. Living Shorelines as Alternative Solutions to Shoreline Stability*

More recently, a variety of approaches using natural and nature-based features (NNBFs; also referred to as nature-based solutions (NBSs)), including salt marshes, mangroves, seagrasses, dunes, coral reefs, oyster reefs, tidal flats, and rock sills (Arkema et al., 2013; Firth et al., 2014; French, 2008; Koch et al., 2009; Shipman,

2009; Temmerman et al., 2013), have emerged as viable options for stabilizing shorelines while preserving coastal ecosystem functions (Sutton-Grier et al., 2015). Living shorelines are a type of NNBF commonly used in temperate ecosystems, consisting of created fringing marshes often accompanied by rock sills, oyster reefs, tidal flats, and other features (Currin, 2019). These living shorelines can occur naturally or be engineered, constructed, and/or restored to mimic natural conditions (Currin, 2019). This approach has been in use for several decades, gaining momentum and spreading nationwide due to its dual benefits of shoreline stabilization and habitat creation (Miller et al., 2022).

Marsh sill living shorelines, consisting of constructed fringing marshes with adjacent rock sills, are a preferred type of NNBF for sites with low to moderate erosion rates (Miller et al., 2022; Polk et al., 2022). This approach has been widely implemented in the Chesapeake Bay since the mid-1980s, particularly in Maryland (Hardaway Jr et al., 2017). The Chesapeake Bay Foundation (2007) recommends marsh sill living shorelines for sites with erosion rates of approximately 0.2 to 0.7 m/y. Sills are typically low-crested structures with a freeboard constructed parallel to the shoreline, then backfilled with clean sand to achieve a suitable height and slope for planted tidal marsh vegetation (Miller et al., 2022). Sill height is generally at or slightly above Mean Tide Level (MTL; Hardaway Jr et al., 2017) but below Mean High Water (MHW) to minimize interruption of tidal exchange. Their effectiveness in living shorelines depends significantly on the relative crest width and height, with wider and higher sills attenuating more waves and providing better shore erosion control

(Hardaway Jr et al., 2017). The width of the marsh developing behind the sill structure determines the extent of additional wave energy dissipation. Hardaway and Byrne (1999) recommend a minimum width of approximately 9 to 21 m for low to moderate energy sites. Generally, a wider intertidal zone enhances the marsh's ability to dissipate wave energy (Miller et al., 2022). For small waves, 50% of their energy is dissipated within the first approximately 2.4 m of marsh, and 100% is dissipated within about 30 m (Knutson et al., 1982). Bed shear stress and velocity are notably higher within 5 m of the marsh edge of a micro-tidal living shoreline (Sun et al., 2024). While overall gentle slopes are preferred, slopes between 1/8 and 1/10 have been identified as optimal for drainage purposes (Hardaway et al., 2010). Priest (2006) advises against areas of standing water larger than approximately 10 $m^2$ to prevent drowning and dieback of marsh vegetation. In the Chesapeake Bay, *Spartina alterniflora* (smooth cordgrass) typically dominates the low marsh of living shorelines, while *Spartina patens* (marsh hay cordgrass) and *Phragmites australis* are common species in the high marsh of living shorelines (Miller et al., 2022).

Although generally effective at wave attenuation and erosion control, sill placement along the marsh edge has been reported to impact the benthic habitat underneath the structure by obstructing the exchange between the intertidal and subtidal zones (Bilkovic et al., 2016). In recent years, marsh sill living shorelines with tidal gaps, also referred to as tidal openings or windows, through the sills have been encouraged to enhance hydrological connectivity (Smith, 2006) and allow access for marine fauna (e.g., fish and turtles) to the created marsh (Hardaway Jr et al., 2017; Miller et al.,

2022). While tidal water can access the intertidal marsh behind a continuous sill through pore spaces or via overtopping (Hardaway Jr et al., 2017), gaps allow for additional tidal water exchange, wave energy transmission, and sediment transportation between intertidal and subtidal environments. Segmented sills are usually oriented perpendicular to the dominant incoming wave direction to maximize effectiveness. If waves come from multiple directions, chevron-shaped structures or staggered zig-zag structures can be used (Miller et al., 2022). A special type of segmented sill living shoreline is the headland breakwater, characterized by tombolos or salients with a marsh or sandy beach behind. The formation of these features depends on the length of the structure ($L_b$), the spacing between the structures ($G_b$), and the distance to the shoreline ($X_b$). Tombolos are more likely to form when headland breakwaters are closer to shore, and the gaps between adjacent structures are smaller (Hardaway, 1999). When the $L_b$:$G_b$ ratio is greater than 1:2, conditions favor tombolo formation; when the $L_b$:$G_b$ ratio is less than 1, conditions favor salient formation (US Army Corps of Engineers, 2002). Guidelines suggest gaps at least every 30 m (Hardaway et al., 2010) and an $L_b$:$G_b$ ratio of about 1:1.0 to 1:1.5 for headland breakwaters (Hardaway and Gunn, 2002). However, limited research has been performed to determine the optimum tidal gap width and frequency.

### *1.2 Living Shorelines for Enhancing Coastal Resilience*

Shoreline erosion and sediment deposition, as contrasting influences on marsh resilience to sea-level rise and high-energy storm events, have been well-addressed in previous research. In coastal tidal marshes, sea-level rise changes the location and characteristics of breaking waves (Miller et al., 2022), contributing to different

morphological dynamics. Natural marshes with jagged boundaries and steep slopes from the intertidal to the subtidal zones are susceptible to frontal erosion caused by wave-induced undercutting and subsequent collapse at the scarp (Fagherazzi et al., 2013). Salt marsh frontal erosion alters the export of sediments (Li et al., 2019; 2018). For coastal fringing marshes, lateral edge erosion is an important source of sediments for vertical marsh accretion, allowing the marsh platform to maintain elevation at the expense of the total marsh area (Hopkinson et al., 2018). This can lead to open-water conversion, a primary destructive process in marshes, influencing the long-term fate of marsh complexes (Ganju et al., 2017). Therefore, for some marshes that have already lost significant areas of vegetation, sediment accretion and subsequent elevation gain can be symptoms of instability (Ganju et al., 2015), not drivers of stability.

A significant supply of suspended sediment to marshes is necessary to promote sufficient sediment deposition on intertidal marshes to keep pace with sea-level rise (Ganju et al., 2017). High-energy storm events can significantly increase suspended sediment supply to microtidal marshes, enhance marsh deposition, and build up vertical elevation (Wiberg et al., 2020). At the Virginia Coast Reserve (VCR), storm surge events occurred 5% of the time but contributed 40% of marsh deposition from 2009 to 2020 (Zhu and Wiberg, 2022). Castagno et al. (2018) have indicated that intense storms increase the stability of tidal bays by providing the sediment necessary to counteract sea-level rise.

Previous studies have explored the effectiveness of marsh sill living shorelines in mitigating shoreline erosion and enhancing coastal resilience. Numerical modeling research has demonstrated that rock sills contribute positively to sediment balance in created marshes, stabilizing bed levels and shorelines, particularly during extreme events (Vona et al., 2020). Marsh sill living shorelines across North Carolina have shown superior performance compared to hardened shorelines, enhancing marsh resilience to hurricanes by reducing structural damage (Smith et al., 2018) and erosion of fringing salt marshes, as well as promoting lateral shoreline buildup during short-term disturbance events (Polk et al., 2022). In the mesohaline Chesapeake Bay, living shoreline installations can even expand the shoreline seaward, countering historical erosion effects in the long term (Palinkas et al., 2023). However, the effectiveness of living shorelines can be site-specific. Measurements at shallow bays on the seaward side of the southern Delmarva Peninsula in Virginia, USA suggested that fringing oyster reefs can reduce the wave energy reaching the shoreline of marshes with edge elevations close to mean sea level, but have little effect on waves during deeper water conditions (Wiberg et al., 2019). Field observations of living shorelines in upper Delaware Bay indicated that constructed oyster reefs (CORs) only provide partial attenuation of wave energy due to the large tidal range (> 2 m) and significant wind waves and swell energy originating from the Atlantic Ocean (Zhu et al., 2020). A survey of 17 living shorelines (some with rock sills and some with oyster bag sills) in North Carolina indicated that 12 experienced a reduction in erosion rates, with half of those 12 also showing signs of accretion (Polk and Eulie, 2018). Site-specific effectiveness associated with structures can be predicted using

multiple linear regression models that consider structure type, shoreline erosion rate, dominant sediment source, and land use (Palinkas et al., 2018).

The effectiveness of sills diminishes over time due to rising sea levels, which gradually reduce the freeboard of the structure (Miller et al., 2022). Recent research indicates that accelerated sea-level rise has caused mature marsh sill living shoreline boundaries to convert into open water as ponds expand landward of rock sills, negatively impacting coastal marsh resilience and shoreline stability (Sun et al., 2024). The addition of tidal gaps in rock sills enhances tidal flushing and eco-hydrological connectivity (Miller et al., 2022), potentially altering erosion or accretion at the created marsh. Field observations in segmented sill living shorelines have revealed shoreline scouring behind gaps, attributed to wave penetration at these points (Hardaway et al., 2010). However, the impacts of rock sill placement, either with or without tidal gaps, on shoreline erosion and sediment deposition in the living shorelines remain unclear.

### *1.3 Numerical Modeling with Living Shorelines*

Numerical models are essential for simulating the hydrodynamics and morphodynamics around living shorelines. Over the past decades, multiple models have been developed that integrate marsh vegetation dynamics with hydrodynamic and sedimentation processes. These models have been applied to both actual sites and idealized tidal basins featuring coastal tidal marshes. For instance, Nardin and Edmonds (2014) employed Delft3D to simulate sediment deposition in the Wax Lake Delta, exploring the optimal vegetation height and density for inorganic

sedimentation in deltaic marshes. Similarly, Alizad et al. (2016) developed a model for salt marshes in northeast Florida that couples the interactions between hydrodynamics and vegetation dynamics. Mariotti and Canestrelli (2017) integrated shallow-water hydrodynamics with the wind-wave model (Delft3D-FLOW-WAVE) to simulate the long-term (3,000-year) morphodynamics of an idealized muddy back-barrier tidal basin. Xu et al. (2021) further developed the vegetation-hydrodynamic-morphological modeling system in COAWST to study marsh establishment. Some models have focused on marsh channel networks (van Maanen et al., 2015; Fleri et al., 2019). Others have utilized Delft3D-SWAN to explore the impact of waves on coastal morphology (Nardin et al., 2020, 2013; Nardin and Fagherazzi, 2018). More recently, Delft3D-SWAN has been applied to investigate both the independent and synergistic effects of salt marsh vegetation and seagrass (Nardin et al., 2018; Vona et al., 2021; Zhu and Wiberg, 2024).

Several studies have utilized physics-based numerical models to simulate hydrodynamics and morphodynamics in living shorelines. Vona et al. (2020) employed Delft3D-SWAN to investigate the effects of breakwaters on the wave damping and sediment dynamics at an adjacent marsh in the Chesapeake Bay. Wang et al. (2022) developed models that combine fully connected neural networks with long short-term memory to estimate wind-wave characteristics across constructed oyster reefs. Zhu et al. (Zhu et al., 2023) integrated Delft3D-SWAN with a bagged regression tree (BRT) machine learning algorithm to simulate wave dynamics at an oyster reef living shoreline in upper Delaware Bay. Additionally, Vona and Nardin

(2023) used Delft3D-SWAN to assess the performance of breakwater structures coupled with oysters in coastal shoreline protection. While these physics-based models generally yield satisfactory results, their application to real-world living shorelines faces several challenges. These include limited spatial and temporal resolution, imprecise descriptions of initial and boundary conditions (Kissas et al., 2020), time-consuming computations due to nested domains, and the complex generation of computational meshes for intricate geometries (Wang et al., 2022).

### *1.4. Assessment of Coastal Tidal Marsh Resilience*

The assessment of ecosystem resilience in marsh sill living shorelines is vital for guiding shoreline design and enhancing coastal management strategies. Researchers have developed various biotic and abiotic methods to gauge the vulnerability of natural tidal marshes. Sediment availability is a major control of intertidal marsh resilience to sea level rise (Ganju et al., 2017) and the success of marsh restoration (Liu et al., 2021). Donatelli et al. (2020) highlight that a decline in regional marsh area can lead to reduced sediment availability in coastal estuarine systems. Ganju et al. (2017) identify sediment deficits and the transition of marsh to open water as comprehensive and sensitive indicators of salt marsh vulnerability. Furthermore, the marsh sediment budget ($Q_b$) acts as a spatially integrated metric that reflects the balance of constructive and destructive forces affecting sediment dynamics (Ganju et al., 2017). At the landscape scale, both $Q_b$ and the sediment-based lifespan ($L_{sed}$) correlate with the ratio of unvegetated to vegetated marsh areas (UVVR), indicating their usefulness in predicting marsh trajectories (Ganju et al., 2017). Additionally, Ganju et al. (2020) observed a consistent scaling of elevation with UVVR across

different systems, where units with lower elevations are more prone to open-water conversion and exhibit higher UVVRs.

While various metrics provide insights into marsh trajectories, no single metric can universally predict the marsh trajectories. Wasson et al. (2019) introduced a robust approach that combines multiple spatially integrated, landscape-scale metrics, acknowledging the complexity of marsh ecosystems. Building on this, Defne et al. (2020) created a geospatially resolved wetland vulnerability index (WVI), which uses ranked values from different datasets to highlight areas of relative vulnerability across landscapes. Despite these advances, there remains a gap in the research concerning the application of these metrics to specifically assess and predict the trajectories of created marshes in marsh sill living shorelines.

### *1.5. Dissertation Objectives and Layout*

Recently, field observations and aerial imagery have suggested that the boundaries of some mature living shorelines, including both continuous and segmented sills, are deteriorating into open water. Therefore, understanding the physical mechanisms that drive shoreline erosion and sediment accretion at living shorelines is critical for predicting their effectiveness and long-term performance. This dissertation aims to enhance our understanding of the physical mechanisms influencing shoreline dynamics in marsh sill living shorelines and to provide references to promote the practical design of nature-based coastal defenses. Below is an outline of the main chapters planned for this dissertation.

Chapter 2 explores processes at the marsh edges of a rock-sill living shoreline (installed in 2007) and an adjacent natural marsh during a strong wind event at Sunset Island in Ocean City, MD. The main goals are to (1) determine the nature and likely cause of changes at the marsh edge in both the living shoreline and natural marsh, and (2) explore the role of sill height in preventing marsh degradation in living shorelines. This study improves our understanding of the performance of rock sill living shorelines during energetic conditions and provides a reference for coastal managers and regulatory agencies to enhance coastal resilience in facing sea-level rise.

Chapter 3 compares sediment dynamics within the created marshes of two marsh sill living shorelines (one with a continuous sill and one with tidal gaps) to those in a natural marsh adjacent to one of the living shorelines in Ocean City, Maryland, USA. We use both field and numerical modeling approaches to address the main goals of (1) assessing elevation patterns within each study site over a ~1-year period, and (2) exploring differences in sediment transport that arise from gaps in the rock sill. This study improves our understanding of sediment dynamics in marsh sill living shorelines and provides references for the practical design of tidal gaps.

Chapter 4 integrates remote sensing and field sampling data from 18 marsh sill living shorelines (9 with continuous sills and 9 with segmented sills) in Maryland to evaluate marsh stability. We analyzed 15 metrics used to characterize eco-geomorphic features and hydrodynamic conditions of tidal marshes, comparing them between different sill types (continuous versus segmented) and ponding conditions

(with ponding versus no ponding). Additionally, we introduced a novel metric, Functional Marsh Width ($W^*$, in m), to describe the vegetation distribution of the narrow fringing marsh band in living shorelines. The primary objectives of this study are: (1) to evaluate the applicability of potential metrics for assessing the stability of fringing marshes in marsh sill living shorelines, and (2) to investigate the main drivers of potential degradation in marsh sill living shorelines. This research advances our understanding of metrics for assessing the stability of marsh sill living shorelines and improves our insight into their post-construction trajectory.

# Chapter 2: Marsh Boundary Degradation into Open-water in Living Shorelines under High-Energy Conditions

*Sun, L., Palinkas, C.M., Nardin, W., 2024. Marsh boundary degradation into open-water in living shorelines under high-energy conditions. Ecological Engineering 202, 107232.*

***Abstract***

Living shorelines have been recognized for their potential to attenuate wave energy, reduce shoreline erosion, and enhance coastal resilience, and are gaining traction as a preferred method of shoreline stabilization. Yet much remains uncertain about their resiliency and effectiveness in reducing shoreline erosion during high-energy events. This study examines sediment dynamics at a relatively mature living shoreline (constructed in 2007 and comprised of a created marsh and rock sill at the land/water interface) in the Maryland Coastal Bays (USA) during a storm event via field surveys and numerical modeling. Results are evaluated within the context of observations at an adjacent natural marsh. Our study demonstrates that the mechanisms of marsh loss at the edge during these times differ between the living shoreline and natural marsh. Specifically, the living shoreline boundary is degraded through open-water conversion as ponds expand landward of the rock sills, but the natural marsh is eroded by undercutting at the scarp toe, triggering slumping and edge collapse. Sediments in the living shoreline marsh have larger particle sizes and lower organic content than in the natural marsh; vegetation has higher stem heights and lower stem densities compared to the natural marsh. These differences may drive differences in the stability of the marsh boundary. Numerical modeling indicates that bed shear stresses are higher landward of the rock sill at the edge of the vegetation in the living shoreline. This increase in shear stress under high-energy conditions occurs at both flood and ebb tide, potentially contributing to scouring and/or open-water conversion, as well as substantial sediment transport between the subtidal zone and the marsh platform of the living shoreline. Increasing the bank height (both sill and marsh) may

reduce erosion at the marsh edge and/or prevent open-water conversion but should be carefully balanced with marsh ecology and processes during other times of the year.

**Keywords:** Living shoreline; Marsh degradation; Open-water conversion; Sediment erosion; Nature-based solution; Delft3D

## *2.1. Introduction*

Degradation of coastal habitats and continuous population growth along coastlines have led to increasing efforts to bolster coastal resilience to high-energy storms and sea level rise (Smith et al., 2018; Gitmann et al., 2016). In the past, hardened structures, including bulkheads, revetments, seawalls, and breakwaters, were extensively constructed along coastal shorelines to protect against erosion and enhance resistance to storms (Dugan et al., 2011) with 14% of shorelines in the continental US being hardened by 2005 (Gittman et al., 2015). In the Chesapeake Bay, where relative sea level rise (4.5-6.1 mm/y) is higher than global average (Ezer 2023), ~25% of coastal shorelines were hardened by the early-mid 2000s, with shorelines in some subwatersheds being >50% hardened (Patrick et al., 2014). However, these "hard" approaches have many negative impacts on coastal wetlands, including the elimination of habitat connectivity across the land-water interface (Isdell et al., 2015), wave reflection and associated scouring (Nordstrom and Jackson, 2012), increased water depth (Dugan et al., 2011), and sediment starvation and loss of intertidal habitat (Mariotti and Carr, 2014; Currin et al., 2015), all of which contribute to reduced water quality, wetland habitat, fisheries, and wildlife (Currin, 2019).

More recently, living shorelines have been promoted as a nature-based approach for coastal communities that integrates natural features to mitigate coastal erosion. In temperate coastal ecosystems, living shorelines are primarily characterized by created marshes with or without additional rock sills, oyster reefs, tidal flats, and seagrasses (Currin, 2019). A few studies have adopted physics-based numerical models to simulate coastal and estuarine hydrodynamics and morphodynamics in living shorelines. Vona et al. (2021) used Delft3D-SWAN to simulate sediment transport between the created saltmarshes of the living shorelines and adjacent submersed aquatic vegetation (SAV) in a sub-estuary of Chesapeake Bay. Wang et al. (2022) developed soft computing-based models combining fully connected neural networks and long short-term memory to estimate the wind-wave characteristics across constructed oyster reefs. Zhu et al. (2023) combined Delft3D-SWAN and bagged regression tree (BRT) machine learning algorithm to simulate wave dynamics at an oyster reef living shoreline in upper Delaware Bay. Although the physics-based models generally provide satisfactory results, application of these models to real-world living shorelines encounters some challenges, including limited spatial and temporal resolution, lack of precision in the description of initial and boundary conditions (Kissas et al., 2020), time-consuming computation caused by nested domains, and the cumbersome generation of computational meshes for complicated geometries (Wang et al., 2022).

Marsh sill living shoreline which is composed of a created marsh with an adjacent rock sill, has been a popular approach to reduce shoreline erosion, especially in

Maryland (Hardaway Jr and Duhring, 2010). Sills are usually located near the low tide line, then backfilled with clean sand to create a suitable elevation and slope for planted tidal marsh vegetation. The height of the rock sill is generally at or a little above Mean Tide Level (MTL; Hardaway, 2017), but below Mean High Water (MHW) to minimize interruption of tidal exchange. Marsh sill living shorelines have been widely acknowledged to reduce shoreline erosion, preserve estuarine habitats and restore the ecosystem functions of coastal wetlands (Sutton-Grier et al., 2015; Currin, 2019). During high-energy storm events, marsh sill living shorelines exhibited better resistance to landward erosion than hardened shorelines by promoting vertical accretion and experiencing less damage (Smith et al. 2018; Polk et al. 2022). The rock sills contributed to a positive sediment balance in the created marshes over scales of years to decades, stabilizing bed level and shorelines, especially in the presence of adjacent SAV (Vona et al., 2021). Moreover, a series of field observations on ~10-year-old marsh sill living shorelines in mesohaline Chesapeake Bay suggested that rock sills can effectively reduce shoreline erosion at long term by extending the shoreline seaward without any systematic changes to the adjacent subtidal habitat (Palinkas et al., 2023). But the effectiveness of living shorelines can be site-specific. Polk and Eulie (2018) surveyed 17 rock sill living shorelines along North Carolina coasts and found that 6 sites exhibited a reduction in the erosion rate and 6 sites exhibited accretion. Therefore, there is no consensus on the performance of marsh sill living shorelines as the efficacy of a sill will diminish over time as sea-level rise gradually reduces the freeboard of the structure (Miller et al., 2022).

Previous research on natural marshes have suggested that sea-level rise changes the location and characteristics of the breaking waves (Miller et al., 2022), contributing to different morphological dynamics. Natural marshes with jagged boundaries and steep slopes from the intertidal to the subtidal are susceptible to frontal erosion caused by wave-induced undercutting and subsequent collapse at the scarp (Fagherazzi et al., 2013). Salt marsh frontal erosion alters the export of sediments (Li et al., 2018; 2019), but the marsh platform can maintain elevation at the expense of total marsh area (Hopkinson et al., 2018). High-energy storm events have the potential to significantly increase suspended sediment flux to microtidal marshes and build up the vertical elevation (Wiberg et al., 2020). At the Virginia Coast Reserve (VCR), storm surge events occurred 5% of the time, but contributed 40% of marsh deposition during 2009–2020 (Zhu et al., 2022). Recently, some field and imagery evidence has shown that marsh boundary is degrading into open-water at some mature living shorelines. Therefore, understanding the physical mechanisms that control erosion or accretion at the marsh boundary is thus critical for predicting their performance, especially during high-energy extreme events.

This study explores processes at the marsh edges of a rock-sill living shoreline (installed in 2007) and an adjacent natural marsh during a strong wind event at Sunset Island in Ocean City, MD. The main goals are to (1) determine the nature and likely cause of changes at the marsh edge in both the living shoreline and natural marsh, and (2) explore the role of sill height in preventing marsh degradation in living shorelines. This study improves our understanding of the performance of rock sill living

shorelines during energetic conditions and provides a reference for coastal managers and regulatory agencies to enhance coastal resilience in facing sea-level rise.

## *2.2. Methods*

### 2.2.1. Study Site

Our study site was located at Sunset Island in Ocean City, MD, near the boundary between Assawoman and Isle of Wight Bays, and just upstream of the St. Martin River (Figure 2.1a and b). The Bays are micro tidal coastal lagoons and are contiguous with each other (Wells et al., 1994; 2002). Tidal range near the Ocean City Inlet is more than 1.04 m, while it drops to 0.46 m in Assawoman Bay (Wazniak et al., 2004). They are separated from the Atlantic Ocean by a barrier island (Fenwick Island), and connected to the ocean through the Ocean City Inlet at the southern end of Isle of Wight Bay. The drainage area for the Bays is merely about 4 times as large as their open-water area, and the St. Martin River contributes 62% of the total drainage area for the Bays (Wells et al., 1994). Due to the relatively small drainage area and flat topography, the Bays receive a small inflow of fresh water, and the limited freshwater input combined with restricted access to the open ocean contributes to poor flushing of the Bays (Wells et al., 1994). The St. Martin River is a small, coastal plain river draining sandy sediments, and so fluvial sediment input is minor. Instead, shoreline erosion is a significant source of sediment, contributing up to an estimated $11.6 \times 10^6$ kg/y of total sediments into the Bays (Wells et al., 1994; 2002). The rate of relative sea-level rise (RSLR) in the area is among the highest on

the U.S. Atlantic coast at 4.94 mm/y over the past 40 years (https://tidesandcurrents.noaa.gov/sltrends/sltrends_station.shtml?id=8570283).

Marshes have historically lined the shorelines around the Bays but have been shrinking from sea-level rise and increased development that has converted much of the remaining marsh to bulkhead, riprap, or rock sill living shorelines (Dolan et al., 1980). The living shoreline at Sunset Island was installed in 2007, combining marsh restoration with a sill at the edge made of granite rocks. The sill, designed as a shore-parallel, low-rising breakwater, aimed to protect vegetation closer to the land and promote oyster recruitment (Smith et al., 2018). As measured in ArcGIS 10.8.1, the living shoreline marsh spanned approximately 200 m in length, with an average width of 10 m (Figure 2.1c). The sills, about 1 meter in width, were positioned at the marsh edge, slightly below the mean water level. In close proximity to the living shoreline, there is a natural marsh shoreline (70 m long and 10 m wide) that serves as a reference for this study (Figure 2.1c). Both the living shoreline and natural marsh were dominated by *Spartina alterniflora*.

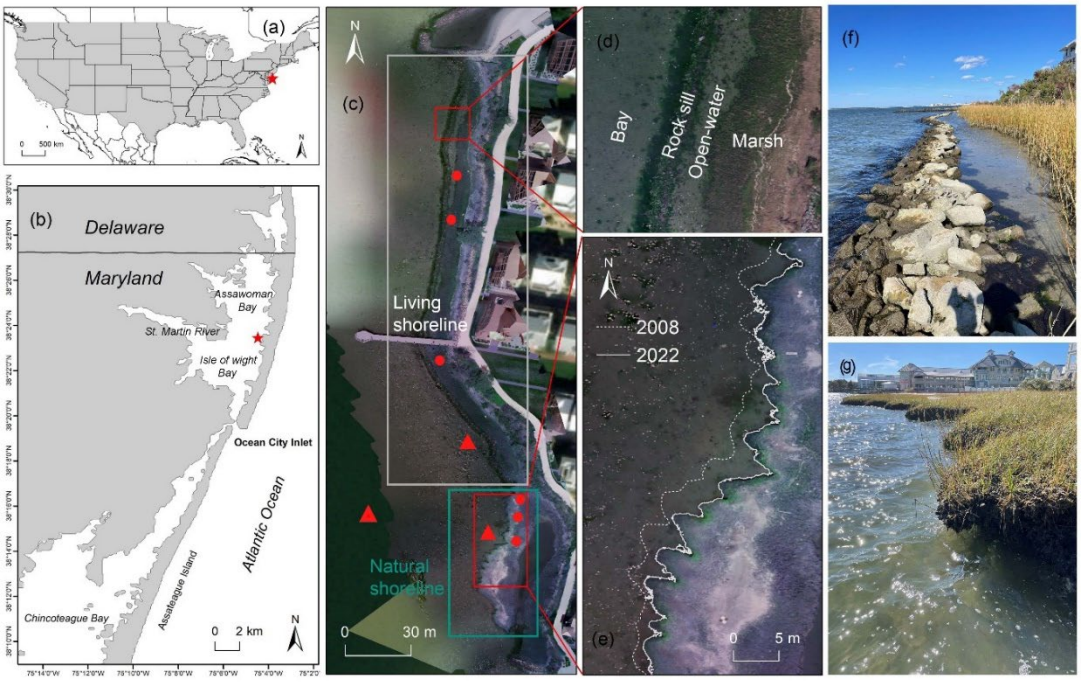


Figure 2.1. Location of study site (a and b); red circles indicate the transect locations, and red triangles show where the equipment (a buoy, an Acoustic Doppler Current Profiler and a turbidity sensor offshore and two turbidity sensors in front of the natural marsh and living shoreline, respectively) was deployed (c); remote sensing images and photos show marsh boundary degradation in the living shoreline (d and f) and natural marsh (e and g). Note: The shorelines in (e) were extracted through visual inspection using ArcGIS 10.8.1, with the 2008 shoreline derived from Google Earth imagery and the 2022 shoreline obtained from drone imagery.

### 2.2.2. Field and Lab Methods

Field sampling was conducted from 2021 to 2022, involving RTK-GPS elevation surveys, vegetation sampling, and sediment core collection along six transects (3 in the living shoreline and 3 in the natural marsh; Figure 2.1c) in the intertidal zones. Sampling took place twice a year, during the growing season (April or July) and in

October near the end of the growing season. RTK-GPS surveys were conducted along each transect, recording elevation at each site for vegetation and sediment characterization, as well as additional points between sites and along the shorelines. Elevation was measured with a geodetic GNSS (GPS + GLONASS) receiver, specifically the Topcon Hiper V, in network Real-Time Kinematic (RTK) mode (Taddia et al., 2021). The instrument's base was placed on known coordinates (Assawoman Bay benchmark REEDY 2 AZ MK 3: https:// www.ngs.noaa.gov/NGSDataExplorer/) located ~0.5 km to the south of the study site. Network Accuracy estimates per FGDC Geospatial Positioning Accuracy Standards is shown in Table S2.1 in the supplementary material. The coordinates were recorded in NAD83(NSRS2007) / UTM zone 18N reference system, while heights were converted into orthometric elevations referred to the NAVD 88 vertical datum. In the marsh, stem density was estimated at each sampling site using a 0.01 $m^2$ quadrat. Stem height and diameter were estimated by measuring five random stems at each site. The stem diameter was measured at 15 cm from the soil surface using a Vernier caliper (Fleri et al., 2019; Nardin et al., 2021). Push cores (5-10 cm long) were collected in the mid-intertidal zone at each transect. All cores were returned intact to the lab where sediments were sectioned into 1-cm increments. In the lab, the top 2 cm of sediments were analyzed for grain size and organic matter content. Grain size analyses were performed by adding sodium metaphosphate to samples and placing them in a sonicator for disaggregation, and then wet sieving samples to separate the mud fraction (<64 μm) from the sand-sized fraction (>64 μm). Subsequently, the sand fraction was dry sieved from 64 μm to 500 μm, using a standard set of 13 sieves, to

calculate the median diameter (D50) of the sand fraction (Palinkas et al., 2013). Organic matter content was measured via combustion at 450°C for 4 hours with the top 2 cm surface sediment of the push cores (Palinkas et al., 2013). Sediment deposition rate was determined from the naturally occurring radioisotope $^{7}$Be (half-life 53.3 days) to capture seasonal-scale processes following Palinkas et al. (2013; 2023).

We deployed several instruments to capture offshore hydrodynamics during a high-energy event from 23 February to 1 March 2023, using an Acoustic Doppler Current Profiler (ADCP), a buoy, and a turbidity sensor to measure the time series of water level, waves, and turbidity, respectively. Another two turbidity sensors were deployed adjacent to the living shoreline and natural marsh, respectively (Figure 2.1c). This time frame was selected specifically to obtain model parameters for a high-energy event rather than including more quiescent periods. This approach has been used by Zhu and Wiberg (2022) and Vona and Nardin (2023). The ADCP was a Nortek Aquadopp Profiler, which included a pressure sensor integrated into the sensor head. The pressure data were then converted to water level using OCEANLYZ, a MATLAB toolbox developed by Karimpour and Chen (2017). The significant wave height was measured by a spotter buoy from SOFAR. Turbidity data were obtained using a YSI 600OMS V2 Optical Monitoring Sonde equipped with a 6136 turbidity sensor. Following Coleman et al. (2020), turbidity data were converted to Suspended Sediment Concentration (SSC) through laboratory calibrations using samples collected from lab and in-situ field sampling. In the laboratory, we created 10

sediment-water slurries with varying SSC levels and measured them using an additional turbidity sensor. In the field, we collected water samples twice around the Monitoring Sonde at different tidal stages and recorded the corresponding time. We compared the turbidity measurements from the sensor to the total suspended solid measurements obtained through vacuum filtration of water samples and sediment-water slurries. More details about the data calibration can be found in supporting information Figure S2.1.

### 2.2.3. Acquisition and Processing of Drone Images

On April 26, 2022, we utilized a DJI Phantom 3 Professional (DJI-P3P) drone to capture aerial images of the marsh. During this time, the marsh featured open terrain with sparse vegetation. Following Nardin et al. (2021), high spatial resolution multispectral images were then retrieved by a Structure from Motion (SfM) approach, which enables a 3D geometry (structure) reconstruction and characterization from a set of 2D images of the scene (motion). The DJI-P3P drone was equipped with a MicaSense RedEdge-M multispectral camera. Aircraft and camera specifications are reported in Table S2.2 in supplementary material. The MicaSense camera can collect the RGB bands as well as the near-infrared wavelengths (NIR) band, specifically with a central value of 840 nm and a Full-Width Half-Maximum (FWHM) of 40 nm. The flight was conducted at an altitude of 43 m, covering an area of 0.0318 $km^2$, resulting in a ground resolution of 1.46 cm/pixel.

The photogrammetric model reconstruction was performed using Agisoft PhotoScan/Metashape Professional software (Nardin et al., 2021). A set of 7 Ground

Control Points (GCPs) and Check Points (CPs) were deployed during the flight. The GCP/CP targets are about 60 cm × 60 cm, clearly visible on the acquired images. Figure S2.2 in supplementary material illustrates the location of the targets. Coordinates at the center of GCPs were collected using a Topcon HiPer V geodetic receiver in network RTK mode. Local elevation at each GCP was also surveyed with the RTK-GPS for an accurate assessment of the Digital Terrain Models (DTMs). The residuals computed for both GCPs and CPs are shown in Table S2.3 in the supporting information. The average vertical error for the CPs was -0.098 m with a RMSE of 0.032 m. This represents the DTMs were generally close to the true bare earth elevation under the sparse vegetation (Medeiros et al., 2015).

### 2.2.4. Model Settings

To investigate processes at the marsh edges under high-energy conditions, we used the spatially resolved and process-based Delft3D FLOW/MOR model (Lesser et al., 2004) coupled with the nearshore phase-averaged wave model SWAN (Booij et al., 1999) to simulate hydrodynamics and sediment transport. To improve computational efficiency, three domains were defined: a large model domain covering the Bays, a local model domain spanning the narrow marshes along the shorelines, and a refined model domain based on a representative cross-section in the living shoreline. The large model domain consisted of 44 × 27 rectangular grid cells with a spatial resolution of 100 m; the medium model domain consisted of 73 × 84 rectangular grid cells with a spatial resolution of 10 m; the refined model domain consisted of 46 × 97 rectangular grid cells with a spatial resolution of 1 m. The smaller model domain was

nested in the bigger model domain using the domain decomposition technique (Deltares, 2014). The representative cross-section for the small domain was measured at 200 m × 50 m. Figure 2.2 illustrates the elevation changes observed in three typical cross-sections: Tra A, where no obvious open water was observed in the living shoreline, Tra B, where open water was present in the living shoreline, and Tra C, natural marsh with no hardened structure. The average sill height for the open-water section was measured at -0.10 ± 0.04 m, while the average sill height for the no open-water section was slightly higher at -0.06 ± 0.03 m ($p < 0.01$). The depth setting for the small domain was primarily based on the characteristics observed in Tra B (Figure 2.2b).

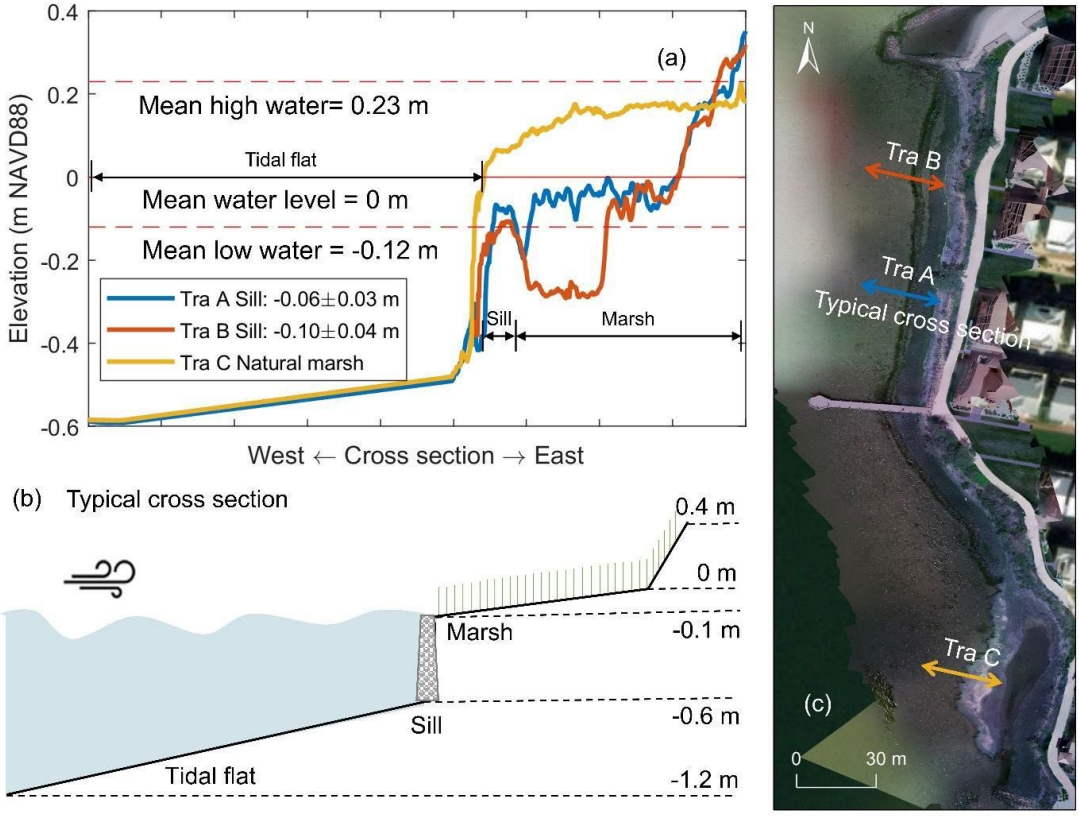

Figure 2.2. Model setup. (a) Line plot demonstrating variation of elevation across typical cross transect A (no obvious open-water conversion), B (obvious open-water conversion), and C (natural marsh); (b) typical cross-section for model setting; (c) drone image showing the location of the typical cross sections.

The model incorporated modules for flow, wave, and sediment transport, and considered the presence of vegetation and rock sills. The input forcing condition of this model, including wind and water level conditions from February 21, 2023, to March 1, 2023, is from the NOAA station at Ocean City Inlet (~7 km south of the study site; Figure 2.5a and b; https://tidesandcurrents.noaa.gov/stationhome.html?id=8570283). Following Zhu and Wiberg (2022), we ran the model for a monthly simulation from Feb. 22 to Mar. 25, 2023, and compared the results to $^{7}$Be-derived sedimentation rates to validate morphology change. Following Zhu et al. (2022), we used a wind speed threshold of 8 m/s (top 5% in 2023, Figure S2.3 in supplementary material) to identify major high-energy events. To generate the best tidal simulation results for the shallow Bays, the water level was dampened by a factor of 0.6 and delayed 2 hours (Castagno et al., 2018; Zhu et al., 2021). The eastern open ocean boundary of the finest model domain was forced with hourly water levels, while the northern and southern boundaries were set as Neumann type (Vona et al., 2021). Sediment concentrations at all three model boundaries of the refined model domain were set to 0.0025 kg/m$^3$ for all sediment classes (see below), based on validation runs. Wave simulations were coupled with the flow model every hour using spatially uniform wind conditions from the same

NOAA station and a JONSWAP bottom friction coefficient of 0.067 $m^2/s^3$ (Nardin et al., 2020). To incorporate the effects of marsh vegetation on flow and wave attenuation, the Baptist vegetation model (Baptist et al., 2005; 2007) and the Suzuki vegetation wave energy dissipation model (Suzuki et al., 2012) were implemented in Delft3D-SWAN. Previous research found significant differences in stem flexibility between species (Möller et al., 2014; Rupprecht et al., 2015), which further determines drag forces in attenuating wave energy (Paul et al., 2016). For rigid vegetation, such as *S. alterniflora*, Delft3D uses the equations proposed by Baptist (2005), while in the case of flexible *Z. marina*, Delft3D assumes a greater degree of roughness (Lera et al., 2019). Our study site is dominated by *S. alterniflora* and the vegetation in winter is generally rigid with low stem densities and heights. Therefore, the model considers vegetation as rigid cylindrical structures and resolves vegetation effects in the momentum balance equation (Baptist et al., 2005). Spatially uniform marsh characteristics that were measured in the field (vegetation height = 0.26 m, stem diameter = 0.08 cm, and density = 96 shoots/$m^2$) were used in the model. Vegetation was placed in the model immediately adjacent to and landward of the rock sill. Following Vona et al. (2021), the rock sill was incorporated into the model as a non-erodible structure by setting the spatially varied erodible sediment depth as 0.

Following Kang and Xia (2020), model bathymetry was extracted from the 1 arc-minute global relief model ETOPO1 Global Relief Model from National Oceanic and Atmospheric Administration (NOAA). According to previous field sampling, sediment cores from the living shoreline marsh were relatively sandy with an average

grain size of 175 μm, and around 90% of them were sand. Therefore, three types of sediments were specified, including a cohesive medium to fine silt fraction (5%) with a representative floc settling velocity of 0.75 mm/s, a cohesive coarse silt fraction (5%) with a settling velocity of 3.6 mm/s, and a non-cohesive sand fraction (90%) with a representative median grain size of 175 μm. Sediment grain density was set to 2650 $kg/m^3$ and dry bed density was specified as 500 $kg/m^3$. The threshold depth for drying and flooding and the minimum depth for computing sediment transport were both set to 0.1 m (Wiberg et al., 2015; Zhu and Wiberg, 2022). The initial sediment layer thickness was set to 0.05 m, and the erosion rate was proportional to the availability of types of sediment fractions (Deltares, 2014). The critical shear stress for cohesive sediment erosion was set to 0.04 $N/m^2$ (Zhu and Wiberg, 2022), and an erosion parameter of $7\times10^{-5}$ $kg/m^2/s$ was selected for cohesive sediment erosion after model calibration to generate the best agreement between modeled and measured SSC at Sunset Island. For a complete list of parameters used in the model, refer to Table 2.1.

Table 2.1. Parameters used in the model.

| Module | Parameter | Value | References |
|---|---|---|---|
| Sediment transport | Chézy bed roughness | 65 $m^{1/2}$ /s | Wiberg et al. (2015) and Nardin et al. (2018) |
| | Sediment size for non-cohesive sand (mass fraction 90%) | 175 μm | Wiberg et al. (2015) and Zhu and Wiberg (2022) |
| | Settling velocity for coarse cohesive sediment (mass fraction 5%) | 3.6 mm/s | Wiberg et al. (2015) and Zhu and Wiberg (2022) |
| | Settling velocity for fine cohesive sediment (mass fraction 5%) | 0.75 mm/s | Wiberg et al. (2015) and Zhu and Wiberg (2022) |
| | Sediment grain density | 2650 $kg/m^3$ | Wiberg et al. (2015) and Nardin et al. (2018) |
| | Dry bed density | 800 $kg/m^3$ | Wiberg et al. (2015) and Nardin et al. (2018) |
| | Boundary conditions for sediment input | 0.0025 $kg/m^3$ for each sediment type | Selected for this study after model calibration |

| | | | |
|---|---|---|---|
| | Threshold depth for drying and flooding | 0.1 m | Zhu and Wiberg (2022) |
| | Minimum depth for computing sediment transport | 0.1 m | Wiberg et al. (2015) |
| | Critical shear stress for cohesive sediment erosion | 0.04 $N/m^2$ | Zhu and Wiberg (2022) |
| | Erosion parameter for cohesive sediment erosion | $7\times10^{-5}$ $kg/m^2/s$ | Selected for this study after model calibration |
| | Active sediment layer thickness | 0.05 m | Wiberg et al. (2015) and Zhu et al. (2021) |
| Wave | JONSWAP bottom friction coefficient | 0.067 $m^2/s^3$ | Nardin et al. (2020) |
| Vegetation | Height | 0.26 m | Selected for this study based on field sampling |
| | Density | 96 $\#/m^2$ | Selected for this study based on field sampling |
| | Baptist 2 equation | #154 | Nardin et al. (2018) |
| | Drag coefficient | 1.65 | Nardin et al. (2018) |
| | Alluvial bed roughness | 65 $m^{1/2}/s$ | Nardin et al. (2018) |

### 2.2.5. Model Skill Indices and Validation

The output from the validation run was compared with observations of water level, significant wave height, and suspended sediment concentration (SSC) offshore from February 23 to March 1, 2023. To assess the performance of the model in simulating hydrodynamics and sediment transport in the living shoreline, we calculated model skill indices, including coefficient of determination ($R^2$), Bias, root mean square error (RMSE), and Willmott Skill Index. The Willmott Skill Index (Willmott, 1981) is defined as,

$$\text{Skill} = 1 - \frac{\sum \left| X_{\text{model}} - X_{\text{obs}} \right|^2}{\sum \left( \left| X_{\text{model}} - \overline{X_{\text{obs}}} \right| + \left| X_{\text{obs}} - \overline{X_{\text{obs}}} \right| \right)^2}$$

where $X_{\text{model}}$ is the model result, and $X_{\text{obs}}$ is the field observation. The skill is usually between 0 to 1, and a higher value of skill stands for better model performance. In coastal hydrodynamic simulations, model skill scores higher than 0.8 are considered generally good model predictions, and skill for water level is usually higher than wave height and SSC (Warner et al., 2005; Liu et al., 2009; Zhu et al., 2021).

### 2.2.6. Statistical Analyses

An independent-sample T-test was used to examine the significance of sample differences. Pearson correlation analyses were used to quantify the relationship between elevation and the proportion of open water. The statistical analyses were performed in R.

## *2.3. Results*

### 2.3.1. Spatial Variation of Local Elevation

We analyzed aerial images (Figure 2.1c, d, and e) to assess potential processes at the edge of the natural marsh and the living shoreline, noting distinct variations in patterns between the two. The natural marsh had a jagged shoreline, likely from erosion through undercutting and slumping, causing the marsh edge to collapse into the water (Figure 2.1g). Furthermore, Figure 2.1e illustrates the shoreline change of the natural marsh from 2008 to 2022, revealing significant lateral erosion of approximately 0.3 m/y. In contrast, the living shoreline had a more linear shape, both at the rock sill and between the sill and the vegetation, suggesting marsh retreat and open-water conversion behind the rock sills, as shown in Figure 1d. Notably, we observed an expansion of ponds behind the rock sills (Figure 2.1f). Assuming that vegetation was planted immediately in front of the rock sill, maximum retreat of the vegetated edge occurred at 0.2 m/y from 2008 to 2022.

To investigate the potential factors influencing the open-water conversion process, we analyzed the DTMs data and found a nonlinear correlation ($y = 0.30e^{-23.73x}$, $R^2 = 0.934$) between the proportion of open water and elevation (Figure 2.3). As elevation decreased, the proportion of open water increased. Notably, the average values for the natural marsh and living shoreline align closely with this curve. Furthermore, we found that the elevation in the natural marsh (average 0.15±0.08 m) was significantly higher than that in the living shoreline (average -0.05±0.13 m; $p < 0.01$).

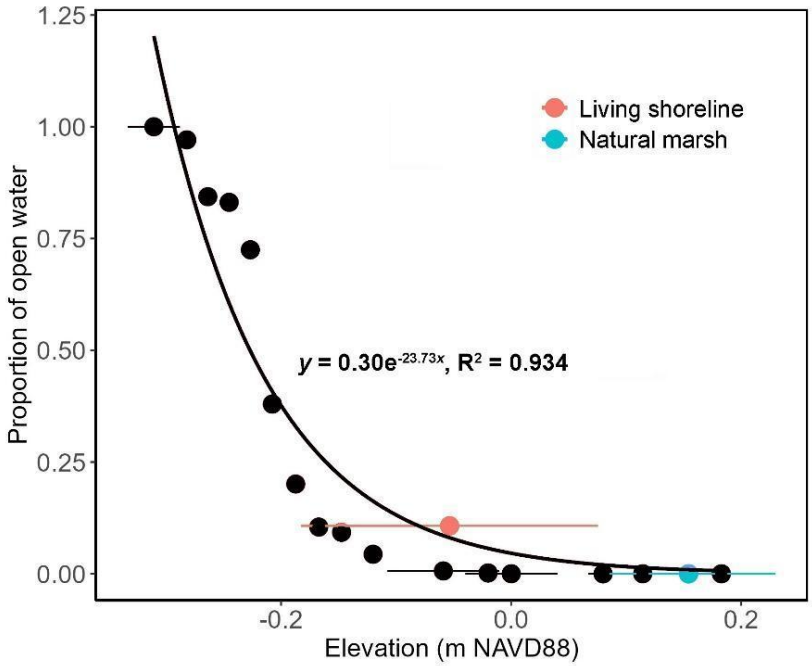


Figure 2.3. Correlation between the proportion of open water and elevation. Black points denote data derived from drone images of the living shoreline with open water. Red and blue points represent average values across the living shoreline and natural marsh, respectively.

### 2.3.2. Sediment and Vegetation Characteristics

Suspended Sediment Concentration (SSC) in the vicinity of the natural marsh was $0.021 \pm 0.039$ kg/m$^3$, significantly higher than that adjacent to the living shoreline marsh ($0.012 \pm 0.011$ kg/m$^3$; $p < 0.01$). In contrast, SSC offshore was notably lower at $0.009 \pm 0.007$ kg/m$^3$, in comparison to the coastal zone adjacent to the shorelines (Figure 2.4; $p < 0.01$). While average values may be similar ($p < 0.01$), SSC adjacent to the natural marsh is consistently higher than at the living shoreline, and the maximum value is >4x higher adjacent to the natural marsh. Additionally, we

observed that variations in SSC in front of the natural marsh were more substantial than those in front of the living shoreline marsh (Figure 2.4).

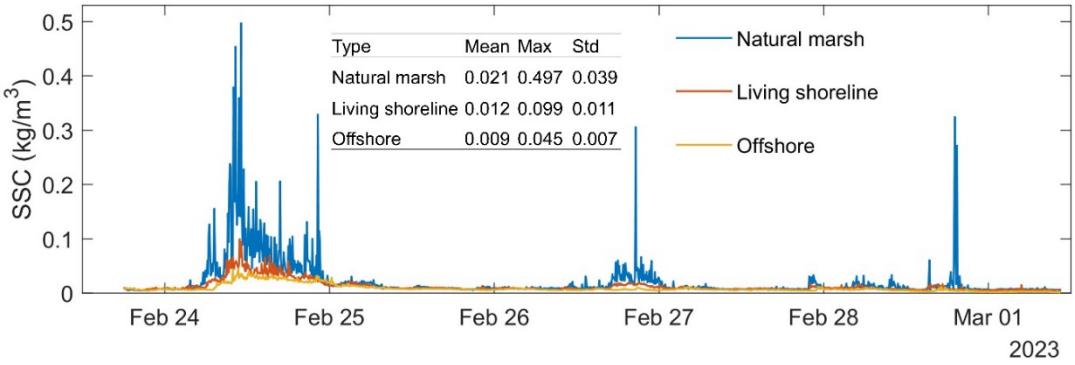


Figure 2.4. Variations of suspended sediment concentration (SSC, kg/m$^3$) adjacent to the natural marsh (blue), living shoreline (red), and offshore (orange).

We found significant differences in sediment and vegetation characteristics between the living shoreline and the natural marsh at Sunset Island. Sediments in the living shoreline marsh were sandy with greater grain size and lower organic content than in the natural marsh ($p < 0.01$ for both; Figure 2.5a and b). The natural marsh also demonstrated a higher seasonal sediment deposition rate than the living shoreline marsh ($p < 0.05$; Figure 2.5c). Though vegetation in the living shoreline had greater stem heights and diam ($p < 0.01$; Figure 2.5d and e), the natural marsh had higher stem densities ($p < 0.01$; Figure 2.5f).

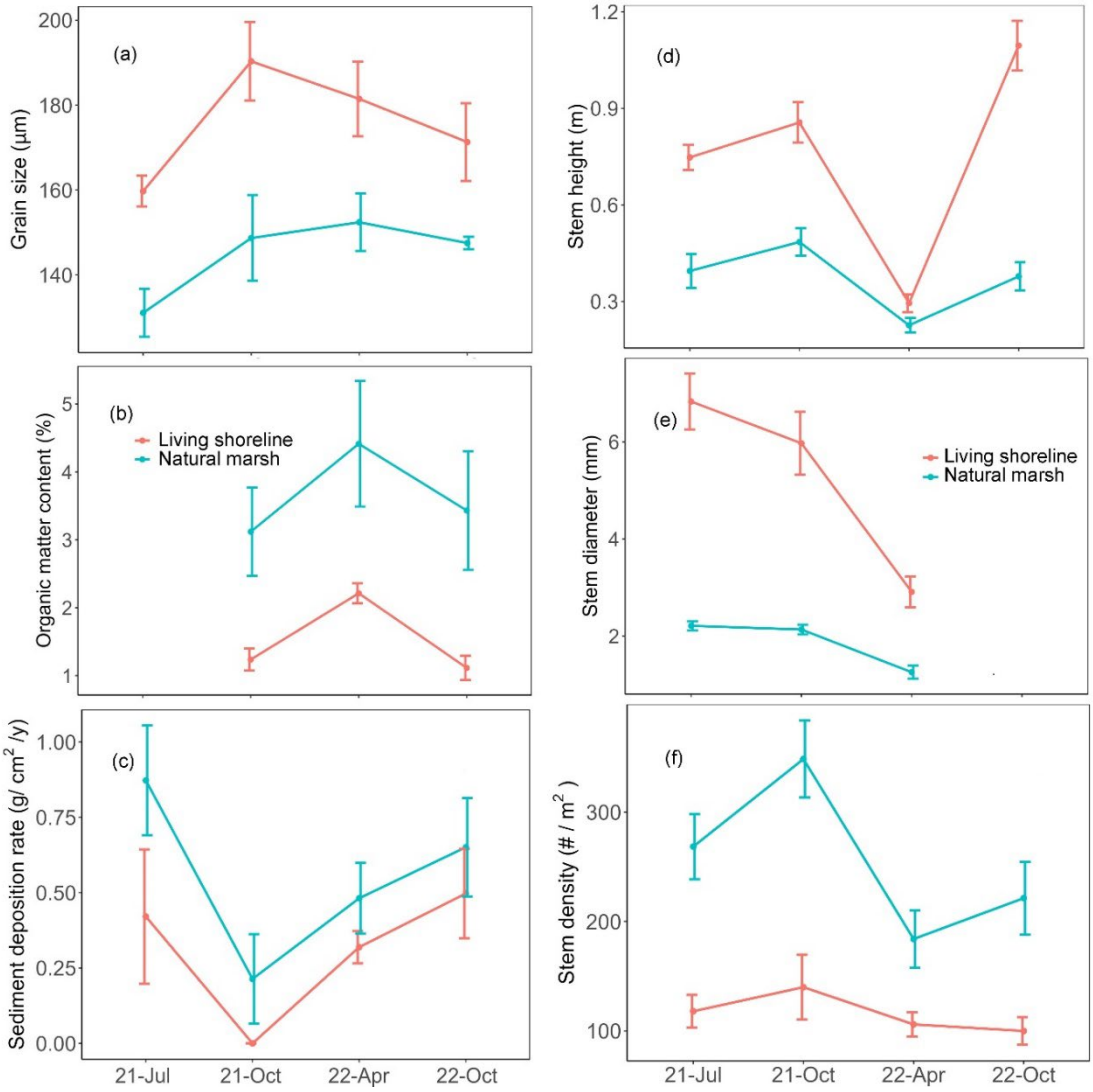


Figure 2.5. Comparison of sediment characteristics (grain size, organic matter content, and $^{7}$Be-derived sediment deposition rate; a, b, and c) and vegetation characteristics (stem height, diameter and density; d, e, and f) between the living shoreline (red) and natural marsh (blue) from 2021 to 2022.

### 2.3.3. Model Validation

Under the 8-day forcing and high-energy conditions from 21 February to 1 March 2023 (Figure 2.6a and b), the modeled water level (Figure 2.6c), significant wave height (Figure 2.6d), and suspended sediment concentration (SSC; Figure 2.6e) were correlated with field measurements (Table 2.2 and Figure S2.4 in supplementary material). However, during the last 3 days of the model validation run, there were discrepancies in the water level between the modeled results and measurements, which might be attributed to the long distance (~7 km) between the Ocean City inlet NOAA station and Sunset Island. Despite this, the modeled water level generally matched the measurements well ($R^2$ = 0.528 and Skill = 0.891). The model effectively replicated wave patterns at the shoreline, with an $R^2$ of 0.684 and a skill score of 0.976. The model captured the majority of sediment resuspension events, resulting in an $R^2$ of 0.541 and a skill score of 0.899, but the model underpredicted the SSC peak on February 24, 2023. This discrepancy might be caused by the shallow water depths at low tides (<0.15 m). In this model, the minimum water depth for computing sediment transport was set to 0.1 m, which might constrain reproducing the SSC peak with a limited water level. In addition to hydrodynamic validation, the modeled sediment deposition rate over the longer run (1 month) extrapolated to an annual rate (onshore 4.9 mm/y and offshore 1.4 mm/y) at the living shoreline marsh was similar to the average marsh accretion rate at the same site (onshore 4.3 ± 1.1 mm/y and offshore 1.9 ± 0.8 mm/y) determined by $^{7}$Be dating. Overall, the model is able to reproduce field measurements of the hydrodynamics that drive morphological change relatively well.

Table 2.2. A summary of statistical metrics for model validation

| Parameter | Sample size (N) | $R^2$ | Bias | RMSE | Skill |
|---|---|---|---|---|---|
| Water level | 138 | 0.528* | 0.069 | 0.111 | 0.891 |
| Significant wave height (Hs) | 137 | 0.684* | -0.013 | 0.030 | 0.976 |
| Suspended sediment concentration (SSC) | 137 | 0.541* | -0.075 | 0.036 | 0.899 |

Notes: (*$p < 0.01$)

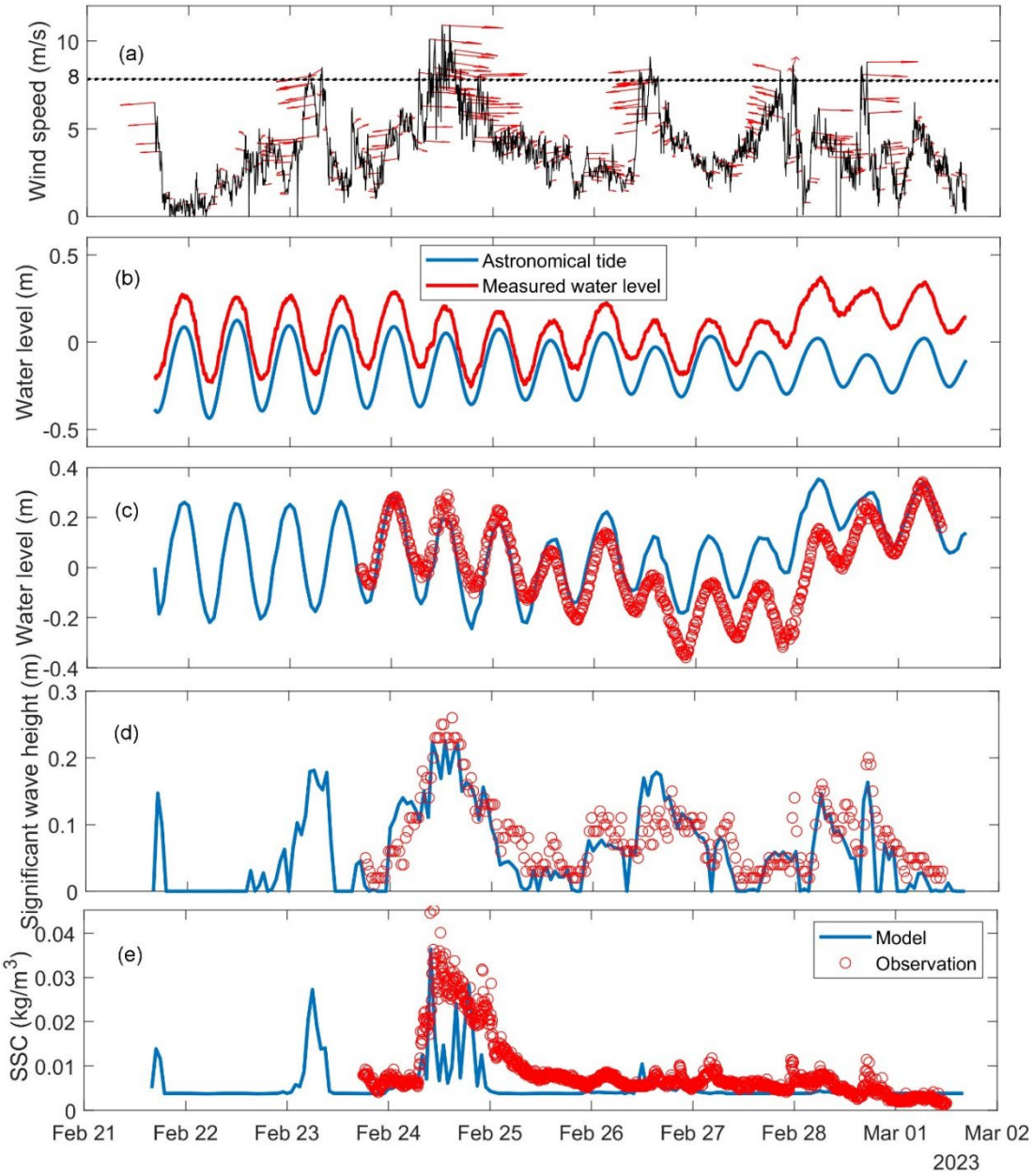


Figure 2.6. Comparison of measured and modeled hydrodynamic conditions, output from 23 February to 1 March 2023: (a) wind speed and direction, (b) measured water levels and astronomical tides at the Ocean City Inlet from NOAA station; (c) water level, (d) significant wave height (Hs), and (e) total suspended sediment concentration (SSC).

### 2.3.4. Spatial Distribution of Modeled Hydrodynamic Conditions in the Living Shoreline

Figure 2.7 provides further insights into the modeled hydrodynamic conditions and morphology changes along a cross-section relative to the distance from the marsh edge in the living shoreline. As the distance to the marsh edge increased (moving landward), the water level decreased (Figure 2.7a). Within 6 m of the marsh edge, the velocity was higher compared to the other parts of the marsh (Figure 2.7b). The pattern of bed shear stress followed a similar trend as velocity (Figure 2.7c), with higher values within 6 m of the marsh edge compared to the rest of the marsh. In terms of vertical change, Figure 2.7d revealed that erosion predominantly occurs within 5 m of the marsh edge. Beyond this distance, there was a relatively greater amount of deposition than erosion in the marsh.

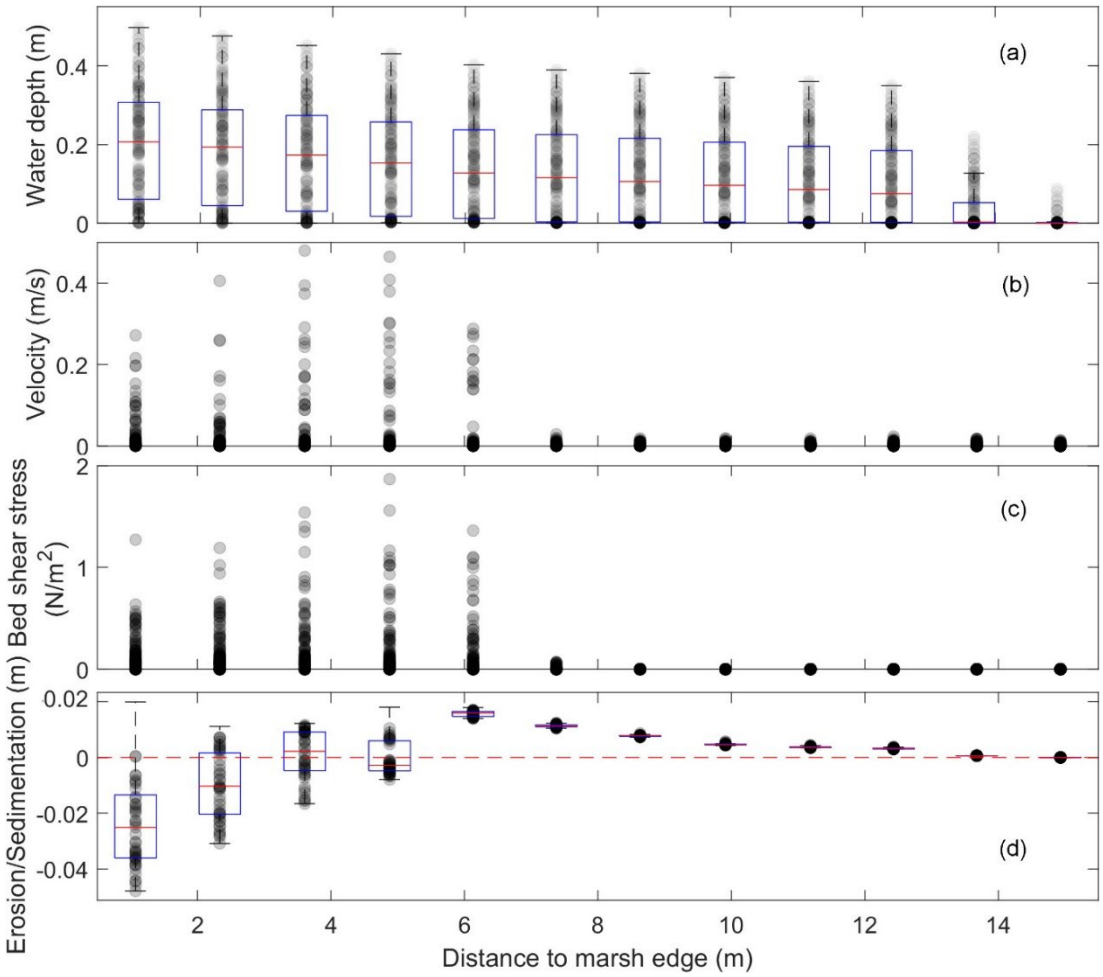


Figure 2.7. Spatial distribution of modeled hydrodynamic conditions and morphology change in the marsh along cross-section with distance to living shoreline marsh edge: (a) water level (m), (b) velocity (m/s), (c) bed shear stress ($N/m^2$), (d) cumulative erosion/sedimentation (m; negative is erosion and positive is deposition). Each circle is a data point and is transparent gray; darker colors indicate overlapping circles.

### 2.3.5. Influence of Wave Exposure on Sediment Transport in the Living Shoreline

To assess the impact of wind-driven waves on the living shoreline marsh, we analyzed major high-energy events by setting a wind speed threshold of 8 m/s,

representing the top 5% of wind speeds recorded in 2023 (Zhu et al., 2022). During the simulation, 5 high-energy events where wind speed exceeded 8 m/s were identified (Figure 2.6a and Figure 2.8a). Each of these events was associated with a noticeable increase in significant wave height when the wind speed surpassed 8 m/s (Figure 2.6d). Additionally, the SSC saw a marked increase from February 24 to February 25, aligning with significantly higher wind speeds exceeding the established threshold, with the wind blowing west and hitting the shorelines perpendicularly (Figure 2.6e). Our analysis revealed that substantial sediment transport occurred between the subtidal zone and the marsh platform during these events. The total sediment flux into the marshes exhibited a substantial increase and the erosion area decreased during west wind events when the wind blew towards the living shoreline (Figure 2.8). Conversely, the sediment flux experienced a sharp decrease and the erosion area increased during east wind events when the wind blew away from the living shoreline (Figure 2.8).

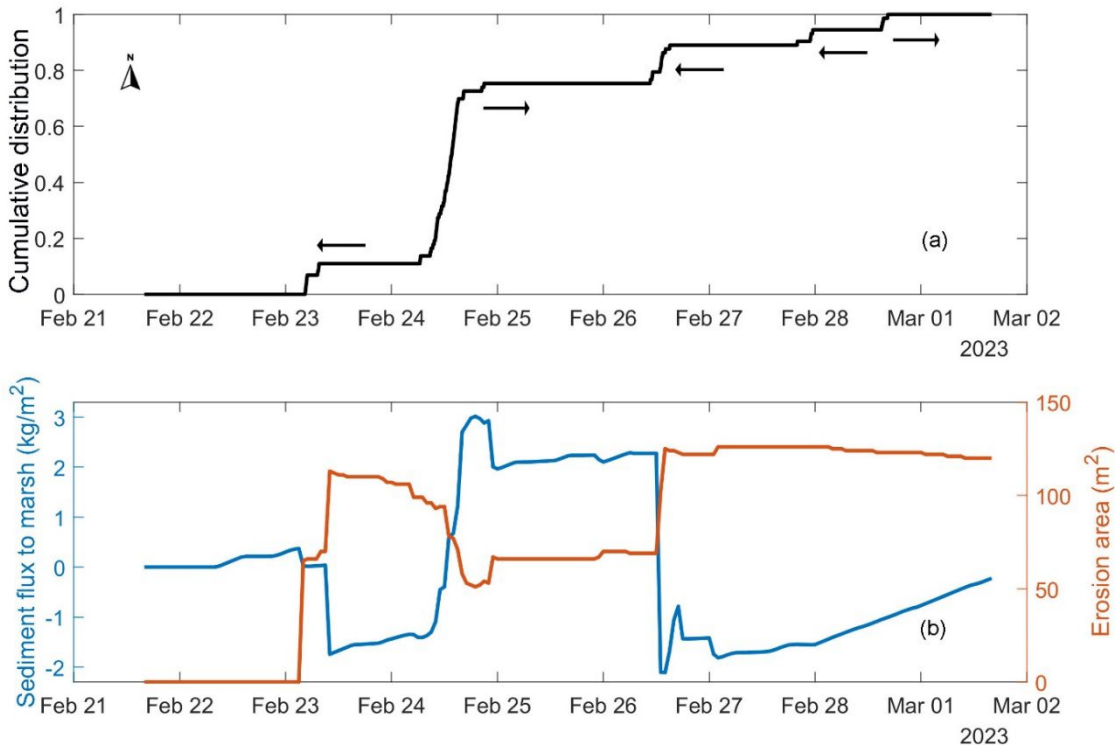


Figure 2.8. (a) Cumulative distribution of high-energy events during the simulation (proportion of time when the wind speed is higher than 8 m/s; arrows indicate the dominant wind direction at each high-energy event with north pointing upward); (b) Modeled results of cumulative sediment flux to marsh (kg/m$^2$; left y-axis) and erosion area (m$^2$; right y-axis) of the living shoreline marsh.

### 2.3.6. Influence of Sill and Bank Height on Sediment Transport in the Living Shoreline

We conducted additional model runs under identical forcing conditions but varying the sill and bank (both the sill and marsh) heights. The results demonstrated that increasing the sill and bank height led to less erosion at the marsh edge of the living shoreline (Figure 2.9). Notably, when the sill elevation reached -0.06 m relative to the

mean water level, there was a continuous positive sediment flux to the marsh throughout the simulation (Figure 2.9a), indicating a net import of sediments to the marsh and vertical elevation gain. The cumulative erosion/sedimentation at the marsh edge increased significantly with higher sill heights and stayed positive when sill height was over -0.06 m to mean water level (Figure 2.9b). Similarly, when the bank elevation was -0.07 m relative to the mean water level, there was a persistent positive sediment flux to the marsh (Figure 2.9c), and the cumulative erosion/sedimentation increased notably with increasing bank heights, peaking at -0.06 m relative to mean water level (Figure 2.9d).

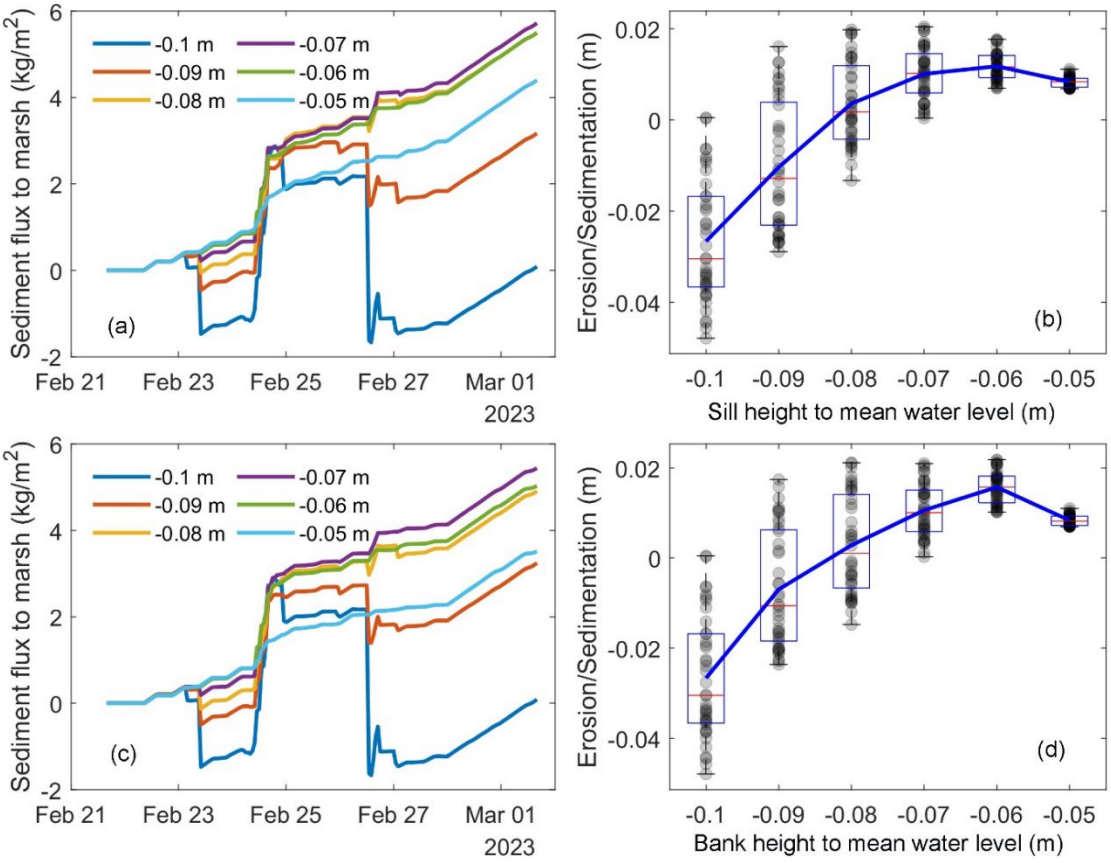

Figure 2.9. Scenario analysis of sediment dynamics in the living shoreline: total sediment flux to marsh (a) and cumulative erosion/deposition (b) with vary height of the rock sill to mean water level (-0.1 to -0.05 m); total sediment flux to marsh (c) and cumulative erosion/deposition (d) with varying height of the bank (both rock sill and marsh platform) to mean water level (-0.1 to -0.05 m).

*2.4. Discussion*

Living shorelines have been shown to attenuate wave energy (Vona et al., 2021), mitigate shoreline erosion (Palinkas et al., 2023), and enhance coastal resilience (Smith et al., 2018; Polk et al., 2022) in the face of accelerated rates of sea-level rise. However, science has lagged behind the rapid expansion of implementation, leaving significant gaps in knowledge of living shoreline performance, especially during high-energy events. In this study, drone images of a mature rock sill living shoreline (17 years old) showed a gap between the edge of the vegetation and the rock sill (Figure 2.1d and f), which differed from the observed undercutting and slumping in the adjacent natural marsh (Figure 2.1e and g). The rock sills at the seaward side of the living shoreline likely prevented physical erosion at the marsh edge. However, the opening of a gap between the vegetation and the rock sill, converting marsh to open water, is a concern for the long-term persistence of this living shoreline.

Several factors might be associated with this open-water conversion process in living shorelines. Based on the DTM data from the drones, a nonlinear negative correlation ($y = 0.30e^{-23.73x}$, $R^2 = 0.93$) was found between the proportion of open water and elevation. As elevation decreased, the proportion of open water increased in the living

shoreline marsh, similar to findings in natural marshes along the northeast U.S. Atlantic coast (Ganju et al., 2020). We also found that the elevation in the natural marsh (average 0.15±0.08 m) was significantly higher than that in the living shoreline (average -0.05±0.13 m; $p < 0.01$), which highlights the pivotal role of elevation in driving the conversion of open water in marsh ecosystems. While we do not know the initial conditions of our study site, a similar elevation difference between living shoreline and adjacent natural marsh has been found in other systems (Smith et al., 2018). The mean water level is around 0 m, higher than the living shoreline but lower than the natural marsh, which would alter sediment supply and the impact of waves even in the absence of a rock sill. Variations in sediment and vegetation characteristics between the living shoreline and natural marsh are likely also linked to the contrasting patterns of marsh loss observed between the two shoreline types. Sediment grain size was higher in the living shoreline compared to the natural marsh ($p < 0.01$; Figure 2.4a), while organic matter content in the living shoreline was lower than in the natural marsh ($p < 0.01$; Figure 2.4b). Though the living shoreline exhibited greater stem height and diameter ($p < 0.01$; Figure 2.4d and e), vegetation in the natural marsh was significantly denser than the living shoreline ($p < 0.01$; Figure 2.4f). These findings agree with prior investigations on living shorelines conducted in the Chesapeake Bay (Bilkovic and Mitchell, 2013; Palinkas et al., 2023). The coarser sediment and taller plants in the living shoreline, along with the presence of the rock sill, may confer greater stability and resistance to erosion, as well as limiting sediment supply to the marsh. In contrast, the higher organic matter content and stem density in the natural marsh may enhance its cohesive properties,

rendering it more vulnerable to slump and collapse into the water, with sediment available for transport back onto the platform to nourish the marsh.

Erosion of the natural marsh shoreline, but not the living shoreline, likely explains why SSC, especially maximum SSC during high-energy events, was much higher adjacent to the natural marsh than the living shoreline, and SSC offshore was much lower ($p < 0.01$; Figure 2.4). Moreover, the natural marsh demonstrated a higher seasonal sediment deposition rate than the living shoreline marsh ($p < 0.05$; Figure 2.5c). These results suggest that shoreline erosion serves as a primary sediment source to the nearshore area and natural marsh. The natural marsh is eroded at the shoreline through undercutting and subsequent slumping, leading to an increase in SSC immediately adjacent to the shorelines, especially during high-energy events (Figure 2.10a and b). Eroded sediment can be transported back onto the marsh platform in subsequent events, contributing to elevation gain (Figure 2.10c). This agrees well with previous work at natural marshes that marsh salt marsh frontal erosion alters the export of sediments (Li et al., 2018; 2019), and it provides an important fraction of the material needed for marsh vertical accretion (Hopkinson et al., 2018). In contrast, the living shoreline is protected by a rock sill, which dissipates incoming wave energy but also might increase energy immediately landward of the sill, both of which would limit sediment deposition and elevation gain in the marsh (Figure 2.10d, e and f).

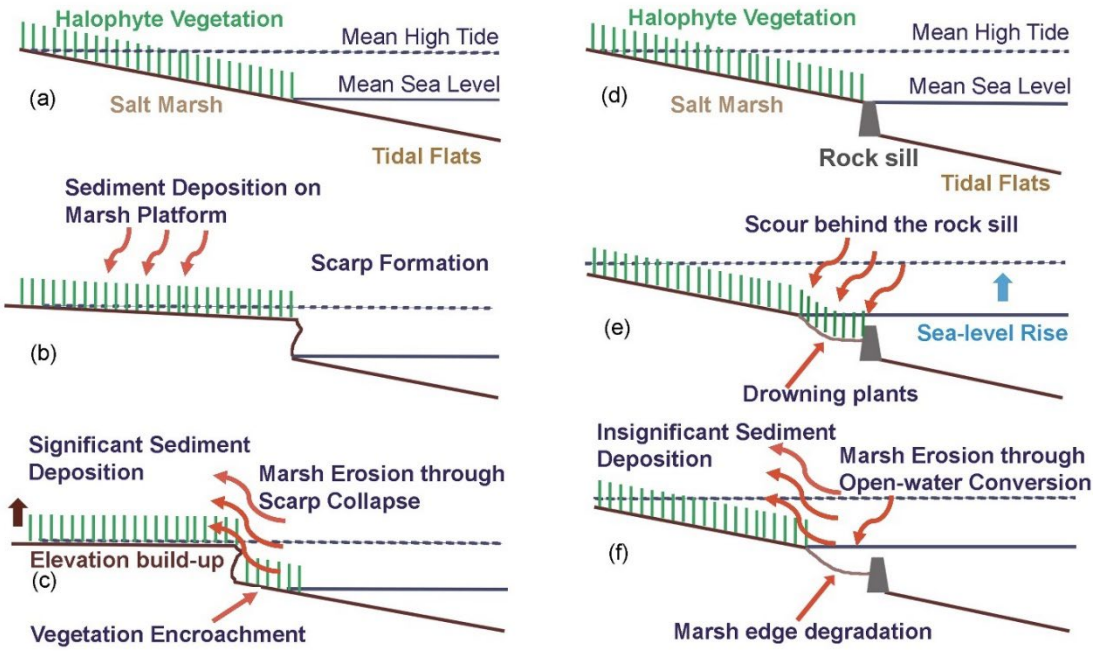


Figure 2.10. Conceptual model of marsh boundary degradation in natural marshes (a, b and c; adapted from Fagherazzi et al., 2020) and living shoreline marshes (d, e, and f).

Substantial sediment transport occurred between the offshore subtidal zone and the marsh platform during the high-energy events. In 2023, the total period of the identified high-energy events was 395 hr, which roughly accounted for 5% of total time in our analysis (Figure S2.3a in supplementary material). Previous research on natural marshes in VCR has reported that storm surge events occur 5% of the time, but contribute 40% of marsh deposition (Zhu et al., 2022). In this study, the total sediment flux to the marshes exhibited a substantial increase during west wind events when the wind blew towards the living shoreline, and a sharp decrease during east wind events when the wind blew away from the living shoreline (Figure 2.8). The histogram (Figure S2.3b in the supplementary material) illustrated that east winds

were the most common during the simulation period, resulting in significant sediment loss and shoreline erosion. This level of severe erosion is atypical for living shorelines. Conversely, in the Maryland Coastal Bays, southwest winds were the predominant direction in 2023 (Figure S2.3d in the supplementary material), suggesting a potential increase in sediment accumulation in the marsh at Sunset Island.

Within 5 m behind the rock sill at the marsh edge, modeled bed shear stress averaged 0.24 $N/m^2$, reaching a maximum value of 3.77 $N/m^2$, which was higher than the rest of the marsh (Figure 2.7c), potentially contributing to scouring and open-water conversion. Specifically, this increased bed shear stress, particularly during ebb tide, led to more sediment export from the marsh and resulting in local elevation decrease, both of which could contribute to plant dieback and the formation of ponds behind the rock sill at the marsh-sill boundary. Similar to the spatial distribution of bed shear stress, velocity was also higher close to the rock sill, within 5 m of the marsh edge (Figure 2.7b). In terms of vertical change, erosion primarily occurred within 5 m to the marsh edge, while accretion is more prominent beyond 5 m (Figure 2.7d). This corresponds to the approximate width of open water measured in the field and provides a possible explanation for marsh retreat behind the rock sill.

Model results showed that increasing the bank height (both sill and marsh) led to less erosion at the marsh edge of the living shoreline. Specifically, when increasing the sill elevation to -0.06 m or the bank height to -0.07 m relative to the mean water level

(0 m), sediment flux to the marsh stayed positive, which indicated a net import of sediments to the marsh and vertical elevation gain during the simulation (Figure 2.9). This could explain why some sections of the living shoreline did not have a gap between the rock sill and the vegetation. Based on the DTMs data, the average elevation of the rocks at the section with open-water conversion was -0.10±0.04 m, while the average elevation for the rocks at the section without open-water conversion was higher at -0.06±0.03 m ($p < 0.01$). It is important to note that the DTM was collected in April 2022, and the hydrodynamic measurements were taken in February/March 2023, and some differences may have occurred between the two time periods. However, sedimentation rates are 4.3 mm/y, and so the change in marsh elevation from 2022-2023 would be below the resolution of both RTK and drone measurements (~1 mm). According to the design guidelines, height of the rock sill is generally at or a little above Mean Tide Level (MTL; Hardaway, 2017) and below Mean High Water (MHW). Sea level in this region has been rising at around 84 mm since the living shoreline was constructed in 2007, with a regional relative sea level trend of 4.94 mm/y. This implies the continuous rising sea level might partially contribute to the open-water conversion at the marsh boundary behind the rock sills in living shorelines.

Despite the effectiveness of our methodology in capturing the performance of living shorelines during high-energy extreme events, several limitations should be acknowledged. Firstly, the process of open-water conversion can be gradual and may take years to manifest, posing challenges for validation of morphological changes in

an 8-day simulation. Since changes at the open-water conversion in 8 days may not be significant enough to be detected by GPS survey, this study validated morphology by the average sedimentation rate on the marsh platform rather than the rate of open-water conversion. Therefore, the 8-day simulation period during the winter season may not fully capture the long-term effects of such events on shoreline dynamics and morphology. In the Maryland Coastal Bays, prevailing winds from October through June largely originate from the northwest (blowing towards the rock sill in our study site), while the summer months see prevailing winds mostly from the southwest (National Climatic Data Center, 1976). Winter and early spring exhibit mean wind speeds ranging from 4.5 to 5.4 m/s, surpassing the 4.0 to 4.5 m/s range observed in summer (National Climatic Data Center, 1976). Because our focus was on understanding living shoreline performance under high-energy conditions, we chose to study winter conditions. In addition, the rock sill is modeled as a solid, non-erodible layer, when in reality, some wave energy is dissipated by gaps in the rock matrix of the sill. This likely overestimates the impact of the structure, and together with our focus on winter conditions, likely represents an upper estimate of erosion that could occur. Integrating our observations with those during times when inorganic and organic sediment deposition is favored (generally summer, with robust vegetation and calmer weather) is critical to understand the full annual cycle of sediment deposition and erosion that leads to net elevation change. The vegetation in the model is represented by rigid cylinders, modeling the effect of vegetation on flow by correcting the bed roughness (Baptist et al., 2005; 2007). This does not include the ecology of vegetation growth or dieback, nor does it allow the vegetation to be

uprooted or to bend, and constant plant characteristics (such as stem height and density) and vegetated area are maintained throughout the simulation. The impact of this simplification on our findings is likely minimal, as vegetation in winter generally has low stem densities and heights, and significant changes in plant stem height, density, or biomass production are unlikely to occur during an 8-day simulation. The simplification may lead to an overestimation of interactions between the flow and vegetation due to plant removal or an underestimation of interactions due to plant growth. Furthermore, while our study focused on a specific site, Sunset Island, the response of living shorelines to high-energy events can vary significantly depending on local environmental conditions, geomorphology, and anthropogenic factors. Therefore, caution should be exercised when extrapolating our findings to other sites without considering site-specific factors. However, to the best of our knowledge, this is the first study to focus on the performance of marsh rock-sill living shorelines under high-energy conditions and to explore the role of the bank (marsh and sill) and sill height. This provides an important first step for coastal managers and regulatory agencies seeking to improve coastal resilience in the face of sea-level rise.

### *2.5. Conclusions*

Our study found that mechanisms of marsh loss at the edge differ between living shorelines and natural marshes under high-energy conditions. Specifically, the natural marsh was eroded by undercutting at the scarp toe, triggering slumping and edge collapse; the living shoreline boundary was degraded through open-water conversion as ponds expanded landward of the rock sills. The open-water conversion process was highly associated with local elevation by a nonlinear correlation ($y = 0.30e^{-23.73x}$, $R^2 =$

0.934), with lower elevations showing more open-water in the living shoreline marsh. Variations in sediment and vegetation characteristics between the living shoreline and natural marsh might also contribute to the contrasting erosion patterns. The created living shoreline marsh exhibited higher stem height and particle sizes, as well as lower organic content and stem density compared to the natural marsh, which may drive differences in the stability of the marsh boundary. The model further demonstrated that the presence of rock sill caused a noticeable surge of bed shear stress behind it at the marsh edge, potentially contributing to the scouring and open water conversion. We noticed that substantial sediment transport occurred between the subtidal zone and the marsh platform during high-energy conditions. The scenario analysis indicated that an increase in the bank height (both sill and marsh) led to less erosion at the marsh edge of living shorelines. This study focuses on the open-water conversion at the marsh boundary of a mature rock sill living shoreline (17 years old) and further explores the role of the sill and bank height in preventing shoreline erosion, which can provide references to improve coastal resilience in the face of sea level rise for coastal managers and regulatory agencies.

# Chapter 3: Impacts of Rock Sill Placement on Sediment Dynamics and Marsh Stability in Living Shorelines

*Abstract*

Rock sills have been widely used at the seaward edge of the created marshes in living shorelines to mitigate erosion, stabilize shorelines, and enhance coastal resilience over recent decades. However, the influence of rock sill placement on sediment dynamics within the created marshes remains poorly understood. To address this gap, our study investigates two types of marsh sill living shorelines — one featuring tidal gaps and the other without — in comparison with an adjacent natural marsh in Ocean City, Maryland, USA. We examine differences in intertidal sediment and vegetation characteristics and surface elevation changes, along with offshore suspended sediment concentration (SSC). We build on previous work using Delft3D-SWAN to model sediment dynamics in marsh sill living shorelines by incorporating tidal gaps in the sills to assess differences in hydrodynamics and sediment dynamics.

Our findings indicate that although lateral erosion in the natural shoreline is significantly more extensive compared to those with rock sills, tidal gaps contribute to a significant elevation increase at the pocket beaches between these gaps. This suggests that while rock sills in living shorelines mitigate erosion at the marsh edge, they diminish sediment deposition on the marsh platform. Numerical modeling reveals that more erosion occurs at the marsh sill living shoreline with tidal gaps compared to the continuous one. However, during high-energy events, sediment flux to the marsh in the segmented sill living shoreline is notably higher than in the continuous counterpart. Overall, tidal gaps in rock sills have the potential to provide both horizontal and vertical stability to tidal marshes by reducing marsh edge erosion and enhancing tidal flushing and sediment import. Our study improves understanding

of sediment dynamics in marsh sill living shorelines and offers insights for the practical design of tidal gaps.

**Keywords:** Nature-based Solution; Living Shorelines; Sediment dynamics; Rock sills; Tidal gaps; Delft3D-SWAN; Drone survey

### *3.1. Introduction*

In the past decades, the degradation of coastal habitats and intensive development in the coastal zone has led to increasing attention to shoreline stabilization and coastal resilience around the world (Gittman et al., 2016a; Smith et al., 2018). Some traditional "hard" structures, such as bulkheads, revetments, seawalls, and breakwaters, have been extensively constructed along coastal shorelines (Dugan et al., 2011; Gittman et al., 2015). However, those hardened structures largely have negative ecosystem impacts on intertidal and nearshore habitats (Bilkovic and Mitchell, 2013; Prosser et al., 2018; Gittman et al., 2016b), leading to growing interest in alternative solutions. More recently, a variety of approaches using natural and nature-based features (NNBF; or nature-based solutions (NBS)) have been developed to stabilize shorelines and preserve ecosystem functions of coastal habitats by mimicking features of the natural environment (Currin, 2019; Sutton-Grier et al., 2015). Living shorelines are one type of NNBF comprised of a created fringing marsh commonly with adjacent rock sills, oyster reefs, tidal flats, etc. (Currin, 2019).

Marsh sill living shorelines (created marshes with adjacent rock sills) have been used extensively in the Chesapeake Bay over the years, especially in Maryland (Hardaway,

2017). Sills are usually low-elevation (near the low tide line) structures constructed parallel to the shoreline, then backfilled with clean sand to create a suitable height and slope for planted tidal marsh vegetation. The sills are used to dissipate wave energy and reduce the erosional pressure along the coastal shoreline (Polk et al., 2022). The wider and higher the marsh sill system the greater the ability to provide shore erosion control (Hardaway, 2017), although trade-offs with habitat requirements, especially vegetation in the created marsh, need to be carefully considered. Marsh sill living shorelines can outperform hardened shorelines during hurricanes by promoting vertical accretion and experiencing less damage (Smith et al., 2018; Polk et al., 2022). Numerical modeling research has also shown that rock sills contribute to a positive sediment balance in the created marshes, which helps stabilize bed levels and shorelines, especially in the case of extreme events (Vona et al., 2021). Living shoreline installation itself often extends the shoreline seaward, counteracting the effects of historical shoreline erosion (Palinkas et al., 2023). However, the effectiveness of living shorelines might be site-specific, with almost half of the living shorelines surveyed in North Carolina exhibiting erosion and another half exhibiting accretion (Polk and Eulie, 2018). In addition, the efficacy of the sill will diminish over time as sea-level rise gradually reduces the freeboard of the structure (Miller et al., 2022). If sea level increases rapidly without enough sediment supply to nourish the created marsh of the living shoreline, open-water conversion can occur at the marsh's edge, resulting in marsh loss (Sun et al., 2024).

In recent years, marsh sill living shorelines with tidal gaps, also called tidal openings or windows, through the sills have been encouraged to enhance hydrological connectivity (Smith, 2006), and allow access for marine fauna (i.e., fish and turtles) to the created marsh (Miller et al., 2022). Segmented sills are usually oriented perpendicular to the dominant incoming wave direction to maximize effectiveness. If waves come from multiple directions, chevron-shaped structures or staggered zig-zag structures can be used (Miller et al., 2022). Limited research has been performed to determine optimum gap width and frequency, though guidelines suggest gaps at least every 30 m (Hardaway et al., 2010). A special type of segmented sill living shoreline is the headland breakwater, characterized by tombolos or salients with a marsh or sandy beach behind (Hardaway, 1999). While tidal water can access marsh areas behind a continuous sill through pore spaces or via overtopping (Hardaway, 2017), gaps allow direct connection between intertidal and subtidal environments. The presence of gaps results in additional tidal water exchange, wave energy transmission, and sediment transport, which influences erosion/deposition in the created marsh (Miller et al., 2022). Scour has been observed along the shoreline behind the gaps as waves are allowed to penetrate this area at the marsh edge (Hardaway et al., 2010; Miller et al., 2022). However, the impacts of rock sills, either continuous or with gaps, on sediment dynamics in the created marshes of living shorelines are not well understood.

In this study, we compare sediment dynamics within the created marshes of two marsh sill living shorelines (one with a continuous sill and one with segmented sills)

to those in a natural marsh adjacent to one of the living shorelines in Ocean City, Maryland, USA. We use both field and numerical modeling approaches to address the main goals of (1) assessing elevation patterns within each study site over a ~1-year period, and (2) exploring differences in sediment transport that arise from gaps in the rock sill. This study improves our understanding of sediment dynamics in marsh sill living shorelines and provides references to promote the practical design of nature-based coastal defenses.

## *3.2. Methods*

### 3.2.1. Study Site

Two marsh sill living shorelines, one with a continuous rock sill, and the other with gaps, in the Maryland (MD) Coastal Bays, were selected for this study. The MD Coastal Bays is a restricted shallow coastal lagoon system (~ 1 m) located behind the barrier island of Delmarva Peninsula (Figures 3.1a and b; Boynton et al., 1996; Wazniak et al., 2004). The Bays have around 287.5 km² of water, approximately 399 km of shoreline, and nearly 141.64 km² of wetlands (Kang and Xia, 2020). The lagoon system includes a total of five coastal bays and one major river, including Assawoman Bay, Isle of Wight Bay, Sinepuxent Bay, Newport Bay, Chincoteague Bay, and St. Martin River (Figure 3.1b). There are two inlets, Ocean City Inlet in Maryland and Chincoteague Inlet in Virginia. Because of the limited freshwater discharge and constricted inlets, the interior circulation of the bays is poor (Pritchard, 1960; Kang et al., 2017), which contributes to relatively high salinity (> 25) in most parts of the bays except near creeks dominated by freshwater flow (Wang et al.,

2013). The Bays are mostly fringed by salt marsh with some shoreline hardening on the west side of Sinepuxent, Newport, and Chincoteague Bay (Ganju et al., 2017) and the east side of the Assawoman and Isle of Wight Bay.

The continuous sill living shoreline is situated at Sunset Island in Ocean City, MD, near the boundary between Assawoman and Isle of Wight Bays, north of the Ocean City Inlet (Figures 3.1a and b). The living shoreline was installed in 2007, combining marsh restoration with a shore-parallel, low-rising sill at the edge made of granite rocks, aiming to protect vegetation closer to the land (Smith et al., 2018). As measured in ArcGIS 10.8.1, the continuous sill living shoreline marsh spans approximately 200 m in length, with an average width of 10 m (Figure 1c). The sills, about 1 meter in width and positioned at the marsh edge, are currently (in 2023) slightly below the mean water level for the sections with open-water conversion and slightly higher for sections without open water. Next to the marsh sill living shoreline, there is a natural marsh shoreline (70 m long and 10 m wide) that serves as a reference (Figure 3.1c). *Spartina alterniflora* (low marsh) and *spartina patens* (high marsh) dominate both the marsh sill living shoreline and natural marsh. Field data and the numerical model developed for Sunset Island by Sun et al. (2024) are used in this study, along with new data (aerial imagery from drones) and a modified model setup, to compare with observations from Assateague State Park.

The segmented sill living shoreline is located in Assateague State Park along Sinepuxent Bay, south of the Ocean City Inlet (Figures 3.1a and b). The living

shoreline is comprised of a created marsh and segmented rock sills with periodic gaps (Figure 3.1d). Before construction, the shorelines had been eroding rapidly at a rate of nearly a meter per year (https://www.ecosystemrestoration.com/assateaguestatepark). The living shoreline project was completed in 2018. It utilized large boulders, cobble, clean sand fill, and native wetland vegetation to build a series of 10 headland vegetated tombolos. The segmented rock sill living shoreline spans a length of about 200 m and the maximum width of the marsh is about 70 m (Figure 3.1d). The tombolos have an average width of about 10 m with a Gap/Rock ratio of 1:1. The dominant species in the created marsh are *Spartina alterniflora*, *Spartina patens* and *Phragmites australis*.

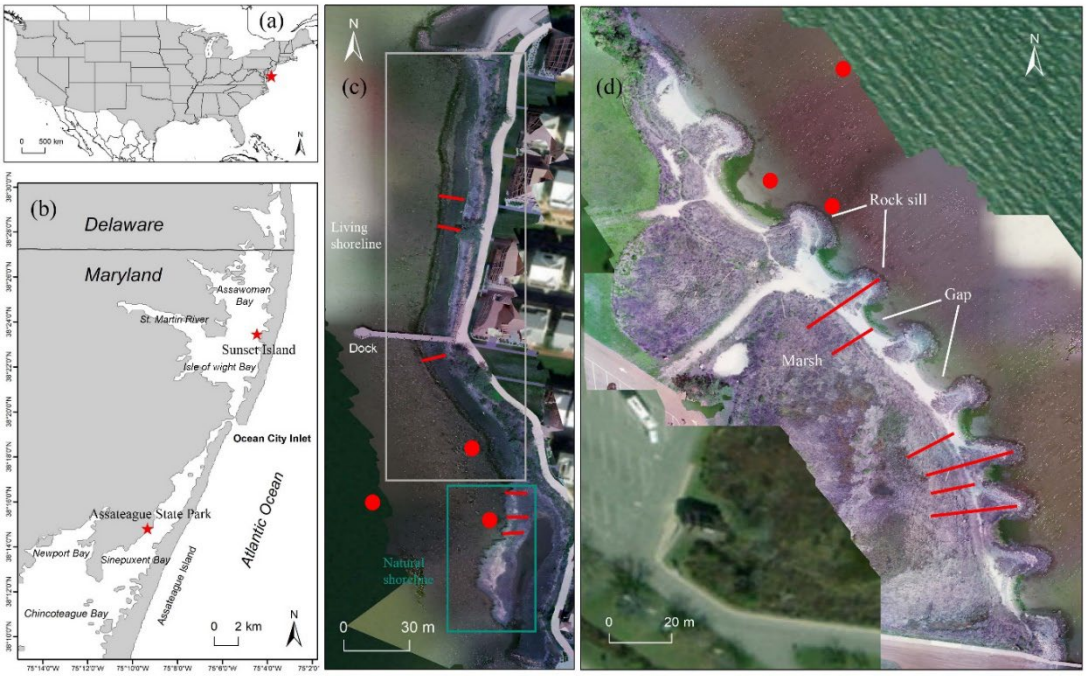


Figure 3.1. Location of study sites (a and b); red lines denote the locations of transects and red dots indicate the location of turbidity sensors at Sunset Island (c)

and Assateague State Park (d). The images in c and d were obtained via drone on April 26, 2022.

### 3.2.2. Field and Lab Methods

Field sampling was conducted twice a year, during the growing season (April or July) and in October near the end of the growing season, in 2021 and 2022. Transects were established perpendicular to the shoreline. At Sunset Island, there were three transects across the living shoreline marsh and three transects across the natural marsh (Figure 3.1c). At Assateague State Park, there were three transects across the rock sills and three transects across the gaps (Figure 3.1d). Field data for Sunset Island were reported by Sun et al. (2024). Identical protocols are used in this study to facilitate comparison.

Elevation was measured with a geodetic GNSS (GPS + GLONASS) receiver in Real-Time Kinematic (RTK) mode. For GNSS RTK with a single base station, an accuracy of ~1 cm horizontal and ~2 cm vertical can be achieved (Taddia et al., 2021). The instrument's base was placed at a benchmark closest to each site during the measurement (https://geodesy.noaa.gov/datasheets/; see Table S3.1). The coordinates were recorded in NAD83(NSRS2007) / UTM zone 18N reference system, and elevations referred to the NAVD 88 vertical datum.

Vegetation sampling points were established at each transect with a distance of 0 m, 2.5 m, and 5 m to the adjacent shoreline. Following Nardin et al. (2021), stem height

(m), diameter (mm), and density (#/$m^2$) were measured at each sampling point using 0.01 $m^2$ quadrats. Stem height was determined by averaging the heights of the 5 tallest individual stems within each quadrat. Stem diameter was calculated by averaging measurements of 5 stems at a height of 15 cm from the soil surface using a Vernier caliper. Stem density was determined by counting the number of stems inside the quadrat. For the marsh edge where vegetation erosion occurred, the corresponding data were marked as missing.

Push cores (5-10 cm long) were collected in the mid-intertidal zone with a distance of 2.5 m to the adjacent shoreline at each transect and returned intact to the lab for processing. In the lab, cores were sectioned into 1-cm increments. The top 2 increments (0-1 and 1-2 cm depth) were analyzed for grain size (D50, μm), organic matter content (%), and $^7$Be-derived sedimentation rate (g/$cm^2$/y) following Palinkas et al. (2013). Grain size analyses were performed by adding sodium metaphosphate to samples and placing them in a sonicator for disaggregation. Samples were then wet-sieved to separate the mud fraction (<64 μm) from the sand-sized fraction (>64 μm). The sand fraction was then subjected to dry sieving with a standard set of 13 sieves ranging from 64 μm to 500 μm. All data were used to calculate the median diameter (D50). Organic matter content was measured via combustion at 450 ◦C for 4 h and then calculated as the percentage of mass loss. Sedimentation rates were determined from the naturally occurring radioisotope $^7$Be (half-life 53.3 days), which has been previously used to capture seasonal sedimentation in marshes (Palinkas et al., 2013; Russ and Palinkas, 2018; Palinkas et al., 2023; Sun et al., 2024). $^7$Be activities were

measured via gamma spectroscopy and used to calculate sedimentation rates following Palinkas et al. (2013).

Three turbidity sensors were deployed at each site to investigate the spatial distribution of suspended sediment concentration (SSC, $kg/m^3$). At Sunset Island, one turbidity sensor was deployed in front of the living shoreline, one in front of the natural marsh, and one 10 m offshore of the shoreline, respectively (Figure 3.1c; Sun et al., 2024). At Assateague State Park, we placed one turbidity sensor in front of a rock sill, one in front of a gap, and one offshore 10 m away from the shoreline (Figure 3.1d). Deployment at Sunset Island was conducted from 23 February to 1 March 2023, and the deployment in Assateague State Park was from 27 May to 1 June 2023; both deployments were intended to capture relatively high-energy conditions. Turbidity was measured by a YSI 600OMS V2 Optical Monitoring Sonde equipped with a 6136 turbidity sensor. Turbidity measurements were converted to SSC through laboratory calibrations using water samples collected *in situ* from field (n=2) and also created in the lab (n=10; Coleman et al., 2020). See Figure S3.1 for calibration results.

### 3.2.3. Acquisition and Processing of Drone Images

A DJI Phantom 3 Professional (DJI-P3P) drone was used to capture aerial images and data to create Digital Terrain Models (DTMs) (see Table S3.2 for drone and camera specifications). Drone surveys were conducted on the same day for both sites, April 26, 2022 and May 24, 2023, with image acquisition at 40 m altitude to obtain an image resolution of about 2 cm. All surveys were performed in the mid-low tide. The

flights for both Sunset Island and Assateague State Park were performed within the same day with a break of about 2 hours. A set of Ground Control Points (GCPs) and Check Points (CPs) were deployed before the flight for model georeferencing. GCPs are specific points on the ground with precisely known coordinates used to align and georeference aerial or satellite imagery, ensuring accurate mapping. CPs are similarly precise points used independently of the georeferencing process to verify and validate the accuracy of the mapped images. A square target of about 60 cm × 60 cm was set at each GCP/CP to illustrate its location on the acquired images. We then collected the coordinates of the GCPs and CPs by GNSS RTK survey (Figure S3.2). In addition, Validation Points (VPs) were recorded along each transect for an accurate assessment of the intertidal marsh (Figure S3.2). The photogrammetric model reconstruction was performed using Agisoft PhotoScan/Metashape Professional software (Nardin et al., 2021; Taddia et al., 2021). The residuals of GCPs and CPs computed for each flight are shown in Table S3.3. The resolution of drone-derived elevations is ~2 cm. Sunset Island generally has short and sparse vegetation, and data were grouped by location: north living shoreline, south living shoreline, and natural marsh (Figure 3.1c). Vegetation at Assateague State Park is taller and denser, and so data were grouped by vegetated (marsh) and unvegetated (sand) locations. Based on the special design of the living shoreline, we chose 5 characteristic unvegetated sites to describe the spatial distribution of elevation change around the tombolos.

### 3.2.4. Numerical Model Settings and Validation

The spatially resolved and process-based Delft3D FLOW/MOR model (Lesser et al., 2004) coupled with the nearshore phase-averaged wave model SWAN (Booij et al.,

1999) has been widely used to simulate hydrodynamics and sediment transport in coastal marshes. We adopted a geomorphic model of the Sunset Island marsh sill living shoreline developed in Delft3D-SWAN by Sun et al. (2024). The model incorporated modules for flow, wave, and sediment transport, and considered the presence of vegetation and rock sills. Following Vona et al. (2021), the rock sill was incorporated into the model as a non-erodible structure (1 m in width) by setting the spatially varied erodible sediment depth as 0. Vegetation with a stem height of 0.26 m and density of 96 #/$m^2$ was placed in the model immediately adjacent to and landward of the rock sill. Our study site is dominated by *S. alterniflora* in the living shoreline and the vegetation in winter was generally rigid with low stem densities and heights. Therefore, the model took vegetation as rigid cylindrical structures and resolved vegetation effects in the momentum balance equation (Baptist, 2005; 2007). Changes in marsh surface elevation are dictated by the balance between erosion, inorganic deposition through settling, and particle capture by vegetation. The role of organic production is not considered in the model, and so elevation changes are likely underestimated. Considering the small scale, three domains were nested in the model to reduce computational time in generating waves using the domain decomposition technique (Deltares, 2014). They include a large model domain (5 × 10 km) covering the Bays, a local model domain (1.5 × 2.5 km) spanning the shorelines with narrow marshes, and a small model domain (200 × 50 m) with a fine resolution based on a representative transect in the living shoreline at Sunset Island. Refer to Sun et al. (2024) for more details about the parameter selection and model skill validation.

Sun et al. (2024) report the results of model runs for the continuous sill living shoreline at Sunset Island. Here, we evaluate the effects of tidal gaps on sediment dynamics by using the same model set up and forcing conditions but inserting gaps every 10 m along the shoreline at the same Gap/Rock ratio (1:1) as the segmented sill living shoreline at Assateague State Park. We ran the model for the same 8-days as Sun et al. (2024), from February 21, 2023, to March 1, 2023. Spatial distributions of bed shear stress and depth-averaged velocity were analyzed to investigate the hydrodynamics in the living shoreline, and sediment flux to the marsh and sedimentation/erosion on the platform were calculated to describe the sediment dynamics. Results were compared to those in Sun et al. (2024) to assess potential differences due to the presence of gaps.

#### 3.2.5. Statistical Analyses

An independent-sample T-test or ANOVA test was used to examine the significance of sample differences. Pearson correlation analyses were used to quantify the correlation relationship between two datasets. The statistical analyses were performed in R.

## *3.3. Results*

#### 3.3.1. Assessment of Digital Terrain Models (DTMs) Accuracy

Validation of the DTMs with the Validation Points (VP) showed the accuracy of the DTMs varied in different regions. Figure 3.2 shows the correlation between the GNSS RTK measurements and elevations derived from the drone (DTM values); Table 3.1 reports the validation results for each region. At Sunset Island, elevations

from the RTK and drone agreed within ~1 cm in all three regions (natural marsh, south living shoreline, and north living shoreline), though the Root Mean Square Error (RMSE) value for the north living shoreline was slightly higher (Figure 3.2a and Table 3.1). At Assateague State Park, the average vertical error of the DTM was up to 18 cm (Figure 3.2b and Table 3.1), higher in vegetated regions. Due to the high uncertainty in vegetated regions, we did not use DTM-derived elevation data from the marsh platform to evaluate geomorphological changes at Assateague State Park. However, differences between the RTK- and DTM-derived elevations were much lower in unvegetated regions (sand), with a mean difference value of 1.1 cm and an RMSE of 2.1 cm. Thus DTM-derived elevations were used for Sunset Island and the unvegetated regions at Assateague State Park for further morphology analysis. Similar values were found for the other aerial surveys in this work.

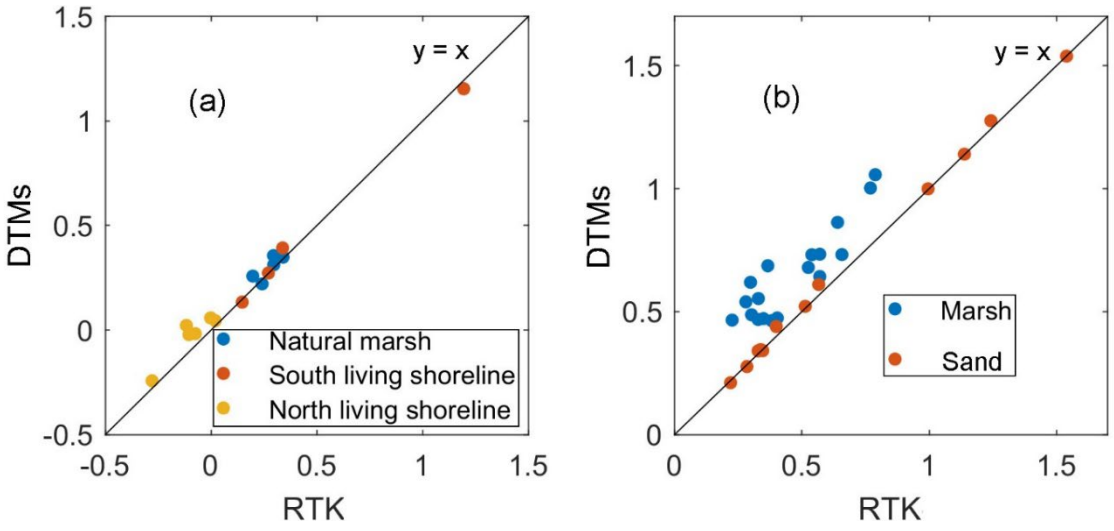


Figure 3.2. Assessment of Digital Terrain Models accuracy with GNSS RTK survey at Sunset Island (a) and Assateague State Park (b).

Table 3.1. Validation results of Digital Terrain Models (DTMs) in Sunset Island and Assateague State Park

| Study site | Region | Min difference (m) | Max difference (m) | Average (m) | RMSE (m) |
|---|---|---|---|---|---|
| Sunset Island | Natural marsh | -0.020 | 0.061 | 0.025 | 0.041 |
| | South living shoreline | -0.040 | 0.055 | 0.001 | 0.035 |
| | North living shoreline | 0.025 | 0.139 | 0.067 | 0.076 |
| Assateague State Park | Marsh (vegetated) | 0.071 | 0.321 | 0.180 | 0.198 |
| | Mudflat (unvegetated) | -0.009 | 0.044 | 0.011 | 0.021 |

3.3.2. Spatial Distribution of Elevation Digital Terrain Models (DTMs)

DTMs were constructed from high-resolution drone imagery collected at Sunset Island on April 26, 2022, and May 24, 2023 (Figure 3.3). The analysis revealed distinct patterns in the elevation distribution across different regions of the tidal marshes at Sunset Island. Notably, in the north living shoreline marsh, significant depressions were identified along the marsh boundary behind the sill, coinciding with areas of marsh boundary degradation and open water conversion. Additionally, a low-elevation spot observed in the south living shoreline marsh in the 2022 imagery (Figure 3.3a) was not present in the 2023 imagery (Figure 3.3b), indicating an

elevation gain at this location over the past year. In contrast, the elevation of the natural marsh, characterized by a jagged shoreline, was consistently higher than that of the living shoreline marsh in both sets of imagery. However, the 2023 imagery revealed a pronounced decrease in elevation along the jagged shoreline of the natural marsh compared to the 2022 data. This decrease in elevation is associated with the observed collapse at the scarp in the natural marsh, suggesting an ongoing elevation loss at the edge of the marsh. Regarding the frequency distribution of elevation, the peak of the elevation slightly shifted to the right, indicating an overall increase in elevation, while the distribution also expanded more to the left, suggesting that some areas of the marshes experienced an elevation decrease.

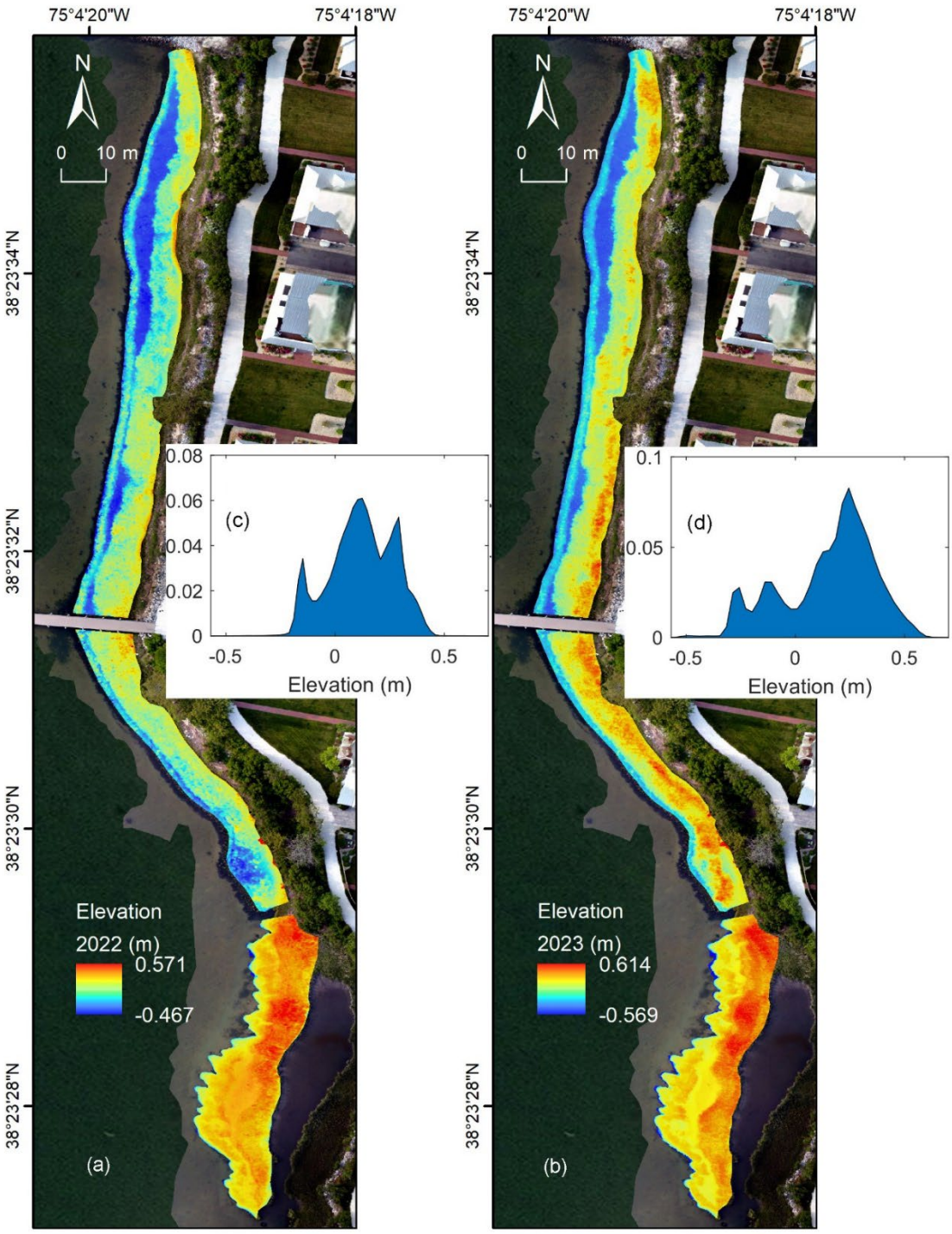


Figure 3.3. Digital Terrain Models (DTMs) and the frequency distribution for aerial images acquired on April 26, 2022 (a and c) and May 24, 2023 (b and d) at the marsh sill living shoreline in Sunset Island.

Similarly, DTMs were constructed by high-resolution imageries from the two drone flights at Assateague State Park (Figure 3.4). The elevation distribution in the living shoreline at Assateague State Park differed markedly from that at Sunset Island, primarily due to the unique design of tombolos. In particular, the elevation in the northern marsh was significantly higher than in the southern marsh. Additionally, the elevation along the shoreline in the unvegetated zones (sand) was substantially lower than in the intertidal marsh, a discrepancy possibly attributable to differences in vegetation coverage. The presence of vegetation may have introduced errors in the DTMs of the vegetated zones (marsh). Notably, a prominent elevation peak at the marsh boundary adjacent to the sand of the pocket beaches indicated a hotspot of high elevation, consistent with its unique geographic location.

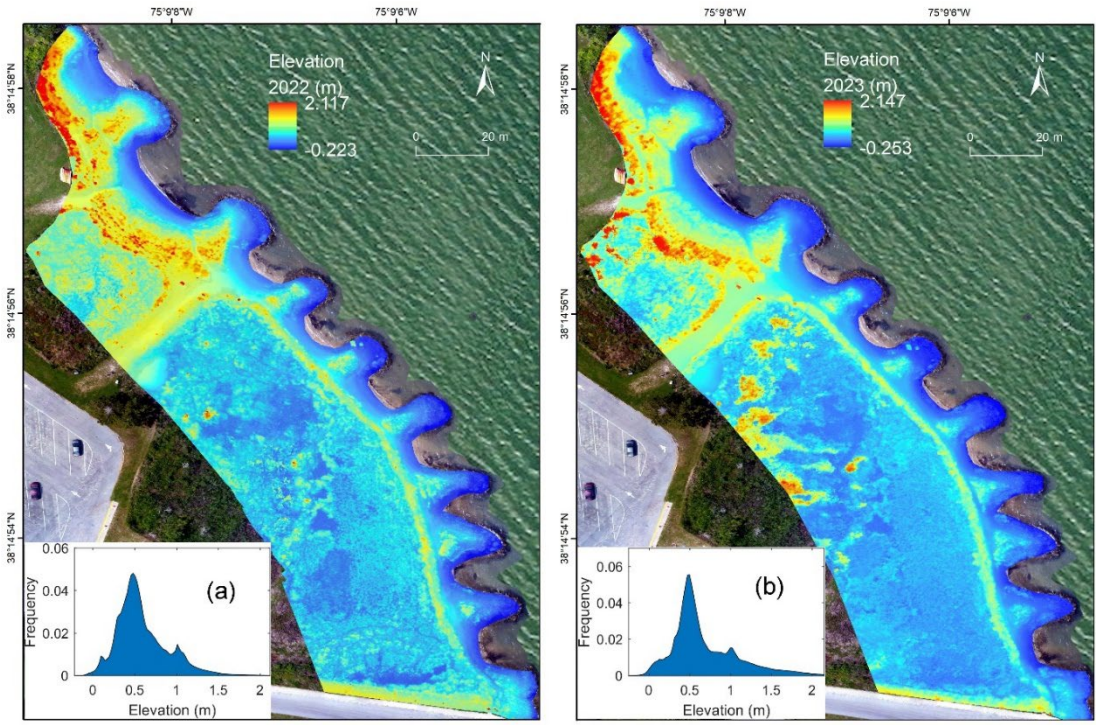

Figure 3.4. Digital Terrain Models (DTMs) and the frequency distribution for aerial images acquired on April 26, 2022 (a) and May 24, 2023 (b) at the marsh sill living shoreline in Assateague State Park.

### 3.3.3. Spatial Distribution of Elevation Change

The DTMs obtained on April 26, 2022, were subtracted from those on May 24, 2023, to calculate elevation changes. At Sunset Island, distinct patterns were observed across the three regions (Figure 3.5). The north living shoreline exhibited a broader band of elevation loss behind the sill compared to the south living shoreline, which showed less elevation gain landward of the sill (Figure 3.5d). Conversely, the south living shoreline displayed areas with the highest elevation gain, while the natural marsh exhibited more modest changes within its boundaries compared to either area of the living shoreline. Notably, a narrow band of dark blue along the shoreline of the natural marsh indicated edge collapse. When averaging elevations by distance from the shoreline in each area, a significant decrease in elevation was observed within 1 m of the natural marsh shoreline (-0.09 ± 0.15 m at 0.5 m from the shoreline, $p < 0.01$; Figure 3.5c). In the south living shoreline, where vegetation was immediately adjacent to the sill and landward, elevation change was negligible within 1 m of the sill, increased to approximately 0.16 m at 3.5 m, and then decreased to approximately 0 m at 7.5 m from the sill (Figure 3.5b, $p < 0.01$). In the north living shoreline, characterized by a gap between the vegetation and the rock sill, there was a significant decrease in elevation within 2 m of the sill ($p < 0.01$, Figure 3.5c). However, from 2 to 8 m from the rock sill, vertical elevation changes consistently

remained positive ($p < 0.01$, Figure 3.5c). Notably, the point cloud exhibited two "dark" areas around 2.5-3.5 m from the sill, indicating a scarp at the edge of the north living shoreline marsh (with the vegetation edge approximately 2-3 m away from the sill).

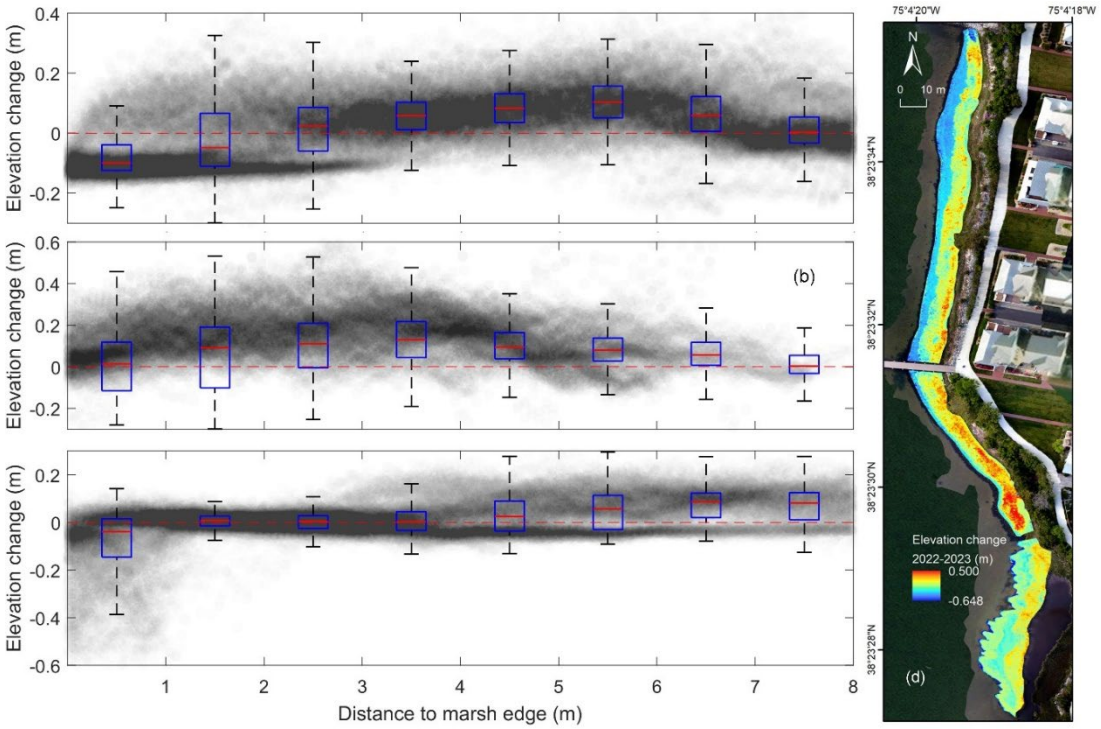


Figure 3.5. Spatial distribution of vertical elevation change (m NAVD88) at Sunset Island from 2022 to 2023. Vertical elevation changes at the (a) north living shoreline marsh, (b) south living shoreline marsh, and (c) natural marsh with respect to the distance to marsh edge (m). (d) Spatial distribution of vertical elevation changes at Sunset Island.

At Assateague State Park, due to the dense, tall marsh vegetation, we utilized elevation data from unvegetated sites (sand) for further morphological analysis.

Specifically, we selected 5 representative sites based on their geomorphic settings to characterize tombolo features (Figure 3.6a). Elevation changes were calculated by averaging pixel values within 1 m of each site (Figure 3.6b). Behind the rock sills (site A), there was a decrease in elevation (average change of -0.04 ± 0.07 m, $p <$ 0.01), whereas elevation changes were near zero at sites B (between the tombolo and back marsh) and E (right side of the pocket beach). Elevation increased at sites C (left side of the pocket beach) and D (middle of the pocket beach). Overall, elevation decreased immediately landward of the rock sill but showed an increase at the middle of the pocket beach within the gap.

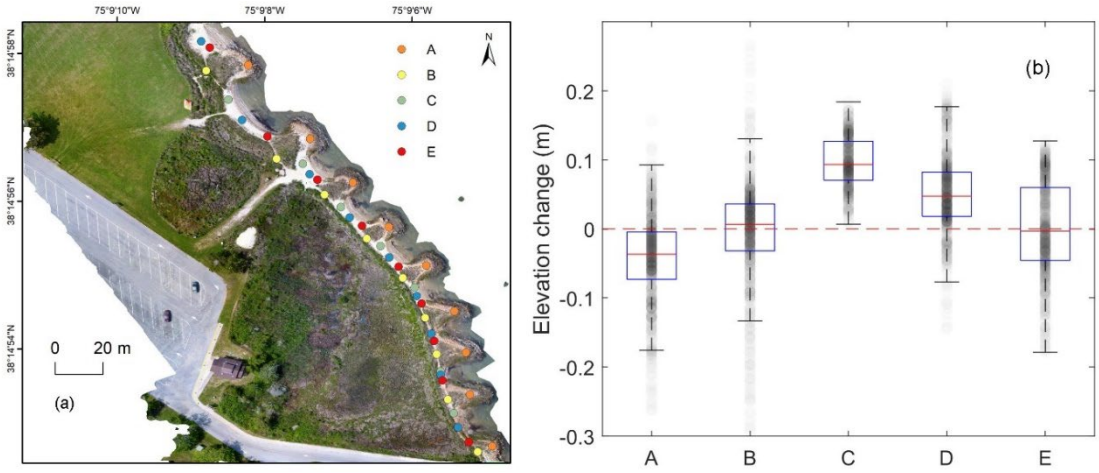


Figure 3.6. Spatial distribution of vertical elevation change (m) at the Assateague State Park from 2022 to 2023. (a) Colorful dots indicate the locations where spatial data was sampled, highlighting five typical features of the constructed tombolo; (b) boxplot illustrating the elevation change at these five typical features of the constructed tombolos.

### 3.3.4. Sediment and Vegetation Characteristics in the Living Shorelines

A previous study on the marsh sill living shoreline at Sunset Island (Sun et al., 2024) reported observations of vegetation and sediment characteristics, as well as SSC. A data summary is provided in Table 3.2 for ease of comparison with observations at Assateague. Though vegetation in the living shoreline had greater stem heights and diameter, the vegetation in the natural marsh had higher stem density ($p < 0.01$; Table 3.2). This is likely due to the varying dominant species in the marshes. The living shoreline marsh was primarily planted with *Spartina alterniflora*, while the natural marsh was mainly dominated by *Spartina patens*. Sediment in the living shoreline marsh had larger sediment grain sizes ($p < 0.01$), lower organic content ($p < 0.01$), and lower sedimentation rates ($p < 0.05$) compared to the natural marsh. In general, SSC adjacent to the natural marsh was higher than that adjacent to the living shoreline, with much lower SSC offshore. This suggests that shoreline erosion serves as a primary sediment source to the nearshore area, with more pronounced erosion adjacent to the natural marsh than the living shoreline.

Table 3.2. Vegetation and sediment characteristics of the marsh sill living shoreline with a continuous sill in Sunset Island (Sun et al., 2024).

| Category | Parameter | Natural marsh | Living shoreline | *p*-value |
|---|---|---|---|---|
| Vegetation characteristics | Stem height (m) | 0.385±0.028 | 0.748±0.058 | *$p < 0.01$ |
| | Stem diameter (mm) | 1.946±0.090 | 5.238±0.411 | *$p < 0.01$ |
| | Stem density (#/m$^2$) | 226±20 | 116±11 | *$p < 0.01$ |
| Sediment characteristics | Grain size (μm) | 142±5 | 173±6 | *$p < 0.01$ |
| | Organic matter content (%) | 4.6±0.7 | 1.6±0.2 | *$p < 0.01$ |
| | Sedimentation rate (g/cm$^2$/y) | 0.477±0.112 | 0.278±0.098 | *$p < 0.05$ |
| Sediment availability | SSC (kg/m$^3$) | 0.021±0.039 | 0.012±0.011 | *$p < 0.01$ |

Note: SSC stands for Suspended Sediment Concentration.

At Assateague State Park, vegetation behind the rock sills had relatively higher stem height and density and lower stem diameter compared to vegetation within the gaps. However, significant differences were only found in stem diameter between transects across the rock sills and the gaps ($p < 0.02$; Table 3.3). Sediments on behind the rock sills had significantly larger grain sizes and lower organic matter content compared to sediments within the gaps ($p < 0.01$ for both; Table 3.3). Although the average

sedimentation rate was higher behind the rock sills compared to the gaps, this difference was not statistically significant ($p < 0.3$; Table 3.3). SSC offshore was $0.066 \pm 0.088$ kg/m$^3$, which was significantly lower than the nearshore region ($p < 0.01$). SSC was higher in front of the rock sills $0.131 \pm 0.086$ kg/m$^3$ than in front of the gaps ($0.098 \pm 0.053$ kg/m$^3$; $p < 0.01$; Table 3.3).

Table 3.3. Vegetation and sediment characteristics of the marsh sill living shoreline with segmented sills in Assateague State Park.

| Category | Parameter | Gap | Rock | *p*-value |
|---|---|---|---|---|
| Vegetation characteristics | Stem height (m) | 0.511±0.032 | 0.581±0.026 | $p < 0.10$ |
| | Stem diameter (mm) | 1.703±0.174 | 1.332±0.047 | $*p < 0.02$ |
| | Stem density (#/m$^2$) | 246±23 | 298±25 | $p < 0.20$ |
| Sediment characteristics | Grain size (µm) | 194±40 | 391±15 | $*p < 0.01$ |
| | Organic matter content (%) | 32.1±7.1 | 3.4±0.9 | $*p < 0.01$ |
| | Sedimentation rate (g/cm$^2$/y) | 0.337±0.139 | 0.537±0.186 | $p < 0.30$ |
| Sediment availability | SSC (kg/m$^3$) | 0.098±0.053 | 0.131±0.086 | $*p < 0.01$ |

Note: SSC stands for Suspended Sediment Concentration.

### 3.3.5. Hydrodynamic Modeling

The geomorphic model, originally parameterized and validated by Sun et al. (2024) for the continuous sill living shoreline at Sunset Island, was adapted by introducing gaps in the rock sill. The model simulations were conducted over the same 8-day period (from February 21, 2023, to March 1, 2023). Throughout this duration, bed shear stresses were generally higher during ebb tide compared to flood tide, regardless of whether the sill was continuous or segmented. In the case of the continuous sill living shoreline, the maximum bed shear stress occurred immediately landward of the sill at the marsh edge during both flood (Figure 3.7a) and ebb (Figure 3.7c) tides, gradually decreasing towards the interior of the marsh. Conversely, for the segmented sill living shoreline, zones of elevated bed shear stress were located approximately 1 m landward of the sill, with notable "hotspots" of heightened stress directly behind the gaps (Figures 3.7b and d). During flood tide, depth-averaged velocities (indicated by arrows in Figures 3.7a and b) were directed landward, transporting sediments towards the marsh; during ebb tide, depth-averaged velocities shifted seaward (arrows in Figures 3.7c and d). These flow patterns contributed to distinct patterns of modeled elevation change between continuous and segmented sill living shorelines (Figures 3.7e and f). In simulations with the continuous sill living shoreline, erosion primarily occurred immediately behind the sill, transitioning to deposition further inland in a relatively uniform spatial pattern. However, in simulations with segmented sill living shoreline, significant sediment deposition occurred within the gaps of the rock sill, while erosion was concentrated immediately landward of the gaps, extending ~2 m inland from the rocks (Figure 3.7f).

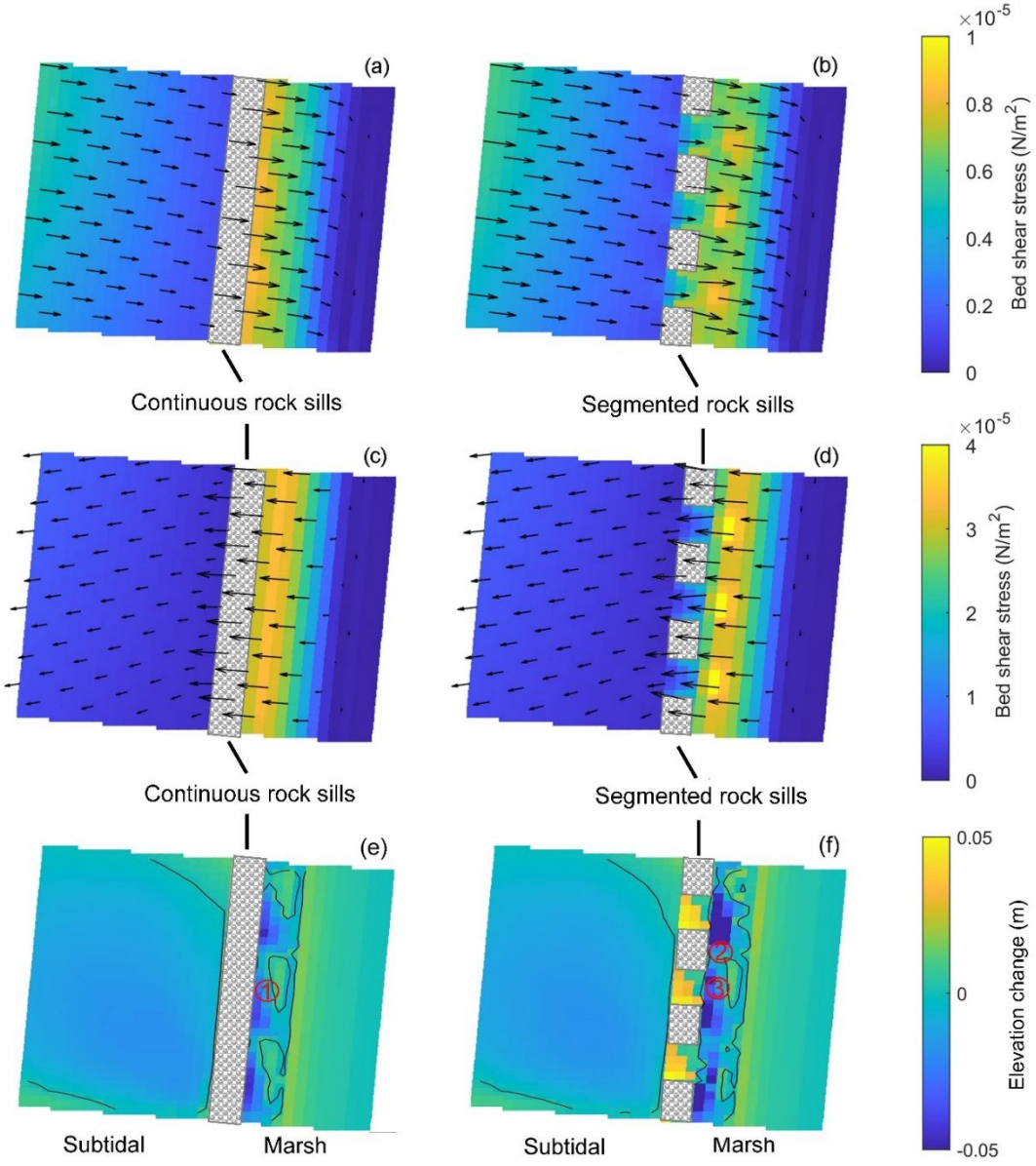


Figure 3.7. Spatial distribution of modeled hydrodynamic conditions and morphology change in the marsh sill living shoreline with different gap configurations. Spatial distribution of bed shear stress ($N/m^2$) and depth average velocity (m/s) at (a) continuous sill living shoreline during flood tide, (b) segmented sill living shoreline during flood tide, (c) continuous sill living shoreline during ebb

tide, (d) segmented sill living shoreline during ebb tide. Spatial distribution of elevation change (m) at (e) continuous sill living shoreline and segmented sill living shoreline (f). Contour lines denote where the elevation change equals 0 m. Red numbers demonstrate where samples were taken for time series variation in Figure 3.8b-d, including (1) continuous sill (2) segmented sill – rock, and (3) segmented sill – gap.

Time-series analyses of bed shear stress, depth-averaged velocity, and bed elevation change provide insights into sediment dynamics driving elevation changes. Three specific locations were examined: at the marsh edge of the continuous sill, behind the rock of the segmented sill, and behind the gap in the segmented sill (Figures 3.7e and f). Bed shear stresses showed consistent patterns across these locations, with higher values observed behind the gaps (up to $1.27 \times 10^{-3}$ N/m$^2$) compared to behind the rocks (up to $0.81 \times 10^{-3}$ N/m$^2$) during the high-energy event from February 24 to February 25 (Figures 3.8a and 3.8b). Depth-averaged velocities exhibited a similar trend (Figure 3.8c). Elevation changes occurred concurrently at these locations but varied in magnitude. For instance, between February 23 and 24, bed elevation decreased by $6.98 \times 10^{-3}$ m behind the continuous sill, $9.98 \times 10^{-3}$ m behind the segmented sill rock, and $16.4 \times 10^{-3}$ m behind the segmented sill gap. Subsequently, a significant elevation increase occurred during a wind event from February 24 to 25, with the peak wind speed exceeding 10 m/s blowing towards the shorelines. Elevation gain was more pronounced behind the gaps of the segmented sill (Figures 3.8a and d). This wind event triggered significant sediment import and reduced erosion in the area

around the segmented rock sill living shoreline (Figures 3.8e and f). Throughout the simulation, bed elevation increased by $4.6 \times 10^{-3}$ m behind the continuous sill and by $1.3 \times 10^{-3}$ m behind the rocks of the segmented sills, while decreasing by $8.5 \times 10^{-3}$ m behind the gaps. By the end of the simulation, more sediment was exported with the segmented sill design, leading to a larger erosion area (Figures 3.8e and f).

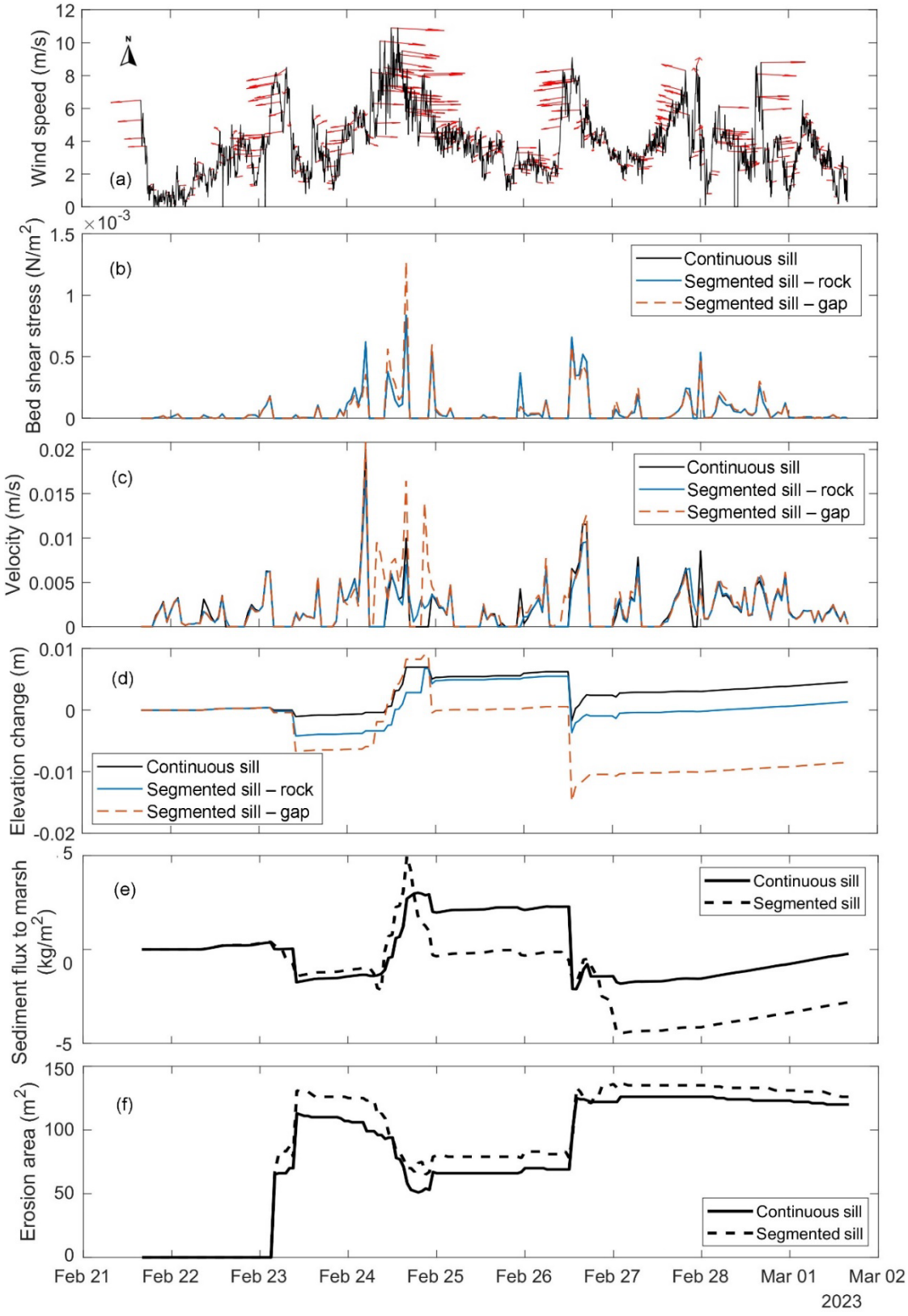
Wind speed (m/s)
(a)
Bed shear stress (N/m$^2$)
$\times 10^{-3}$
(b)
Continuous sill
Segmented sill – rock
Segmented sill – gap
Velocity (m/s)
(c)
Elevation change (m)
(d)
Sediment flux to marsh (kg/m$^2$)
(e)
Continuous sill
Segmented sill
Erosion area (m$^2$)
(f)
Feb 21
Feb 22
Feb 23
Feb 24
Feb 25
Feb 26
Feb 27
Feb 28
Mar 01
Mar 02
2023

Figure 3.8. Input wind (a; arrows indicate the wind direction) and model results of bed shear stress ($N/m^2$; b), depth average velocity (m/s; c), and elevation change (m; d) at the marsh edge of the continuous and segmented sill living shorelines, as well as cumulative sediment flux to the marsh ($kg/m^2$) and erosion area ($m^2$; f) of continuous and segmented sill living shorelines. Cumulative sediment flux to the marsh and erosion area were averaged over the whole marsh.

### *3.4. Discussion*

Marsh sill living shorelines are widely acknowledged for their potential to attenuate wave energy (Nardin et al., 2021; Leone and Tahvildari, 2023), reduce shoreline erosion (Hardaway, 2017; Palinkas et al., 2023), and improve coastal resilience (Gittman et al., 2016a; Smith et al., 2018; Currin, 2019). However, sediment dynamics within the created marshes are not well understood, particularly concerning the differences between continuous and segmented rock sill designs. This study integrates field observations and numerical modeling to shed light on these dynamics and compare potential mechanisms of marsh loss in natural marshes and the created marshes of living shorelines.

Some natural marshes experience erosion caused by undercutting at the scarp toe, leading to slumping and edge collapse (Fagherazzi et al., 2013). Our observations at Sunset Island revealed a significant elevation decrease within 1 m of the marsh edge in the natural marsh ($-0.09 \pm 0.15$ m, $p < 0.01$; Figure 3.5c), indicating ongoing edge collapse. Notably, elevation increased noticeably beyond 2 m from the marsh edge (*p*

< 0.01), suggesting that lateral marsh edge erosion contributes sediment for vertical accretion, consistent with findings elsewhere (Hopkinson et al., 2018). For the continuous sill living shoreline at Sunset Island, elevation changes differed between the northern and southern portions. In the north living shoreline marsh, evident ponding occurred between the vegetation and the rock sill, converting the vegetated area to open water (Sun et al., 2024), and elevation decreased immediately landward of the sill (Figure 3.5a). This aligns with modeling results showing higher bed shear stresses immediately landward of the sill structure during high-energy conditions (Figure 3.7), which may erode sediment at the marsh edge and/or prevent sediment deposition. In contrast, no ponding was observed in the southern portion, and elevation increased consistently across the intertidal marsh (Figure 3.5b), likely due to the relatively higher elevation in the south living shoreline marsh. Elevation has been shown to correlate with open-water conversion in salt marshes, with lower elevation units demonstrating more open-water conversion (Ganju et al., 2020). Despite open-water conversion in the north living shoreline marsh, erosion in the living shorelines was less extensive compared to the natural marsh experiencing significant edge collapse. Additionally, higher SSC was observed in front of the natural marsh, along with higher sedimentation rates on the natural marsh platform (Table 3.2). These findings align with previous studies indicating that marsh frontal erosion alters sediment export dynamics (Li et al., 2018, 2019), but the marsh platform can maintain elevation at the expense of total marsh area (Hopkinson et al., 2018). Overall, these results suggest that continuous sill living shorelines effectively

mitigate shoreline erosion (Hardaway, 2017; Palinkas et al., 2023) but may reduce the sediment supply needed to build elevation in created marshes.

Segmented sill living shorelines have gained increasing attention over continuous sill designs for enhancing eco-hydrological connectivity between nearshore subtidal and intertidal marshes (Miller et al., 2022). While tidal water can access marsh areas behind continuous sills through pore spaces or via overtopping (Hardaway et al., 2017), gaps in segmented sills enhance tidal water exchange and wave energy transmission (Miller et al., 2022), potentially leading to diverse sediment dynamics within created marshes. Our study reveals that sediment dynamics in segmented sill living shorelines exhibit greater spatial variability compared to continuous sill designs. Specifically, elevation behind the rock sills decreased ($p < 0.01$), whereas elevation in the gaps increased ($p < 0.01$) in the segmented sill living shoreline at Assateague State Park (Figure 3.6). Correspondingly, SSC was significantly lower in the gaps compared to in front of the sills ($p < 0.01$), and sedimentation rates in the marsh were slightly lower behind the gaps than behind the sills (Table 3.3). In addition, elevation increased noticeably on the left side of the pocket beach (sites C), whereas there was minimal change on the right side (sites E), indicating the possible influence of the longshore current on sediment dynamics.

The modeling results provide further insights into the differences between continuous and segmented sill living shorelines from a hydrodynamic perspective, using the same model configuration, forcing, and duration for both designs. In the continuous sill

living shoreline, the maximum bed shear stress occurred immediately landward of the sill (Figures 3.7a and c), whereas in the segmented sill living shoreline, it was approximately 1-2 m landward of the gaps (Figures 3.7b and d). Notably, bed shear stress was significantly higher behind the gaps compared to behind the rocks during the high-energy event between February 24 and 25 (Figure 3.8b), potentially contributing to substantial sediment import. This observation aligns well with the simulated morphology changes observed. During a high-energy wind event from February 24 to 25, we observed significant sediment import and a reduction in erosion area at the segmented sill living shoreline (Figures 3.8e and f). High-energy events play a crucial role in sediment import to coastal salt marshes (Castagno et al., 2018; Vona et al., 2021; Zhu and Wiberg, 2022). Storm surge events, occurring 5% of the time, contribute 40% of marsh deposition (Zhu and Wiberg, 2022). Substantial sediment transport occurs between the offshore subtidal zone and the marsh platform in the continuous sill living shoreline during high-energy events. The total sediment flux to the marshes significantly increases when the wind blows toward the living shoreline and sharply decreases when blowing away from it (Sun et al., 2024). This study further confirms the significance of wind energy and its direction in sediment transport between subtidal nearshore areas and the intertidal marsh. Furthermore, we found that compared to continuous sill living shorelines, segmented sill living shorelines with tidal gaps exhibit greater dynamism, particularly behind the gaps (Figure 3.8d). These findings highlight the critical role of gaps in segmented sill living shorelines in sediment transport between the marsh platform and adjacent

nearshore subtidal areas, underscoring the importance of gap geometry as a key design consideration to enhance the sustainability of created marshes.

This study has several limitations that should be acknowledged. Firstly, the findings from our specific study location may not be fully generalizable to other marsh sill living shorelines with different scales, gap configurations, hydrodynamic conditions, geomorphology, and anthropogenic influences. However, focusing on living shorelines in a similar physical setting helps to minimize confounding factors such as weather and salinity, which would otherwise complicate the understanding of design-related differences. We deliberately configured our model to replicate the gap/rock ratio and gap spacing of our selected segmented sill living shoreline. Currently, there is no consensus on the optimal gap geometry (Miller et al., 2022), and living shorelines with varying scales and gap configurations are likely to exhibit different sediment dynamics. This study serves as an initial step toward optimizing gap geometry in future designs. The 8-day simulation period of our model, intended to capture short-term responses to high-energy events, does not fully represent the range of conditions experienced throughout the year, including low-energy conditions conducive to sediment deposition. Our observations of elevation change are limited by the resolution of the Digital Terrain Models (DTMs). Over the course of a year, elevation changes largely fell within the resolution of the GNSS RTK measurements used for DTM calibration. This aligns with expectations, as elevation changes in marshes typically range from millimeters to centimeters (Taddia et al., 2021). While the elevations derived from RTK and DTMs generally agreed at Sunset Island

(characterized by short, sparse vegetation) and in unvegetated regions of Assateague State Park, significant discrepancies were observed in vegetated regions at Assateague State Park. This inconsistency is expected due to challenges posed by relatively dense vegetation (Taddia et al., 2021). Therefore, future drone surveys would likely be more effective if conducted during winter or spring when vegetation is less dense. Despite these limitations, this study provides valuable insights into the impacts of rock sill placement on sediment dynamics and shoreline stability in living shorelines. The findings contribute to a deeper understanding of the performance of marsh sill living shorelines in erosion control and the function of tidal gaps, offering a solid foundation for future research on gap configuration. We are confident that the outcomes of this research will inspire further investigations for shoreline design and coastal management.

### *3.5. Conclusions*

This study investigated two marsh sill living shorelines, one with a continuous sill and the other with segmented sills, adjacent to Ocean City Inlet in Maryland, USA. The study assessed changes in suspended sediment concentration (SSC), surface elevation, $^{7}$Be-derived sedimentation rate, vegetation characteristics, and sediment properties over a two-year field survey from 2021 to 2022. A model approach in Delft3D-SWAN was utilized to explore the impact of rock sills and their associated gaps on the spatial distribution of sediments. Preliminary findings indicated that while rock sills can help mitigate erosion at the marsh edge, they may reduce sediment deposition on the marsh platform. Overall, rock sills with gaps may have the potential to enhance both horizontal and vertical stability by reducing marsh edge erosion and

enhancing tidal flushing and sediment deposition. Future research will involve more extensive modeling work to validate sediment transport patterns in living shorelines with varying gap configurations (Gap/Rock ratio) in segmented rock sills on sediment flux to the marsh platform. This study aims to advance our understanding of sediment dynamics in marsh sill living shorelines and provide valuable insights for coastal managers and regulatory agencies to promote practical solutions for shoreline protection.

# Chapter 4: Metrics for Assessing Stability of Marsh Sill Living Shorelines: Identifying Main Drivers of Marsh Boundary Degradation

*Abstract*

Marsh sill living shorelines are ubiquitous nature-based features in coastal estuaries to mitigate shoreline erosion and enhance coastal resilience. Evaluating the stability of these structures is crucial for shoreline design and coastal management strategies. Although several metrics have been developed to assess the stability of natural tidal marshes, their suitability for the created marshes of living shorelines is still unclear. This research compiles and analyzes data from 18 marsh sill living shorelines in Maryland, USA — nine with continuous sills and nine with segmented sills. We characterize their eco-geomorphic features and hydrodynamics with 15 metrics through both field sampling and remote sensing. Among the 15 metrics, six representative ones are selected to identify the major factors influencing potential marsh boundary degradation in marsh sill living shorelines. Our findings indicate that the Unvegetated/Vegetated Ratio (UVVR) and sediment deposition rate, typically used for assessing natural marsh resilience, are also applicable to living shoreline marshes. These metrics demonstrate similar relationships with other environmental variables, such as marsh elevation and nearshore sediment concentrations, as observed in natural marshes. Multivariate analyses reveal that the Relative Exposure Index (REI) and Gap/Rock (G/R) ratio significantly contribute to potential marsh boundary degradation in living shorelines, while the elevation relative to Mean Sea Level and G/R ratio effectively differentiate between living shorelines with continuous sills and those with segmented sills. By integrating data across regional ecosystems, this study advances our understanding of potential degradation processes

in living shorelines, offering valuable insights for shoreline design and post-construction maintenance.

**Keywords:** Living shorelines; Nature-based features; Shoreline stability; Coastal resilience; Salt marshes; Multivariate analysis

### *4.1. Introduction*

Climate change and coastal urbanization have been accelerating the demand for reducing shoreline erosion and enhancing coastal resilience to storms and sea level rise (Gitmann et al., 2016; Kirezci et al., 2020). Traditional hardened structures, like seawalls, revetments, and dikes, have been extensively constructed along coastal shorelines for shore erosion control (Dugan et al., 2011; Gittman et al., 2015). However, these structures are costly to maintain and can negatively impact intertidal and nearshore habitats (Bilkovic and Mitchell, 2013; Prosser et al., 2018), leading to increased interest in exploring alternative solutions. Natural and nature-based features (NNBF), also known as nature-based solutions, have emerged as viable options for stabilizing shorelines while preserving coastal ecosystem functions (Sutton-Grier et al., 2015). These features, including dunes, salt marshes, mangroves, seagrasses, rock sills, and oyster reefs, may occur naturally in landscapes or be engineered, constructed and/or restored to mimic natural conditions (Currin, 2019).

Marsh sill living shorelines, consisting of a constructed fringing marsh with adjacent rock sills, are a preferred type of natural and nature-based feature (NNBF) for sites with low to moderate erosion rates (Polk et al., 2022; Miller et al., 2022). This

approach has been widely implemented in the Chesapeake Bay since the mid-1980s, particularly in Maryland (Hardaway, 2017). Sills are typically low-crested structures with a freeboard of approximately 0 to 0.3 m above Mean High Water (MHW), constructed parallel to the shoreline in areas with a small to moderate tidal range, then backfilled with clean sand to achieve a suitable height and slope for planted tidal marsh vegetation (Miller et al., 2022). In recent years, marsh sill living shorelines with tidal gaps, also referred to as tidal openings or windows, through the sills have been encouraged to enhance hydrological connectivity (Smith, 2006; Bilkovic et al., 2016) and allow access for marine fauna (e.g., fish and turtles) to the created marsh (Hardaway et al., 2017; Miller et al., 2022). While tidal water can access the intertidal marsh behind a continuous sill through pore spaces or via overtopping (Hardaway et al., 2017), gaps allow for additional tidal water exchange, wave energy transmission, and sediment transportation between intertidal and subtidal environments.

Previous studies have reported that, although living shorelines are generally effective at wave attenuation and erosion control, their performance can be site-specific (Vona et al., 2021; Polk and Eulie, 2018; Smith et al., 2018; Polk et al., 2022; Palinkas et al., 2023). Site-specific changes can be predicted using multiple linear regression models that consider structure type, shoreline erosion rate, dominant sediment source, and land use (Palinkas et al., 2018). Additionally, the effectiveness of sills diminishes over time due to rising sea levels, gradually reducing the freeboard of the structure (Miller et al., 2022). Recent research indicates that accelerated sea-level rise has caused mature marsh sill living shoreline boundaries to convert into open water as

ponds expand landward of rock sills, negatively impacting coastal marsh resilience and shoreline stability (Sun et al., 2024). Additionally, field observations in segmented sill living shorelines have revealed scouring along the shoreline behind gaps, attributed to waves penetrating this area at the marsh edge (Hardaway et al., 2010; Miller et al., 2022).

Assessing the ecosystem resilience of marsh sill living shorelines is crucial for informing shoreline design and coastal management. Various biotic and abiotic measurements have been developed to evaluate the vulnerability of natural tidal marshes. The success of coastal wetlands restoration is driven by sediment availability (Liu et al., 2021), and a reduction in the regional marsh area decreases sediment availability in coastal estuarine systems (Donatelli et al., 2020). Sediment deficits and open-water conversion serve as holistic and sensitive indicators of salt marsh vulnerability (Ganju et al., 2017). The marsh sediment budget ($Q_b$) provides a spatially integrated measure of competing constructive and destructive forces on sediment dynamics (Ganju et al., 2017). At landscape scales, $Q_b$ and sediment-based lifespan ($L_{sed}$) scale with the areal unvegetated/vegetated marsh ratios (UVVR), suggesting these metrics are useful indicators of marsh trajectory (Ganju et al., 2017). Elevation also consistently scales with the UVVR across systems, with lower elevation units demonstrating more open-water conversion and higher UVVRs (Ganju et al., 2020). However, no single metric universally predicts marsh trajectories, and a more robust approach rigorously combining a suite of spatially integrated, landscape-scale metrics was initially developed (Wasson et al., 2019). To

better integrate these influential factors, Defne et al. (2020) established a geospatially resolved wetland vulnerability index (WVI) by ranking values in each dataset to indicate relative vulnerability. Yet, no research has been performed to determine applicable metrics to evaluate ecosystem resilience and predict marsh trajectories of created marshes in marsh sill living shorelines at regional scales.

In this study, we integrate remote sensing and field sampling data from 18 marsh sill living shorelines (9 with continuous sills and 9 with segmented sills) in Maryland's Chesapeake Bay and Coastal Bays to evaluate marsh stability. We analyzed 15 metrics used to characterize eco-geomorphic features and hydrodynamic conditions of tidal marshes, comparing them between different sill types (continuous versus segmented) and ponding conditions (with ponding versus no ponding). Additionally, we introduced a novel metric, Functional Marsh Width ($W^*$, in m), to describe the vegetation distribution of the narrow fringing marsh band in living shorelines. The primary objectives of this study are: (1) to validate the applicability of potential metrics for assessing the stability of fringing marshes in marsh sill living shorelines, and (2) to investigate the main drivers of potential degradation in marsh sill living shorelines. This research advances our understanding of metrics for assessing the stability of marsh sill living shorelines and improves our insight into their post-construction trajectory.

## *4.2. Methods*

### 4.2.1. Study Site

In this study, we analyzed 18 marsh sill living shorelines located in Maryland's Chesapeake Bay and Coastal Bays (Figure 4.1). These sites were equally divided into two types: nine continuous sill living shorelines and nine segmented sill living shorelines (Table 4.1). The ages of the living shorelines at the time of sampling ranged from 3 to 15 years. The vegetation of all 18 living shoreline marshes was dominated by *Spartina alterniflora*, *Spartina patens*, and *Phragmites australis*. Data for SI and AS were derived from Sun et al. (2024), while data for the remaining continuous and segmented sill living shorelines were sourced from Palinkas et al. (2023) and Koontz (2025), respectively.

These sites experience similar tidal ranges and rates of relative sea-level rise. Two sites, SI and AS, were located in the MD Coastal Bays, which have a relative sea-level rise rate of 4.94 mm/y and an average tidal range of 0.64 m. The MD Coastal Bays is a shallow coastal lagoon system situated between the barrier island of the Delmarva Peninsula and the Atlantic Ocean and are polyhaline (Boynton et al., 1996; Wazniak et al., 2005). The other sites were located in the mesohaline region of the Chesapeake Bay, experiencing relative sea-level rise of ~4 mm/y and tidal ranges of ~0.3-0.5 m. While all of the sites are micro-tidal, significant wind-driven changes in water levels result from variations on the Atlantic continental shelf (Chuang and Boicourt, 1989) and from storms, which can flood extensive areas for hours to days (Gong et al., 2009). In the mid-bay, most wave action is generated locally and is

fetch-limited (Lin et al., 2002). While shoreline erosion is the predominant source of sediment in this region, substantial sediment can also be mobilized by overland flow during significant rainfall events (Hobbs et al., 1992).

Table 4.1 Name, install year, length, rock sill type, and sampling date for the 18 living shorelines in Maryland.

| Site | Install year | Length (m) | Rock sill type | Sampling date | Age during sampling (y) |
|---|---|---|---|---|---|
| Sunset Island (SI) | 2007 | 204.2 | Continuous | 2021-2022 | 14-15 |
| Queens Landing (QL) | 2005 | 172.9 | Continuous | Aug-2018 | 13 |
| Oppenheim (OP) | 2006 | 134.1 | Continuous | Aug-2018 | 12 |
| Ruesch (RU) | 2008 | 510.5 | Continuous | Jul-2018 | 10 |
| Hatton Garden (HG) | 2007 | 245.5 | Continuous | Jul-2018 | 11 |
| San Domingo (SD) | 2007 | 73.5 | Continuous | Jul-2018 | 11 |
| Environmental Concern (EC) | 2005 | 61.9 | Continuous | Oct-2017 | 12 |
| Myrtle Grove (MG) | 2004 | 246.0 | Continuous | Aug-2018 | 14 |
| Maritime Museum (MM) | 2008 | 53.2 | Continuous | Jul-2018 | 10 |
| Assateague State Park (AS) | 2018 | 212.1 | Segmented | 2021-2022 | 3-4 |

| | | | | | |
|---|---|---|---|---|---|
| Wye House East (WHE) | 2008 | 330.6 | Segmented | Aug-2023 | 15 |
| Wye House West (WHW) | 2009 | 371.9 | Segmented | Sep-2022 | 13 |
| Tred Avon (TA) | 2010 | 87.6 | Segmented | Aug-2022 | 12 |
| Narrows Pointe (NP) | 2016 | 567.6 | Segmented | Sep-2023 | 7 |
| Plaindealing Creek (PC) | 2010 | 90.3 | Segmented | Aug-2022 | 12 |
| Irish Creek (IC) | 2011 | 141.8 | Segmented | Sep-2022 | 11 |
| Conrad Gordon (CG) | 2013 | 186.4 | Segmented | Aug-2023 | 10 |
| Old Trinity Church (OT) | 2008 | 266.5 | Segmented | Sep-2023 | 15 |

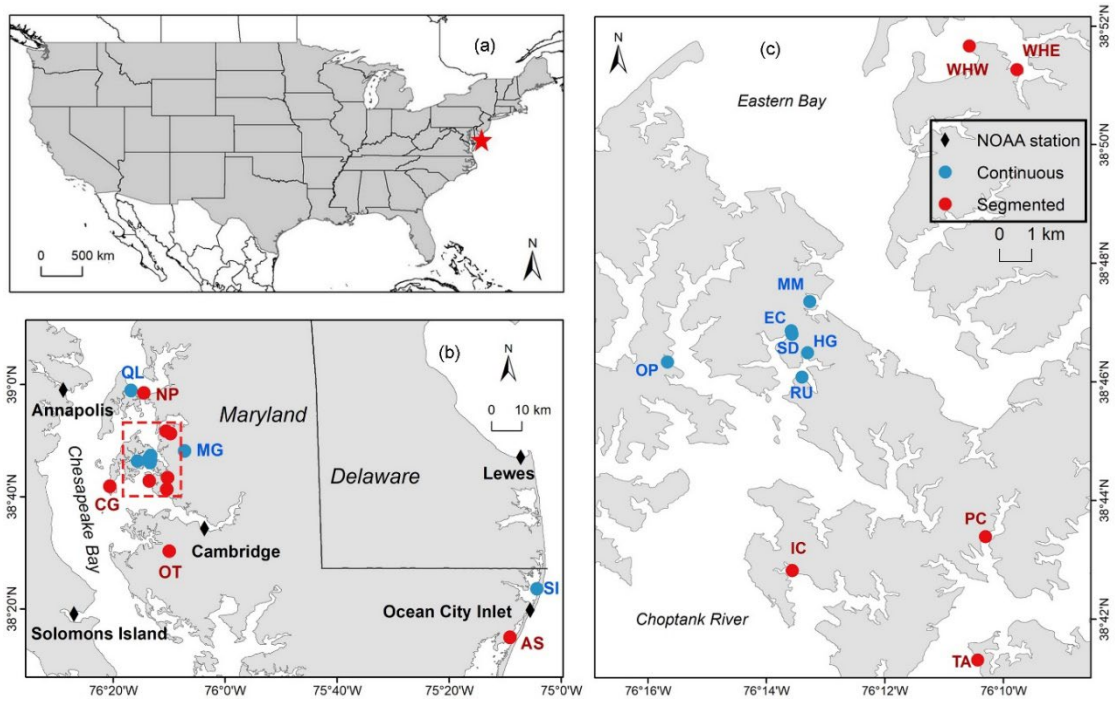


Figure 4.1. Location of study sites. Black diamonds denote the adjacent NOAA stations. Blue dots indicate the continuous sill living shorelines, and red dots represent the segmented sill living shorelines (see Table 4.1).

### 4.2.2. Metrics

This study is based on a variety of data sources, including field sampling, in-situ observations, laboratory processing, and remote sensing. The datasets encompass information on geomorphic features, sediment characteristics, hydrodynamic conditions, vegetation attributes, and marsh trajectory (Table 4.2).

Table 4.2. Summary of metrics used to assess marsh resilience in living shorelines.

| Category | Metric | Reference or data source |
|---|---|---|
| Geographic features | Functional marsh width ($W^*$, m) | This study |
| | Gap/Rock (G/R) ratio | (Hardaway et al., 1991) |
| Morphologic features | Elevation relative to Mean Sea Level (m) | USGS National Map 3DEP (https://www.sciencebase.gov/catalog/item/543e6b86e4b0fd76af69cf4c) |
| | Relative tidal marsh elevation ($Z^*_{MHW}$, m) | (Holmquist and Windham-Myers, 2022) |
| Sediment characteristics | Total Sediment Matter (TSM, mg/l) | (Ondrusek et al., 2012) |
| | Sand percentage (%) | (Palinkas et al., 2023; Sun et al., 2024; Koontz, 2025) |
| | Organic matter content (%) | (Palinkas et al., 2023; Sun et al., 2024; Koontz, 2025) |
| Hydrodynamic conditions | Relative Exposure Index (REI) | (Fonseca et al., 2002; Wong, 2018) |
| | Average tidal range (m) | Center for Operational Oceanographic Products and Services (CO-OPS) tide station (https://tidesandcurrents.noaa.gov/) |

| | | |
|---|---|---|
| | Rate of relative Sea-level Rise (RSLR, mm/y) | National Oceanic and Atmospheric Administration (NOAA) tide gauge (https://tidesandcurrents.noaa.gov/sltrends/sltrends.html) |
| Vegetation characteristics | Vegetation coverage (%) | (Palinkas et al., 2023; Koontz, 2025) |
| | Stem height (cm) | (Palinkas et al., 2023; Sun et al., 2024; Koontz, 2025) |
| | Stem density (num/m^2) | (Palinkas et al., 2023; Sun et al., 2024; Koontz, 2025) |
| Marsh stability | Unvegetated/vegetated ratio (UVVR) | (Ganju et al., 2017) |
| | Deposition rate (mm/y) | (Palinkas et al., 2023; Sun et al., 2024; Koontz, 2025) |

**Geographic features**

Marsh sill living shorelines are typically characterized by a narrow fringing marsh strip featuring a gradual incline situated behind rock sills, which can be either continuous or segmented in design. At the landward boundary of the marsh, a scarp with higher elevation commonly separates the marsh from the residential area. The seaward boundary with rock sills faces the waves and protects the shorelines from erosion. Recently, degradation of marsh resilience has been observed in some marsh sill living shorelines, with boundaries degraded through open-water conversion as

ponds expand landward of the rock sills in both continuous sill (Sun et al., 2024) and segmented sill living shorelines, suggesting a decline in the stability of marsh sill living shorelines. To assess the impacts of open-water conversion on the trajectory of fringing marshes at living shorelines, we introduce an original metric, Functional Marsh Width ($W^*$, m), to integrate the geographic features of the fringing marshes. The $W^*$ metric is calculated as,

$$W^* = \frac{A_v}{L_s}$$

Where $A_v$ is the vegetated marsh area, and the $L_s$ is the total length of the shorelines. Figure 4.2 illustrates the delineation of vegetated and unvegetated areas at living shorelines with various configurations.

Hardaway et al. (1991) initially defined the Gap/Rock (G/R) ratio for headland breakwaters as the ratio of the gap between breakwater units ($G_b$) to the breakwater length ($L_b$). Similarly, we extend this concept to general marsh sill living shorelines. Here, we define the G/R as the ratio of the total length of the gaps between sill segments to the total length of the sill segments. Figure 4.2c-f illustrates sill segments and the gaps between them in marsh sill living shorelines with different designs.

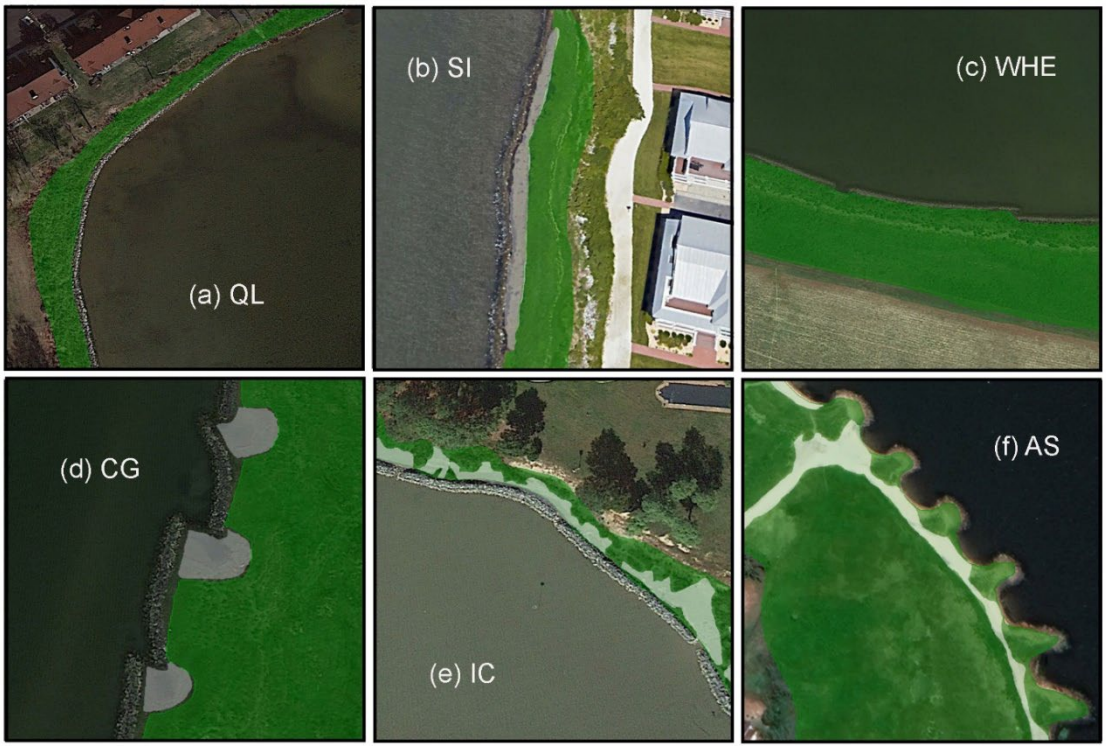


Figure 4.2. Delineation of vegetated and unvegetated areas at living shorelines with various configurations: (a) Continuous sill living shoreline without ponding at QL, (b) Continuous sill living shoreline with ponding at SI, (c) Segmented sill living shoreline without ponding at WHE, (d) Segmented sill living shoreline with ponding at CG, (e) Segmented sill living shoreline with fragmenting marsh at IC, (f) Segmented sill living shoreline with dune at AS. The green zone represents the unvegetated area, and the white zone indicates the vegetated area. Base satellite images are sourced from Google Earth Pro.

**Morphologic features**

Elevation relative to Mean Sea Level (m) referenced to NAVD88 was derived from 1-meter Digital Elevation Models (DEMs) sourced from the USGS National Map 3DEP (U.S. Geological Survey, 2023;

https://www.sciencebase.gov/catalog/item/543e6b86e4b0fd76af69cf4c), and converted to local mean sea level using NOAA's VDatum software (http://vdatum.noaa.gov/docs/userguide.html). The use of the 3DEP Lidar Base Specification provides standardized and consistent data across collections (Stoker and Miller, 2022), and NOAA's VDatum software has been widely employed in previous geomorphic studies (Ganju et al., 2017; Liu et al., 2021).

Relative tidal marsh elevation ($Z^*_{MHW}$, m) is a metric that normalizes elevation to tidal amplitude at mean high water (MHW), it is defined as (Holmquist and Windham-Myers, 2022),

$$Z^*_{MHW} = \frac{Z - MSL}{MHW - MSL}$$

Where Z is the orthometric elevation referenced to the North American Vertical Datum of 1988 (NAVD88). MSL refers to the mean sea level, and MHW is the mean high water.

$Z^*_{MHW}$ is utilized to differentiate wetlands that flood twice a day from those that flood between once a day and a few times a month, accounting for mixed and semi-diurnal tides. This metric provides a convenient and physically relevant means to distinguish between high-elevation and low-elevation marshes. The $Z^*_{MHW}$ data used for this study was extracted from a national-scale map with a resolution of 30 × 30 m covering the contiguous USA (Holmquist and Windham-Myers, 2022).

**Sediment characteristics**

Sediment supply is crucial for surface elevation gains in marsh sill living shorelines. To represent local sediment availability to these shorelines, we included the Total Suspended Matter (TSM, mg/l) as a critical metric. TSM in the nearshore coastal water was derived from remotely sensed Moderate Resolution Imaging Spectroradiometer (MODIS) imagery for the Chesapeake Bay and Choptank River (source: NOAA CoastWatch). Satellite-derived TSM measures the concentration of particulate material in surface water, including mud, silt, and other fine-scale debris, encompassing both organic and inorganic fractions (Ondrusek et al., 2012). The algorithm links in-water sediment concentration measurements to the amount of light leaving the water that is eventually detected by the satellite (Ondrusek et al., 2012). The MODIS-generated TSM product offers high resolution at 250 × 250 m spatial resolution, which is useful for monitoring sediment distribution patterns in the Chesapeake Bay and its tributaries like the Choptank River. In this study, monthly TSM was extracted using Python, averaging the pixel values within 1 km buffers of the study sites. The TSM was then calculated by averaging the TSM values over the 8 months (corresponding to the detection limit for $^{7}$Be) prior to each site's field sampling date (refer to Table 4.1). Specifically, for SI and AS sites, where data encompassed four field sampling periods during 2021-2022, the average value of 24 months' TSM data extracted from monthly imagery was utilized. Sand percentage (%) and organic matter content (%) were derived from field sampling and subsequent laboratory processing, as detailed in the preceding section.

**Hydrodynamic conditions**

The Relative Exposure Index (REI) has been extensively applied in previous research to assess wave exposure intensity in coastal zones (Keddy, 1982; Fonseca et al., 2002; Wong, 2018; Palinkas et al., 2023). It is defined as

$$REI = \sum_{i=1}^{8} (V_i \times T_i \times F_i)$$

where $i$ represents compass headings in 45° increments (e.g., centered on north, northeast, and east). $V_i$ is the average annual wind speed (m/s), $T_i$ is the proportion of time that the wind blew from the $i$-th direction, and $F_i$ is the effective fetch (m) for the i-th direction.

Wind speed data were collected from nearby wind gauges. Specifically, hourly wind directions from Ocean City Inlet, MD (NOAA; ID 8570283) were used for SI and AS. Hourly wind directions from Easton, MD (ID 72404399999) obtained from the National Centers for Environmental Information (NCEI) were used for continuous sill living shorelines at OP, RU, HG, SD, EC, MG, and MM, as well as segmented sill living shorelines at CG, WHE, WHW, PC, IC, and TA. Hourly wind directions from Bay Bridge Airport, MD (ID 72038400124) were obtained for QL and NP. Hourly wind directions from Cambridge, MD (NOAA; ID 8571892) were used for OT.

To calculate effective fetch, the distance from the sampling site to the shoreline along a specified compass bearing (Shore Protection Manual, 1975) was measured for four 11.25° increments centered on the $i$-th compass heading. The effective fetch for each compass heading $i$ was then calculated as,

$$F_i = \frac{\sum_{j=1}^{9} X_j \times \cos \alpha_j}{\sum_{j=1}^{9} \cos \alpha_j}$$

Here, $j$ represents the 11.25° increments on either side of and including the compass heading $i$, $X_j$ is the fetch, and $\alpha_j$ is the angle of departure of the $j$-th increment from the compass heading $i$ (Shore Protection Manual, 1975).

The tidal range (m) data was obtained and interpolated from nearby National Oceanic and Atmospheric Administration (NOAA) tide stations (https://tidesandcurrents.noaa.gov/). The Rate of relative Sea-level Rise (RSLR, mm/y) information was acquired from the Sea Level Rise Viewer (https://tidesandcurrents.noaa.gov/sltrends/sltrends.html), and was also interpolated using data from NOAA tidal gauges.

**Vegetation characteristics**

Vegetation data, comprising vegetation coverage (%), stem height (cm), and stem density (num/$m^2$), were collected during field sampling.

**Marsh trajectory**

The Unvegetated/vegetated ratio (UVVR) is a widely used indicator of tidal marsh trajectory, as it reflects the relationship with the marsh sediment budget (Ganju et al., 2017; Wasson et al., 2019; Defne et al., 2019; Ganju et al., 2020). Unvegetated areas encompass ponds, channels, and dunes, while vegetated areas are covered by plants within each marsh complex (Ganju et al., 2017). A stable tidal marsh, with intact

marsh plains and minimal deterioration, tends to have a UVVR of around 0.1, and values greater than this indicate a trajectory toward marsh plain deterioration (Ganju et al., 2020). Previous research on UVVR for tidal marshes at landscape scales used wetland map code delineation (Defne et al., 2019) or remote sensing imagery, such as the National Agriculture Imagery Program (NAIP; Ganju et al., 2017; Wasson et al., 2019; Ganju et al., 2020) and Landsat (Ganju et al., 2022). Given that marsh sill living shorelines in this study are at a local scale with a maximum length of 570 m, very high-resolution images are required to accurately extract marsh boundaries and existing ponding areas. Therefore, this study uses historical images from Google Earth Pro to delineate vegetated and unvegetated boundaries through manual visualization and digitization (Figure 4.2). Deposition rates (mm/y) were determined using naturally occurring radioisotopes of $^{7}$Be.

### 4.2.3. Field and Lab Methods

Field surveys and sampling were conducted from 2017 to 2023, including vegetation assessments and sediment core collections. Our methodologies for field and laboratory procedures are described in previous studies (Sun et al., 2024; Palinkas et al. 2023; Koontz et al. 2025). Each site featured three to five transects laid perpendicularly across the intertidal marshes of the living shorelines. Sediment cores were collected, and vegetation parameters were recorded, along each transect at 3 to 5 points. Data were averaged to provide site-level characterizations.

Briefly, push cores were returned intact to the laboratory and sectioned into 1-cm increments. The top 1-2 cm of each core was analyzed for sand percentage (%),

median sediment diameter, organic matter content (%), and $^{7}$Be-derived sediment deposition rates (mm/y) as described in Palinkas et al. (2023). Vegetation cover (%), stem height, and stem density were recorded by Palinkas et al. (2023) and Sun et al. (2024).

#### 4.2.4. Statistical Analyses

We employed an independent-sample T-test to examine the significance of sample differences. Pearson correlation analyses were used to quantify the correlation relationship between two datasets. For metrics that were not normally distributed, such as G/R ratio, Elevation relative to MSL, REI, RSLR, vegetation coverage, stem density, and UVVR, we used the Spearman coefficient. We conducted the Shapiro-Wilk Test for normality testing. All statistical analyses were performed using R.

To assess whether the 18 marsh sill living shorelines grouped by ponding versus no ponding based on the assessed metrics, we conducted a suite of related Non-metric Multidimensional Scaling (NMDS) analyses. Ponding was defined by the relative location of open water to rock sills: if open water was on the marsh side of the delineating line at the end of rock sills, it was classified as a living shoreline with ponding; otherwise, it was categorized as a living shoreline with no ponding. NMDS is a statistical technique used to visualize similarities and dissimilarities of data points, focusing on preserving the order of distances or dissimilarities between points instead of exact distances, which is advantageous for ecological or biological data where measurements can be inherently noisy or are best interpreted in rank order (Borcard et al., 2018). Although NMDS does not require independence, the

interpretation of results and subsequent analyses may be influenced by variable relationships. Therefore, we selected six representative metrics, one from each category, characterizing eco-geomorphic features and hydrological conditions of the living shoreline. The six metrics included G/R ratio, Elevation relative to MSL, sand percentage, REI, stem density, and sediment deposition rate. The Unvegetated/Vegetated Ratio (UVVR) was excluded from multivariate analyses because it described rather than predicted the ponding process. In the analysis, we specified two dimensions and used Bray-Curtis dissimilarity for distance, a commonly preferred method in ecological studies (Borcard et al., 2018). Differences between ponding and no ponding sites were visualized using a two-dimensional ordination plot highlighting the main contributors. To further analyze differences by ponding and sill type, we created a similarity matrix and conducted an Analysis of Similarity (ANOSIM). We used Similarity Percentages (SIMPER) to examine groupings and identify metrics that best distinguished them as major contributors. SIMPER is a method used in ecological research to determine the contribution of each variable to the dissimilarity between groups, aiding in understanding which variables contribute most to differences observed in multivariate analyses.

## *4.3. Results*

### 4.3.1. Overall Comparisons of Living Shorelines

To investigate the differences in metrics between continuous sill living shorelines and segmented sill living shorelines, as well as differences between ponding living shorelines and no ponding living shorelines, we performed a series of t-tests (Table

4.3). The results revealed varying patterns of intergroup differences among the living shorelines categorized by these two methods.

In the comparison between continuous and segmented sill types, significant differences were observed primarily in their geomorphic features and vegetation characteristics. Elevations relative to mean sea level (MSL) at the segmented sill living shorelines were significantly higher than those at the continuous sill living shorelines ($p < 0.05$). The relative tidal marsh elevation ($Z^*_{MHW}$) showed a similar but slightly less significant pattern between continuous and segmented sill living shorelines ($p < 0.1$). Regarding vegetation characteristics, significant differences were found in vegetation coverage ($p < 0.05$) and stem height ($p < 0.1$) between continuous and segmented sill living shorelines. Both vegetation coverage and stem height were higher in the continuous sill living shorelines compared to the segmented sill living shorelines. Although stem density was denser in the continuous sill living shorelines compared to the segmented sill living shorelines, this difference was not statistically significant ($p = 0.3$). Importantly, no significant difference was observed in marsh trajectory between continuous sill and segmented sill living shorelines.

Differences in metrics between marsh sill living shorelines grouped by ponding types revealed distinct results (Table 4.3). Living shorelines with ponding tended to exhibit a higher G/R ratio compared to those with no ponding ($p < 0.1$). Although no significant difference was found in elevations between living shorelines with ponding and those with no ponding, there was a significant difference in the average tidal

range between the two groups. Sites with ponding had a relatively higher tidal range than those without ponding ($p < 0.1$). The Relative Exposure Index (REI) at sites with ponding (1011.05 ± 586.16) appeared higher than at sites with no ponding (194.81 ± 26.32), but this difference was not statistically significant. Furthermore, the stem height in the living shorelines with ponding was lower than those with no ponding. In contrast to the comparison between continuous and segmented sill living shorelines, significant differences were observed in marsh trajectory between living shorelines with ponding and those with no ponding. Specifically, the Unvegetated/Vegetated Ratio (UVVR) of the living shorelines with ponding (0.14 ± 0.06) was notably higher than those with no ponding (0, $p < 0.05$), while the sediment deposition rate at sites with ponding (7.14 ± 1.50 mm/y) was relatively lower than those with no ponding (11.59 ± 2.49 mm/y; $p < 0.1$).

Table 4.3. Differences in metrics between varying types of marsh sill living shorelines.

| Metric | Sill type | | | Ponding type | | |
|---|---|---|---|---|---|---|
| | Continuous sill | Segmented sill | p-value | No ponding | Ponding | p-value |
| Functional marsh width (m) | 8.00 ±0.63 | 9.18 ±1.57 | 0.50 | 8.07 ±0.60 | 9.24 ±1.76 | 0.50 |
| Gap/Rock ratio | 0 | 0.15 ±0.07 | **0.05*** | 0.01 ±0.01 | 0.15 ±0.08 | **0.10.** |
| Elevation relative to Mean Sea Level (m) | 0.39 ±0.11 | 0.90 ±0.16 | **0.02*** | 0.51 ±0.16 | 0.81 ±0.13 | 0.20 |
| Relative tidal marsh elevation ($Z^*_{MHW}$, m) | 2.14 ±1.39 | 4.83 ±1.15 | **0.10.** | 3.38 ±1.39 | 3.61 ±1.13 | 0.90 |
| Total Sediment Matter (TSM, mg/l) | 5.19 ±0.20 | 5.13 ±0.23 | 0.90 | 5.07 ±0.21 | 5.22 ±0.19 | 0.60 |
| Sand percentage (%) | 64.78 ±7.78 | 67.66 ±5.60 | 0.80 | 62.48 ±6.27 | 70.89 ±7.08 | 0.40 |

| | | | | | | |
|---|---|---|---|---|---|---|
| Organic matter content (%) | 13.14 ±3.03 | 12.21 ±2.22 | 0.80 | 14.21 ±2.42 | 10.75 ±2.80 | 0.40 |
| Relative Exposure Index (REI) | 202.35 ±27.94 | 912.82 ±526.21 | 0.20 | 194.81 ±26.32 | 1011.05 ±586.16 | 0.20 |
| Average tidal range (m) | 1.54 ±0.08 | 1.59 ±0.08 | 0.70 | 1.48 ±0.02 | 1.67 ±0.12 | **0.10.** |
| Rate of Sea-level Rise (mm/y) | 4.70 ±0.08 | 4.66 ±0.08 | 0.70 | 4.69 ±0.07 | 4.67 ±0.09 | 0.90 |
| Vegetation coverage (%) | 90.50 ±3.23 | 75.02 ±5.67 | **0.05*** | 84.60 ±5.44 | 84.78 ±5.18 | 0.90 |
| Stem height (cm) | 125.64 ±8.58 | 104.00 ±7.18 | **0.07.** | 127.08 ±6.12 | 99.50 ±8.83 | **0.02*** |
| Stem density (num/m^2) | 160.68 ±32.52 | 114.49 ±27.36 | 0.30 | 143.72 ±32.96 | 139.27 ±25.65 | 0.90 |
| Unvegetated/vegetated ratio (UVVR) | 0.02 ±0.02 | 0.11 ±0.05 | 0.20 | 0 | 0.14 ±0.06 | **0.03*** |
| Deposition rate (mm/y) | 10.74 ±2.90 | 9.48 ±1.92 | 0.70 | 11.59 ±2.49 | 7.14 ±1.50 | **0.10.** |

Notes: * $p < 0.05$; **.** $p < 0.10$.

### 4.3.2. Correlation Matrix for the Metrics

The cross-correlation analysis of the metrics (Table 4.4) revealed several significant relationships. The largest correlation was observed between average tidal range and stem height ($r$ = -0.740). Additionally, the average tidal range showed significant correlations with functional marsh width ($W^*$, $r$ = 0.527) and sediment deposition rate ($r$ = -0.382), indicating the influence of tidal conditions on marsh trajectory in living shorelines. Moreover, the sediment deposition rate exhibited inverse correlations with the Unvegetated/Vegetated Ratio (UVVR, $r$ = -0.393), another critical indicator for marsh trajectory. The sediment deposition rate was positively correlated with relative tidal marsh elevation ($Z^*_{MHW}$, $r$ = 0.424) and Total Suspended Matter (TSM, $r$ = 0.579). Notably, the UVVR was positively correlated with the Gap/Rock ratio ($r$ = 0.569) and negatively correlated with stem height ($r$ = -0.583). However, no significant correlation was found between UVVR and any relative elevation metrics (elevation relative to MSL or $Z^*_{MHW}$), suggesting that ponding processes in marsh sill living shorelines may differ from those in natural marshes. The remaining variables generally showed no significant correlation with marsh trajectory based on these analyses. These findings provide insights into the key factors influencing marsh resilience and trajectory in marsh sill living shorelines.

Table 4.4. Correlation coefficients. Red indicates significantly positive correlations. Blue shows significantly negative correlations.

| | Var1 | Var2 | Var3 | Var4 | Var5 | Var6 | Var7 | Var8 | Var9 | Var10 | Var11 | Var12 | Var13 | Var14 | Var15 |
|---|---|---|---|---|---|---|---|---|---|---|---|---|---|---|---|
| *W** (Var1) | 1 | | | | | | | | | | | | | | |
| Gap/Rock ratio (Var2) | 0.294 | 1 | | | | | | | | | | | | | |
| Elevation to MSL (Var3) | 0.271 | **0.610** | 1 | | | | | | | | | | | | |
| $Z^*_{MHW}$ (Var4) | -0.210 | 0.303 | **0.416** | 1 | | | | | | | | | | | |
| TSM (Var5) | -0.168 | 0.118 | 0.379 | 0.254 | 1 | | | | | | | | | | |
| Sand percentage (Var6) | **0.464** | 0.264 | 0.352 | 0.002 | 0.288 | 1 | | | | | | | | | |
| Organic matter content (Var7) | -0.114 | -0.186 | -0.389 | -0.084 | -0.368 | -0.798 | 1 | | | | | | | | |
| REI (Var8) | 0.110 | 0.354 | 0.300 | 0.226 | 0.344 | 0.311 | **-0.655** | 1 | | | | | | | |
| Average tidal range (Var9) | **0.527** | 0.268 | 0.105 | -0.188 | -0.184 | 0.334 | -0.006 | -0.380 | 1 | | | | | | |
| Rate of Sea-level Rise (Var10) | 0.055 | -0.092 | -0.215 | -0.293 | -0.075 | 0.304 | -0.299 | -0.073 | 0.055 | 1 | | | | | |
| Vegetation coverage (Var11) | 0.203 | **-0.435** | -0.385 | -0.074 | -0.188 | -0.032 | -0.109 | 0.241 | -0.218 | -0.319 | 1 | | | | |
| Stem height (Var12) | **-0.554** | **-0.614** | -0.375 | 0.109 | 0.163 | **-0.422** | 0.309 | -0.327 | **-0.740** | -0.278 | 0.068 | 1 | | | |
| Stem density (Var13) | 0.120 | -0.109 | -0.037 | -0.145 | 0.181 | 0.167 | 0.064 | 0.010 | -0.222 | **-0.405** | 0.407 | 0.152 | 1 | | |
| UVVR (Var14) | 0.061 | **0.569** | 0.274 | -0.029 | 0.048 | 0.230 | -0.247 | 0.349 | 0.396 | 0.018 | -0.237 | **-0.583** | -0.055 | 1 | |
| Deposition rate (Var15) | -0.191 | 0.008 | 0.307 | **0.424** | **0.579** | -0.041 | -0.005 | 0.040 | **-0.382** | -0.221 | -0.191 | 0.321 | 0.314 | **-0.393** | 1 |

### 4.3.3. Metrics Related to Marsh Trajectory of Living Shorelines

In exploring the influence of physical and ecological factors on marsh trajectory in marsh sill living shorelines, we investigated the relationships between critical metrics and sediment deposition rate (Figure 4.3). The results revealed several notable correlations. Firstly, a weak positive correlation was observed between elevation relative to mean sea level (MSL) and sediment deposition rate (Figure 4.3a). Secondly, a strong polynomial correlation was found between relative tidal marsh elevation ($Z^*_{MHW}$) and sediment deposition rate ($R^2 = 0.75$; Figure 4.3b), likely linked to the significant correlation observed between average tidal range and deposition rate (Table 4.4). Additionally, a significant positive correlation ($R^2 = 0.33$) was found between Total Sediment Matter (TSM) and sediment deposition rate, indicating higher sediment deposition in marshes located in living shorelines with greater sediment availability in the nearshore coastal water (Figure 3c). Moreover, a negative correlation ($R^2 = 0.19$; Figure 4.3d) was observed between the Unvegetated/Vegetated Ratio (UVVR) and sediment deposition rate, both of which are indicators used to assess marsh trajectory. Sites with a UVVR of 0, indicating no ponding, were observed at several locations. Specifically, QL exhibited a particularly high sediment deposition rate, appearing as an outlier in this correlation (Figure 3d). After removing QL from the analysis, the correlation between UVVR and deposition rate improved (Figure S4.1a; $y = -18.52x + 9.63$, $R^2 = 0.28$). Further filtering out data points with a UVVR of 0 enhanced the correlation even more (Figure S4.1b; $y = -19.57x + 9.94$; $R^2 = 0.52$), highlighting the role of ponding in influencing sediment deposition and marsh trajectory in these living shorelines. These findings provide

valuable insights into the complex relationships between physical and ecological factors impacting marsh resilience and trajectory in marsh sill living shorelines.

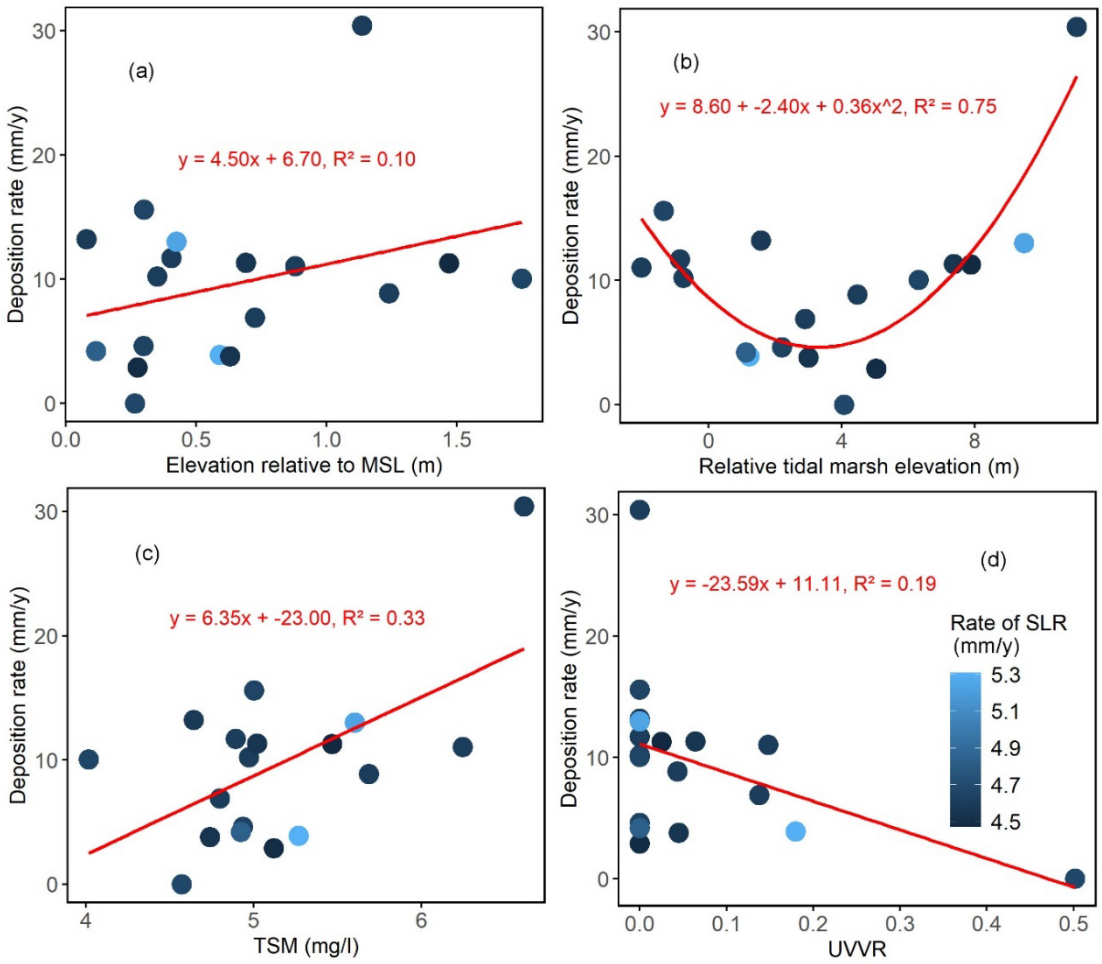


Figure 4.3. Sediment deposition rate (mm/y) in relation to (a) Elevation relative to Mean Sea Level (MSL, m), (b) Relative Tidal Marsh Elevation ($Z^*_{MHW}$, m), (c) Total Suspended Matter (TSM, mg/L), and (d) Unvegetated/Vegetated Ratio (UVVR). Different colors correspond to different rates of sea level rise (mm/y).

Although no linear correlation was identified between the functional marsh width ($W^*$) and deposition rate, we found nonlinear relationships between $W^*$ and the

difference between the observed sediment deposition rate and the rate of relative sea-level rise (Figure 4.4). The results depicted varying patterns in the scaling of sediment deposition rate with $W^*$ under different circumstances. When the deposition rate exceeded the rate of sea level rise, a negative scaling relationship was observed (Figure 4.4b), indicating that as the functional marsh width increased, the deposition rate also increased ($y = 189.46x^{-1.542}$, $R^2 = 0.886$). Conversely, when the deposition rate was below the rate of sea level rise, a positive scaling relationship was evident (Figure 4.4c), signifying that the deposition rate increased with increasing functional marsh width ($y = 3.473\ln(x) - 8.275$, $R^2 = 0.970$). In general, a width of 5-10 m would represent a good balance between cost-effectiveness and achieving a relatively high deposition rate under both circumstances described. This functional marsh width optimizes sediment deposition rates, showing favorable outcomes regardless of whether the deposition rate exceeds or underperforms the rate of sea level rise.

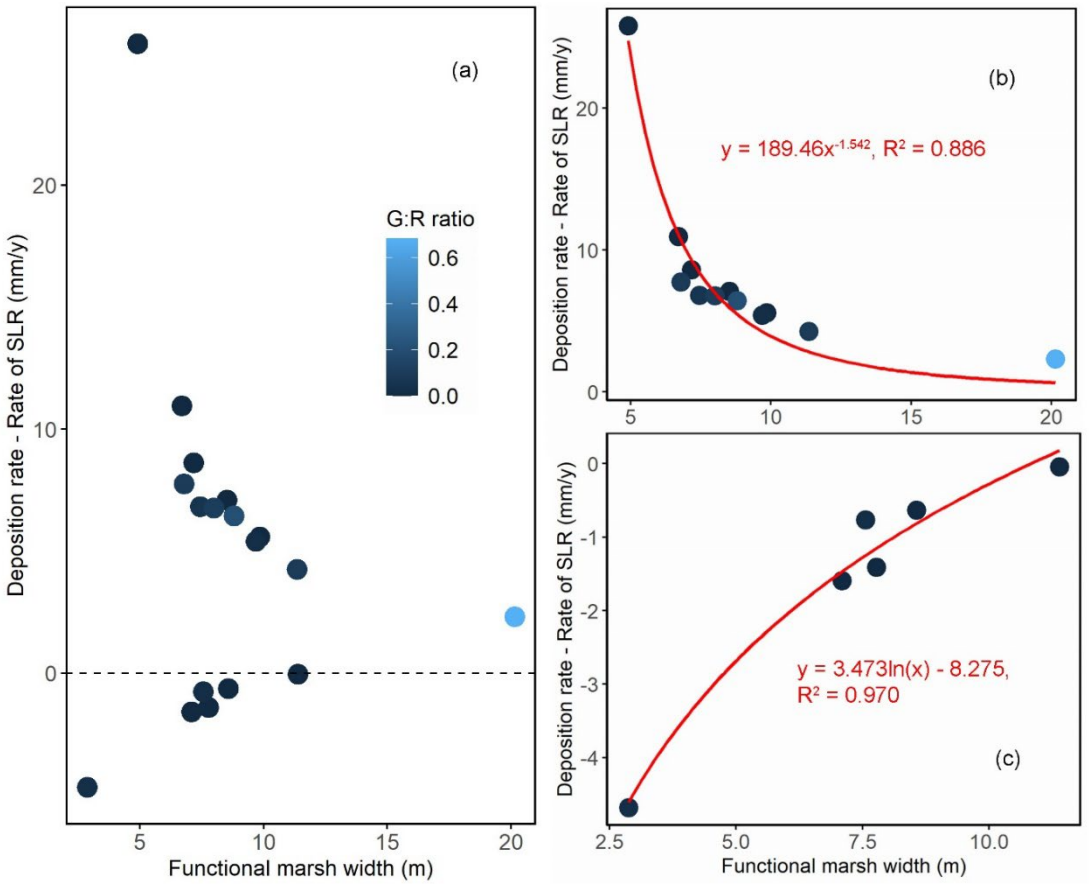


Figure 4.4. Relationship between functional marsh width (*W**, m) and the difference between the sediment deposition rate and the Rate of relative Sea-Level Rise (RSLR; mm/y). (a) Scatter plot illustrating the relationship between *W** and the difference between the sediment deposition rate and RSLR. (b) Relationship between *W** and the difference between the sediment deposition rate and RSLR when the sediment deposition rate exceeds the RSLR. (c) Relationship between *W** and the difference between the sediment deposition rate and RSLR when the sediment deposition rate is below the RSLR. Different colors represent varying Gap/Rock ratios.

### 4.3.4. Factors Potentially Related to Ponding Processes in Living Shorelines

We selected six representative metrics from each category for non-metric multidimensional scaling (NMDS) analysis across 18 living shorelines to explore the environmental factors potentially related to the ponding processes in marsh sill living shorelines. These metrics included Gap/Rock ratio, elevation relative to mean sea level (m), sand percentage (%), Relative Exposure Index (REI), stem density (num/$m^2$), and deposition rate (mm/y). The selected metrics were mostly independent except that a significant correlation was found between the G/R ratio and Elevation relative to MSL. The NMDS analysis yielded a robust ordination of sites, visually indicating clear separation among living shorelines with ponding versus no ponding (Figure 4.5). An ANOSIM test confirmed that the ponding group was significantly influenced by environmental factors ($p < 0.05$), with the six metrics explaining 17.10% of the observed variability between the ponding versus no ponding group. However, a similar ANOSIM test based on sill types (continuous sill versus segmented sill living shorelines) revealed a relatively low proportion of variance explained ($R^2 = 0.10$) by sill type, and sill type did not significantly account for variability in the NMDS data ($p = 0.12$). Notably, Sunset Island (SI) showed little separation from the living shorelines with no ponding, aligning with field observations that ponding was limited to the north in this living shoreline. Given the correlation between G/R ratio and elevation relative to MSL, we further removed one of the two metrics to keep variables independent. Results indicated that removing either of them in the NMDS analysis led to less separation among living shorelines with ponding versus no ponding (Figure S4.2). Conversely, Irish Creek (IC),

Assateague State Park (AS), and Conrad Gordon (CG) clearly separated from living shorelines with no ponding, reflecting the noticeable presence of open water within these marshes.

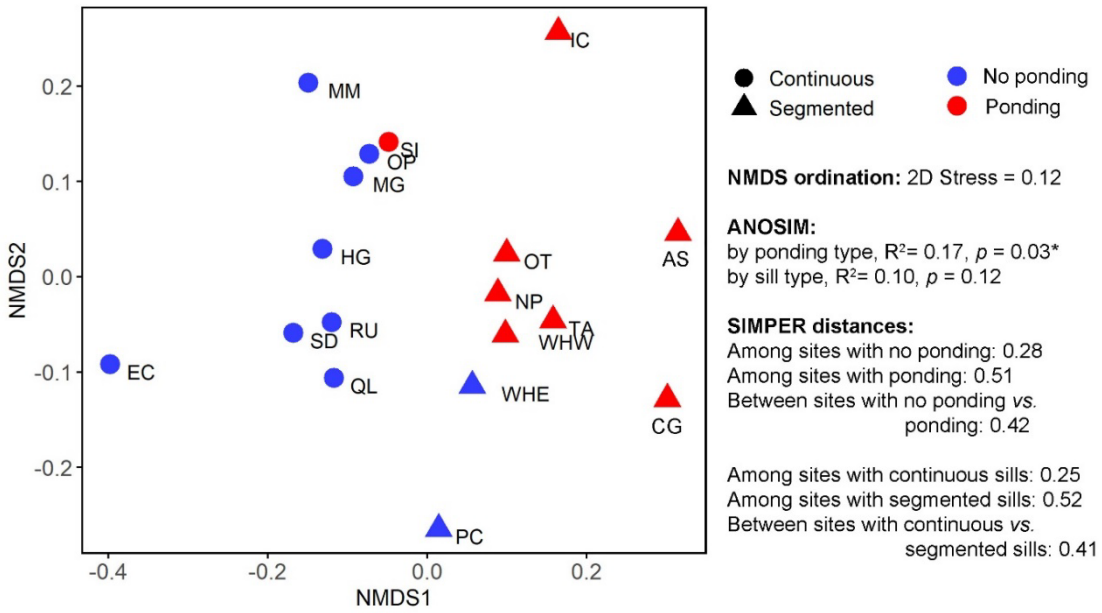


Figure 4.5. Non-metric multi-dimensional scaling analyses for 18 living shorelines with representative variables including Gap/Rock (G/R) ratio, Elevation relative to Mean Sea Level (m), Sand percentage (%), Relative Exposure Index (REI), Stem density (num/m$^2$), and Deposition rate (mm/y). * $p < 0.05$.

The SIMPER analysis revealed significant differences in average squared distances among sites within the ponding versus no ponding groups (0.28 versus 0.51), clearly separating them into two distinct groups on the plot (Figure 4.5). Similarly, within the sill type comparison (continuous sill versus segmented sill), the average squared distance among sites within the continuous sill group (0.25) was significantly less

than within the segmented sill group (0.52), resulting in distinct separation on the plot (Figure 4.5). The SIMPER analysis identified Relative Exposure Index (REI) and Gap/Rock ratio emerging as significant contributors, explaining 5.46% and 4.41% of the difference between ponding and no ponding groups, respectively (Table 4.5). Additionally, elevation relative to Mean Sea Level (MSL) and G/R ratio explained 10.42% and 5.72% of the difference between continuous and segmented sill living shorelines, respectively (Table 4.5).

Table 4.5. Results of SIMPER analyses providing the contribution of each metric to the overall dissimilarity grouped by sill type and ponding type.

| Metric | Sill type | | | Ponding type | | |
|---|---|---|---|---|---|---|
| | Contribution (%) | Ratio | *p*-value | Contribution (%) | Ratio | *p*-value |
| Sand percentage (%) | 11.59 | 1.18 | 0.70 | 11.58 | 1.14 | 0.70 |
| Elevation relative to Mean Sea Level (m) | 10.42 | 1.39 | **0.03*** | 9.89 | 1.55 | 0.12 |
| Deposition rate (mm/y) | 7.25 | 1.01 | 0.73 | 7.43 | 0.97 | 0.46 |
| Stem density (num/$m^2$) | 7.15 | 0.91 | 0.20 | 6.54 | 0.90 | 0.86 |
| Gap/Rock ratio | 5.72 | 0.90 | **0.01*** | 5.46 | 0.82 | **0.01*** |
| Relative Exposure Index (REI) | 4.00 | 0.58 | **0.06.** | 4.41 | 0.61 | **0.01*** |

Notes: * $p < 0.05$; **.** $p < 0.1$.

*4.4. Discussion*

UVVR (Unvegetated/Vegetated Ratio) and sediment deposition rate are recognized indicators of tidal marsh resilience (Ganju et al., 2017; Raposa et al., 2016), but their applicability to assessing the stability of marsh sill living shorelines has not been previously explored. In this study, we investigated 18 marsh sill living shorelines in Maryland, comprising 9 with continuous sills and 9 with segmented sills. Our results indicated no significant difference in UVVR and deposition rate between continuous and segmented sill living shorelines. However, significant differences were observed among living shorelines with ponding versus no ponding. Specifically, living shorelines with ponding at the marsh edge tended to exhibit a significantly higher UVVR (0.14±0.06, $p < 0.05$) and a lower sediment deposition rate (7.14±1.50 mm/y, $p < 0.1$; Table 4.1). Previous research has highlighted that UVVR values greater than 0.1 are indicative of increased open-water conversion and marsh deterioration (Ganju et al., 2017, 2020; Wasson et al., 2019). We identified a significant correlation between UVVR and deposition rate (Figure 4.3d; $R^2 = 0.22$, $p < 0.1$), which was stronger among living shorelines with ponding (Figure S4.1b; $y = -19.57x + 9.94$; $R^2 = 0.52$). These findings align with earlier studies on natural tidal marshes, which emphasized the importance of UVVR and deposition rate as indicators of marsh stability (Ganju et al., 2017; Wasson et al., 2019).

In natural marshes, indicators of marsh stability are often associated with environmental factors that influence marsh dieback, including elevation, sediment supply, and sea-level rise (Wasson et al., 2019). In this study, we investigated

correlations of marsh resilience with physical and ecological factors that could contribute to marsh boundary degradation in living shorelines, revealing patterns reminiscent of natural marshes. For instance, we observed a significant positive correlation between sediment deposition rate and Total Suspended Matter (TSM; $R^2 = 0.33$, $p < 0.01$), indicating that living shorelines can trap more sediments where coastal nearshore water has higher sediment availability. This finding aligns with earlier research emphasizing the significant role of sediment availability in coastal wetland restoration success (Liu et al., 2021). However, not all patterns observed in natural marshes necessarily translate to living shoreline marshes. While previous studies across natural marsh ecosystems have noted a consistent scaling of elevation with UVVR, showing lower elevation units tend to exhibit more open-water conversion and higher UVVRs (Ganju et al., 2021), we found no significant linear correlation between UVVR and elevation relative to Mean Sea Level (MSL). Instead, we identified a significant polynomial relationship between sediment deposition rate and Relative Tidal Marsh Elevation ($Z^*_{MHW}$), underscoring the importance of tidal range in living shoreline marshes (Figure 4.4b). The higher sediment deposition rate in marshes with lower $Z^*_{MHW}$ could be attributed to marsh loss and open-water conversion. A tidal marsh that has already experienced vegetation loss may witness increased sediment mobilization through tidal and wave processes, leading to accretion due to longer submergence times (Morris et al., 2002; Reed, 2002; Wiberg et al., 2019). Therefore, in marshes with significant vegetation loss, sediment accretion, and subsequent elevation gain may be symptoms of instability rather than drivers of stability (Ganju et al., 2015).

Among the key indicators of marsh stability, functional marsh width ($W^*$) is a novel metric that captures the geographic characteristics of fringing marshes. The relationship between $W^*$ and sediment deposition rate varied depending on whether the deposition rate exceeded or fell below the relative sea level rise (RSLR). When the deposition rate exceeded the RSLR, a negative scaling relationship is observed (Figure 4.4b; $y=189.46x^{-1.542}$, $R^2=0.886$). Conversely, when the deposition rate was below the RSLR, a positive scaling relationship was evident (Figure 4.4c; $y=3.473\ln(x)-8.275$, $R^2=0.970$). These varying correlations can be explained by the physical processes of sediment transport and deposition. When the deposition rate exceeded the RSLR, the negative scaling relationship suggested diminishing returns as marsh width increased, likely due to reduced sediment concentration or changes in flow dynamics. Initially, wider marshes enhanced sediment deposition by providing more area for sediment to settle and slowing water flow. However, beyond a certain width, the additional benefits decreased. In contrast, when the deposition rate was below the RSLR, the positive scaling relationship indicated that increasing marsh width consistently improved sediment trapping efficiency, though the rate of improvement diminished logarithmically. An optimal marsh width of approximately 5-10 meters balanced cost-effectiveness with high deposition rates, effectively leveraging the benefits of increased width without encountering diminishing returns or excessive costs.

Open-water conversion is a primary destructive process in marshes, influencing the long-term fate of marsh complexes (Ganju et al., 2017). Previous studies have noted that the living shoreline boundary degrades as ponds expand landward of rock sills (Sun et al., 2024). We identified this form of ponding at 8 sites, encompassing both continuous and segmented sill living shorelines. Through multivariate analyses, we investigated the main drivers of this ponding process in living shorelines. Results indicated that the Gap/Rock ratio and Relative Exposure Index (REI) made significant contributions to differences among living shorelines with ponding versus no ponding, with contributions of 5.46% and 4.41%, respectively ($p < 0.05$ for both). This suggests that tidal gaps and wind-generated wave energy are primary drivers of ponding in living shorelines. Independent t-tests also showed a significant difference in G/R ratio between living shorelines grouped by ponding and no ponding, with a higher G/R ratio in living shorelines with ponding (0.15±0.08) compared to those without ponding (0.01±0.01; $p < 0.1$), indicating more frequent ponding in segmented sill living shorelines than continuous sill living shorelines. Although REI was dramatically higher in living shorelines with ponding (1011.05±586.16) compared to those without ponding (194.81±26.32), this difference was not statistically significant in the t-test ($p = 0.2$). Among living shorelines grouped by sill types, major contributors to differences between continuous sill and segmented sill living shorelines were relative elevation to Mean Sea Level (MSL) and G/R ratio, with contributions of 10.42% and 5.72%, respectively ($p < 0.05$ for both). This suggests that while consideration was given to marsh elevation or height in living shoreline

design, more attention is needed to wave energy to prevent ponding and marsh degradation.

For marsh managers, the most valuable indicators of marsh resilience in living shorelines should possess predictive power for degradation, enabling optimized design or post-construction maintenance interventions. This predictive capability allows for strategies to prevent marsh degradation through specialized design or timely interventions to restore marshes, such as elevation addition, marsh replanting, sill height adjustment, or facilitating marsh migration to higher ground. Robust predictions often stem from factors directly related to marsh dieback drivers (Wasson et al., 2019). Some metrics in our analyses signal potential marsh boundary degradation in marsh sill living shorelines. Designers should particularly consider the G/R ratio of gap design in living shorelines. Although tidal gaps are increasingly used to enhance hydrological connectivity and marine fauna access to created marshes, they can also increase tidal water exchange, wave energy transmission, and sediment transportation, impacting erosion/deposition in the created marsh (Miller et al., 2022). Notably, living shorelines with a high G/R ratio are likely to develop ponding zones between segmented sills, especially at sites with high wave energy. Designers should account for this, possibly incorporating ponding into the design. For instance, the living shoreline at AS was designed as a headland breakwater with a G/R ratio close to 1, incorporating a ponding area and pocket beach between sill segments into the design.

This study provides valuable insights into optimal living shoreline design and maintenance post-construction, but several important limitations must be acknowledged. One significant limitation is the use of static metrics to depict the current state of living shorelines, rather than tracking changes over time, which may limit the understanding of marsh dynamics and response to environmental stressors. Field sampling conducted across different years within the growing season (2017 to 2023) introduces temporal variability that could affect data interpretation and trend analysis. Besides, $^{7}$Be-derived sediment deposition rates are at seasonal scales, while the RSLR is averaged over decades. This discrepancy in the timescale might limit the direct comparability of the two, potentially leading to challenges in accurately correlating sediment dynamics with long-term environmental changes. Additionally, the reliance on Google Earth Pro for satellite imagery-based metrics may introduce uncertainty due to differences in image resolution, data quality, and acquisition methods. Finally, the study's geographical focus on Maryland's Chesapeake Bay and Coastal Bays implies that observed patterns and conclusions may not universally apply to other coastal regions with distinct environmental conditions, morphologies, and anthropogenic influences. Despite these limitations, this study provides valuable insights into metrics for assessing the stability of marsh sill living shorelines and major drivers for the potential marsh boundary degradation. The findings contribute to a deeper understanding of the marsh resilience of living shorelines and offer a solid foundation for advancements in shoreline design and post-construction maintenance.

*4.5. Conclusions*

This study investigated 18 marsh sill living shorelines in Maryland, nine with continuous sills and nine with segmented sills. It assessed the resilience of these marshes under different sediment supply and hydrodynamic conditions to determine if metrics applicable to natural marshes could also predict potential degradation in living shoreline marshes. Utilizing datasets from four prior studies, including 15 metrics obtained through field measurements and remote sensing, we sought to identify common patterns across regional ecosystems. The results suggested that the UVVR and sediment deposition rates effectively differentiated among living shorelines with and without ponding. Moreover, their correlation with other environmental factors like Total Suspended Matter (TSM) and relative tidal marsh elevation ($Z^*_{MHW}$) aligned with patterns observed in natural marshes. Among the six representative metrics selected from each category, the Relative Exposure Index (REI) and G/R ratio were identified as significant contributors to the ponding processes at the marsh boundaries ($p < 0.05$). Additionally, we introduced a novel vegetation-related metric, the Functional Marsh Width ($W^*$), to assess the effective width of fringing marshes in living shorelines. Its nonlinear correlation with sediment deposition rates suggested that a width of approximately 10 m is optimal for achieving more sediment deposition. Overall, this research not only explores the application of various metrics in assessing marsh resilience but also sheds light on potential causes of boundary degradation in living shorelines, offering possible strategies to optimize marsh-sill complex design and post-construction maintenance.

# Chapter 5: Conclusions

This dissertation has investigated shoreline erosion and sediment deposition processes in 18 marsh sill living shorelines in Maryland's Chesapeake Bay and Coastal Bays through field sampling, remote sensing, and numerical modeling. The aim was to explore the mechanisms of marsh resilience and shoreline stability under the placement of rock sills. First, this research identified open-water conversion at the marsh boundary of a mature marsh sill living shoreline (constructed in 2007) and explored the potential causes of marsh boundary degradation by comparing the living shoreline marsh with an adjacent natural marsh. The study further examined the impacts of rock sill placement on sediment dynamics in living shorelines and assessed the function of tidal gaps in enhancing sediment import during high-energy events. Finally, the research integrated a wide range of datasets from all 18 marsh sill living shorelines and evaluated the applicability of metrics used for tidal marsh resilience, such as UVVR and sediment deposition rate in living shoreline marshes.

Chapter 2 focused on the mechanisms of marsh loss at the edge of living shorelines compared to natural marshes under high-energy conditions. It was found that natural marshes eroded primarily through undercutting and edge collapse, while living shorelines experienced open-water conversion behind rock sills. This conversion was strongly correlated with local elevation, where lower elevations led to more open water in the living shoreline marsh. Variations in sediment and vegetation characteristics, such as higher stem height and lower organic content in living shorelines, influenced these erosion patterns. The study highlighted the impact of bed shear stress induced by rock sills, contributing to scouring and open-water

conversion, and suggested that increasing the bank height could reduce erosion at the marsh edge.

In Chapter 3, the study assessed two types of marsh sill living shorelines—continuous and segmented—near Ocean City, Maryland. Over two years, changes in sediment concentration, elevation, and sedimentation rates were monitored. The use of Delft3D-SWAN modeling revealed that rock sills could mitigate edge erosion but might reduce sediment deposition on the marsh platform. Gaps in the sills showed potential for enhancing marsh stability by balancing erosion control with sediment deposition. Future research directions include extensive modeling to validate these findings and refine gap configurations to optimize sediment flux and stability in living shorelines.

Chapter 4 extended the investigation to 18 marsh sill living shorelines with varied geomorphic features and vegetation characteristics. Using metrics from field measurements and remote sensing, the study evaluated resilience under different sediment supply and hydrodynamic conditions. Metrics like UVVR and sediment deposition rates proved effective in differentiating marshes with and without ponding. The introduction of the Functional Marsh Width ($W^*$) provided a new perspective on the optimal width for sediment deposition in fringing marshes. The findings highlighted common patterns across regional ecosystems and identified key metrics, such as the Relative Exposure Index (REI) and G/R ratio, as significant indicators of boundary degradation.

In practice, effective living shoreline design requires thorough site-specific assessments to understand environmental and structural factors such as local elevation, wave exposure, sediment dynamics, and vegetation characteristics. The presence of rock sills can influence marsh resilience and shoreline stability, with low elevations contributing to open-water conversion and gaps in sills enhancing sediment import during high-energy events. Practitioners should evaluate metrics like UVVR and sediment deposition rate to differentiate marsh conditions and guide design decisions. Recommendations include increasing bank height and optimizing gap configurations in rock sills to balance erosion control with sediment deposition. By applying these insights, stakeholders can develop sustainable living shorelines that support long-term ecological health and shoreline protection.

Overall, this work sheds light on potential causes of boundary degradation in marsh sill living shorelines and offers strategies to optimize marsh-sill complex design and maintenance post-construction. By investigating mechanisms of marsh boundary degradation, sediment dynamics, and resilience metrics, this research contributes to the broader understanding of the effectiveness and optimization of living shorelines for coastal protection. It provides critical insights for coastal managers and regulatory agencies to promote practical solutions for shoreline protection. Future research will focus on the long-term performance of living shorelines with different structure types (e.g., oyster reef sills) in the face of sea-level rise and the optimization of tidal gap design under varying hydrodynamic and ecological conditions.

# Appendices

*A.1. Supporting information for Chapter 2*

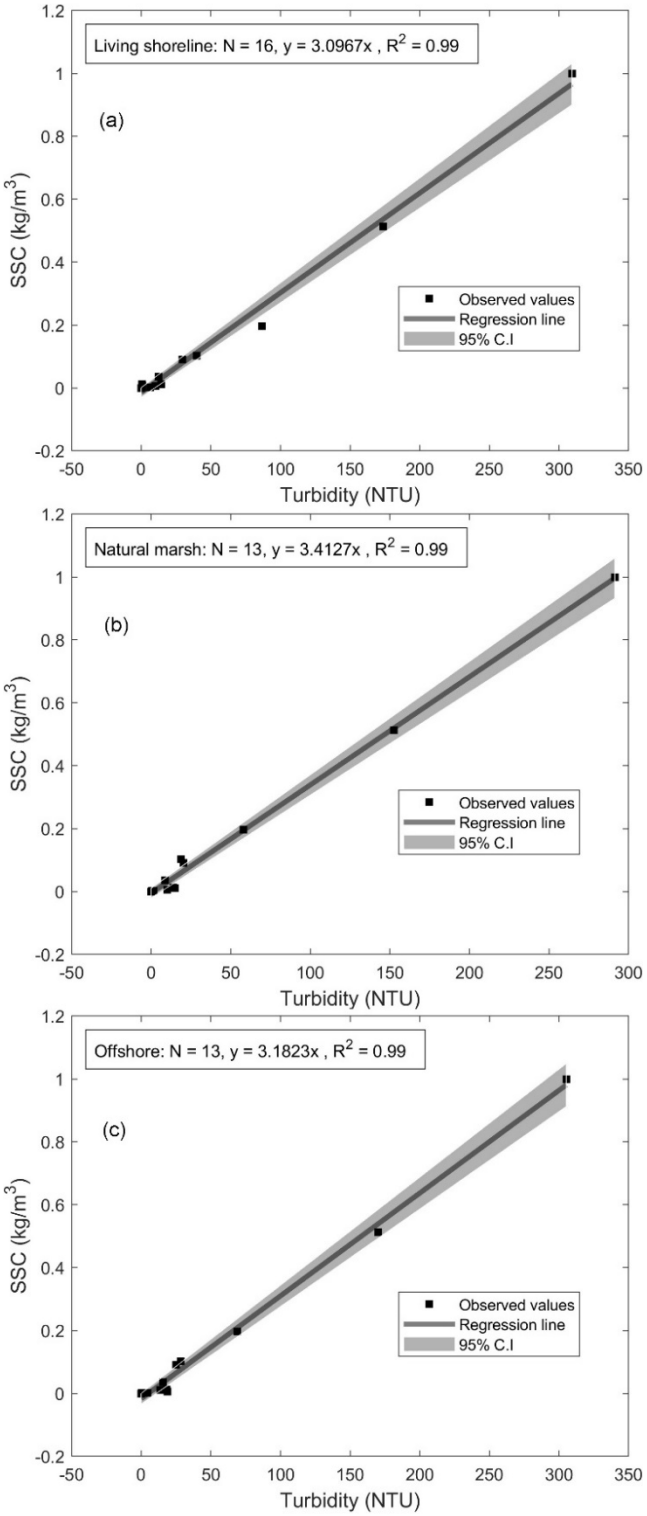


Figure S2.1. Calibration curve used to convert turbidity (NTU) to suspended sediment concentration (mg/L).

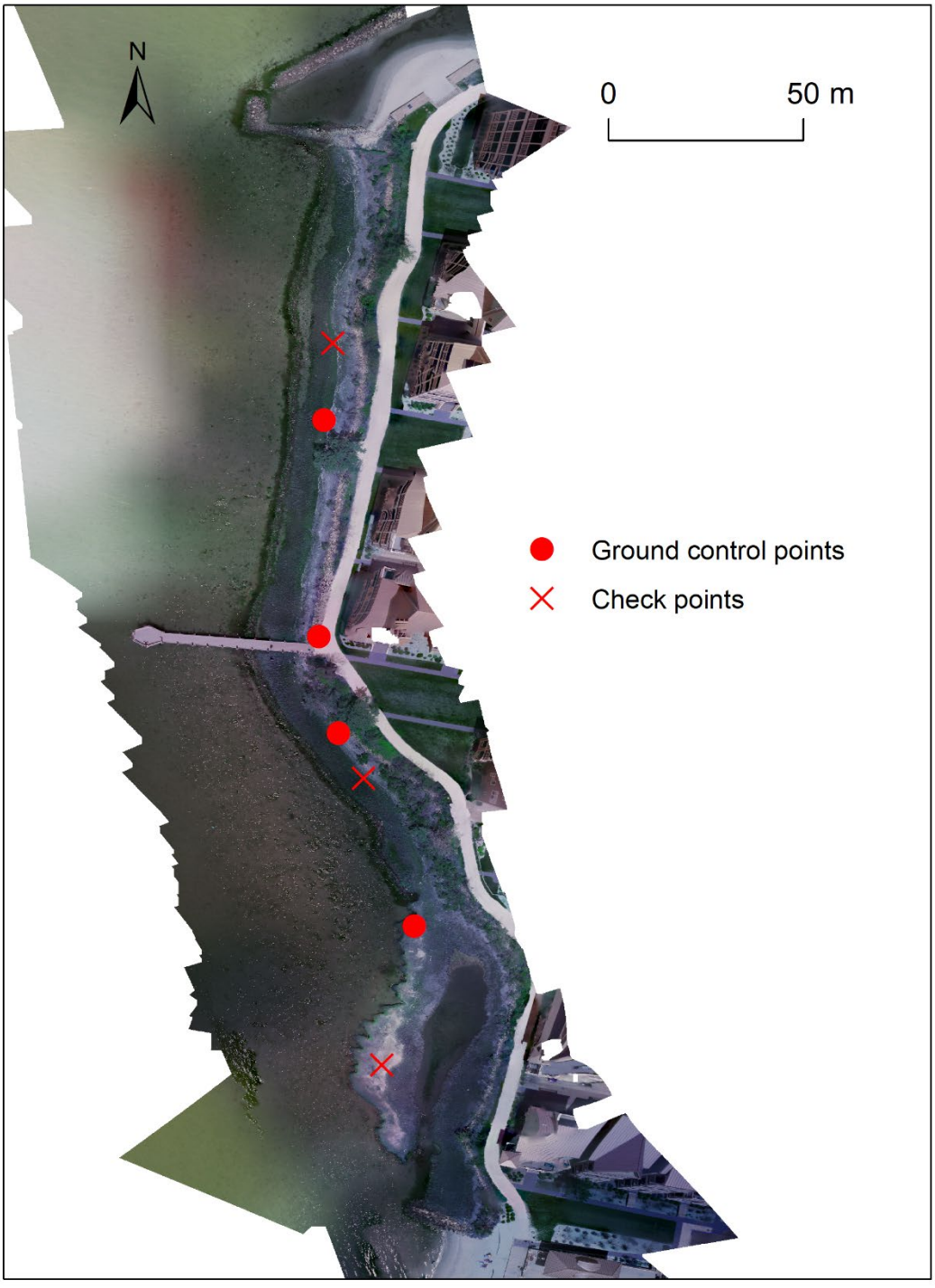


Figure S2.2. Location of Ground Control Points (GCPs) and Check Points (CPs).

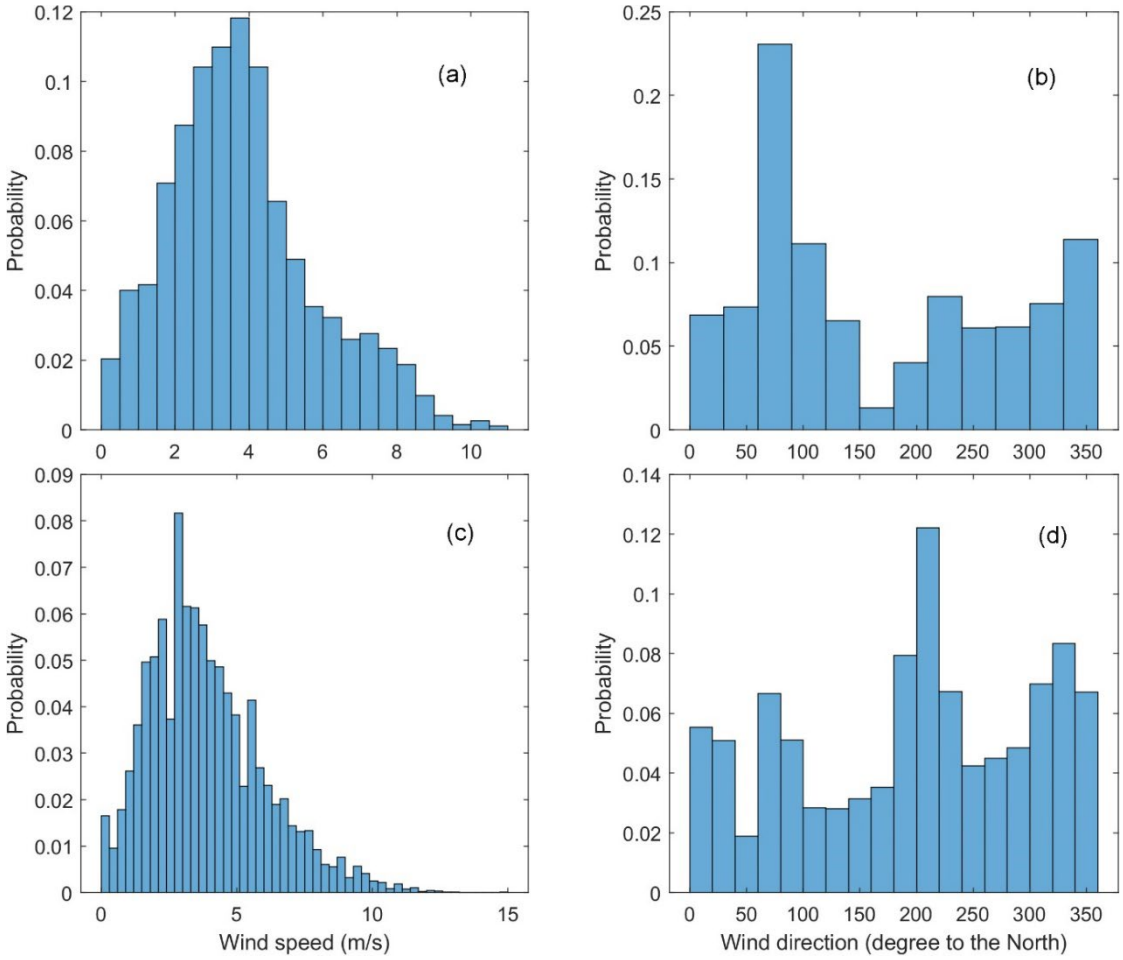


Figure S2.3. Histograms of wind speed (m/s; a is for the 8 days' simulation and c is for 2023) and wind direction (degree to the North; b is for the 8 days' simulation and d is for 2023) from the NOAA station at Ocean City Inlet (https://tidesandcurrents.noaa.gov/stationhome.html?id=8570283).

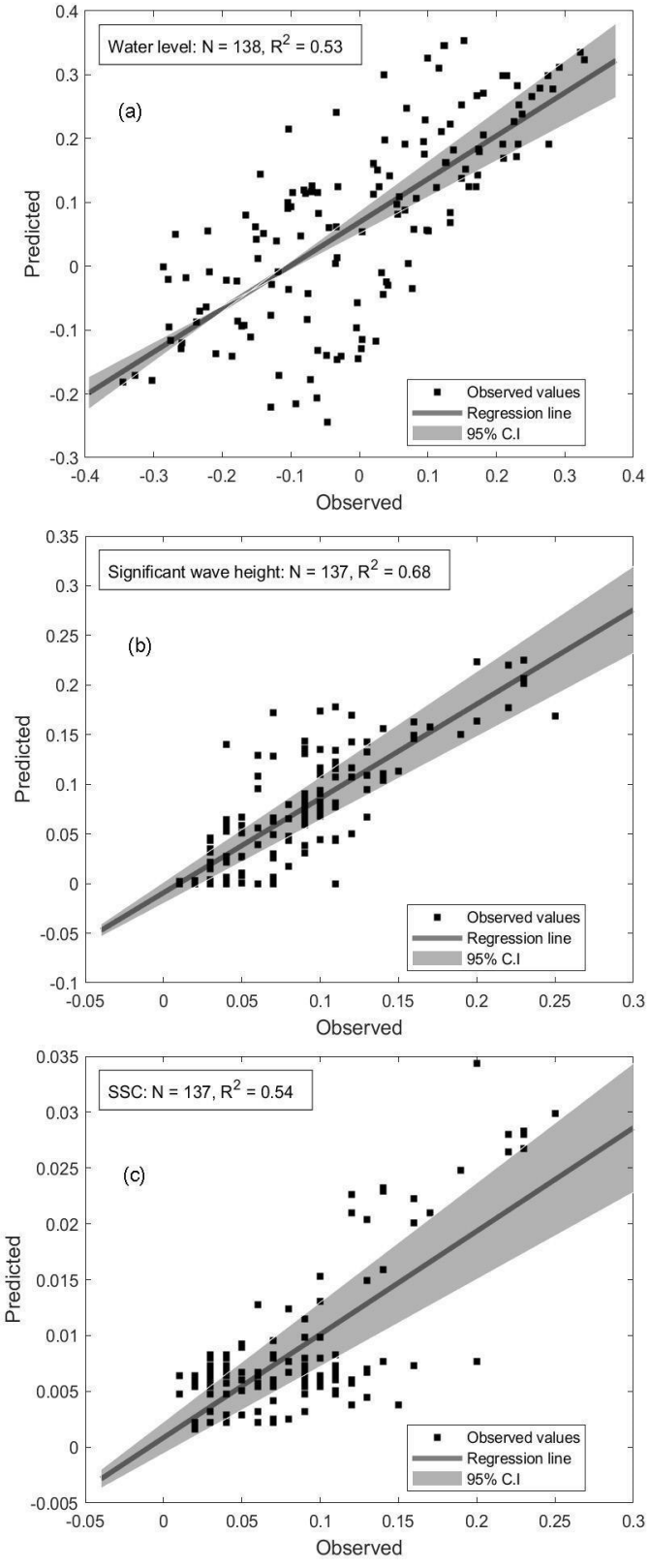


Figure S2.4. Correlation between predicted and observed data.

Table S2.1. Network accuracy estimates per FGDC geospatial positioning accuracy standards.

| | FGDC (95% conf, cm) | | Standard deviation (cm) | | | CorrNE |
|---|---|---|---|---|---|---|
| | Horiz | Ellip | SD_N | SD_E | SD_h | (unitless) |
| NETWORK | 0.48 | 0.90 | 0.21 | 0.18 | 0.46 | -0.0678798 |

Table S2.2. Aircraft and camera specifications.

| **Aircraft Specifications** | |
|---|---|
| Type | DJI Phantom 3 Professional |
| Takeoff weight | 1280 g |
| Max flight speed | 16 m/s |
| Max flight time | ≈12 min |
| Horizontal hovering accuracy | ±0.3 ÷ 1.5 m |
| Vertical hovering accuracy | ±0.1 ÷ 0.5 m |
| **Camera Specifications** | |
| Name | MicaSense RedEdge-M |
| Type | RGB + NIR |
| Focal length | 3.6 mm |
| 35 mm equiv. focal length | 20 mm |
| Image resolution | 1280 × 960 |
| Field of view | 84° |
| GSD at 40 m altitude | ≈1.8 cm |

Table S2.3. Residuals for Ground Control Points (GCPs) and Check Points (CPs).

| | | East (m) | North (m) | Elevation (m) | 3D (m) |
|---|---|---|---|---|---|
| Ground Control Points | Average | 0.641 | 0.599 | 0.025 | 1.537 |
| | Min Difference | -0.442 | -0.167 | -0.122 | 0.266 |
| | Max Difference | 2.74 | 2.538 | 0.107 | 2.761 |
| | RMSE | 1.391 | 1.296 | 0.092 | 1.903 |
| Check Points | Average | -0.855 | -0.799 | -0.098 | 1.746 |
| | Min Difference | -1.926 | -2.808 | -0.055 | 0.538 |
| | Max Difference | 0.419 | 0.748 | -0.016 | 3.406 |
| | RMSE | 1.118 | 1.463 | 0.032 | 1.842 |

*A.2. Supporting information for Chapter 3*

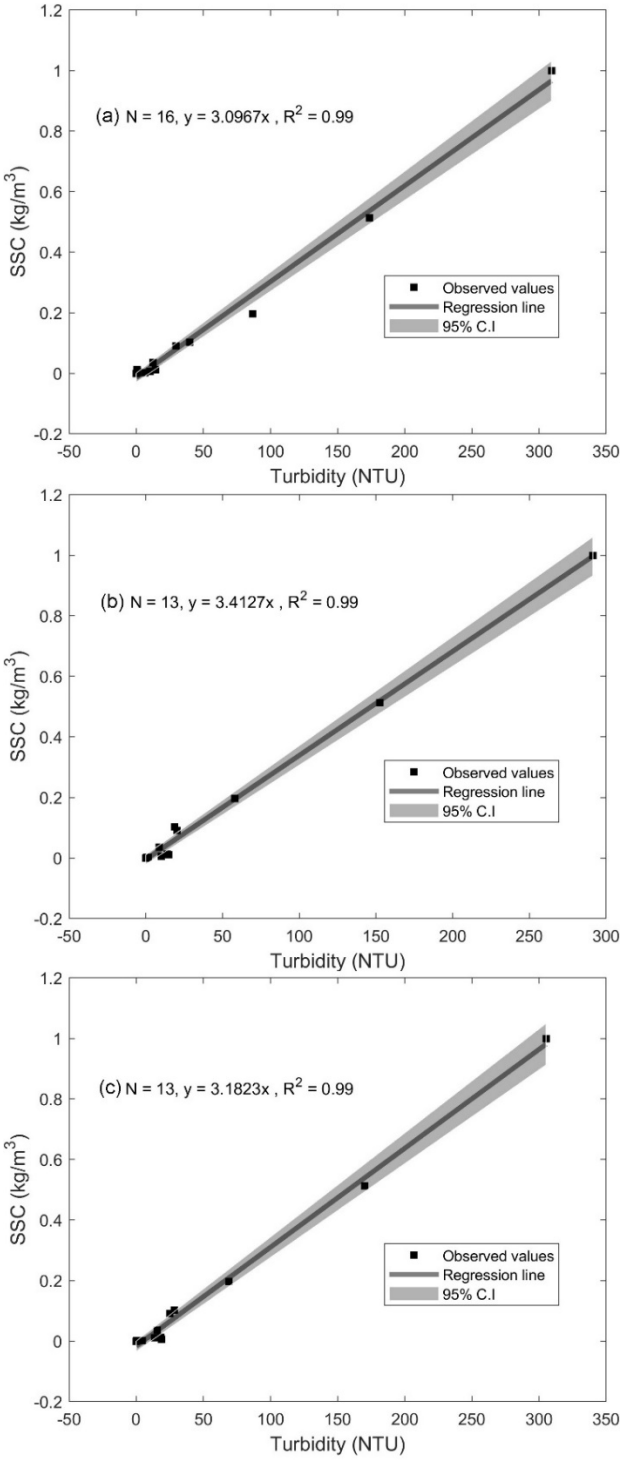


Figure S3.1. Calibration curve used to convert turbidity (NTU) to suspended sediment concentration (mg/L).

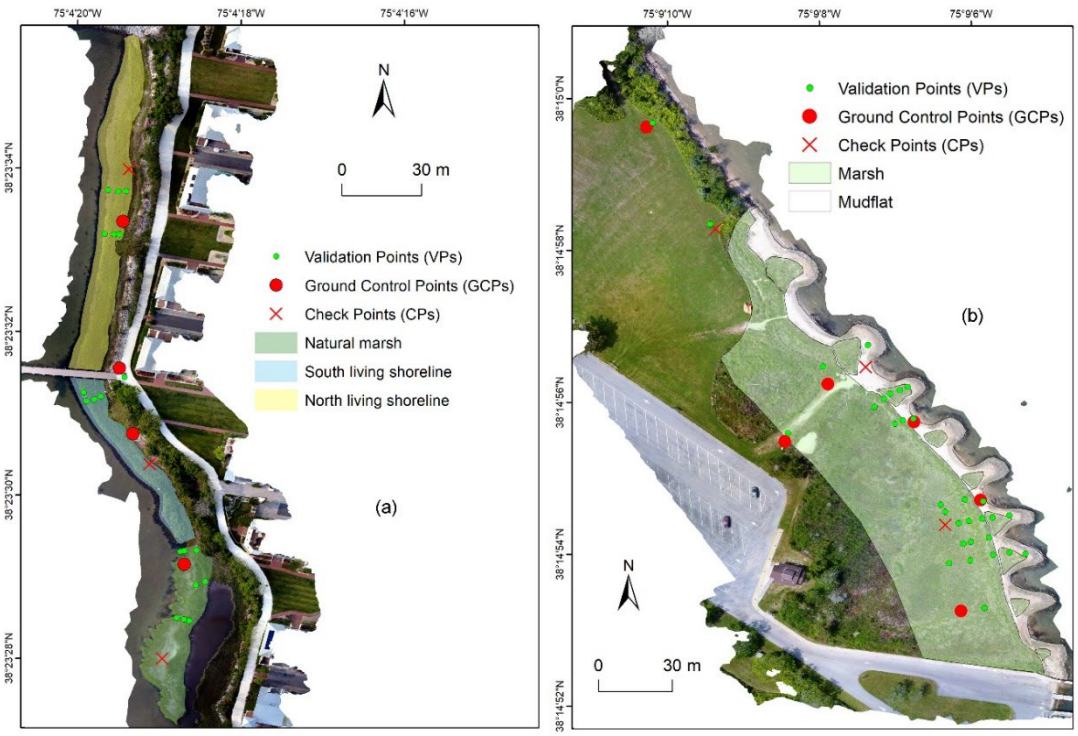


Figure S3.2. Locations of Validation Points (VPs), Ground Control Points (GCPs) and Check Points (CPs) at Sunset Island (a) and Assateague State Park (b).

Table S3.1. Network accuracy estimates per FGDC geospatial positioning accuracy standards at Sunset Island and Assateague State Park.

| Study site | Benchmark name | PID | FGDC (95% conf, cm) | | Standard deviation (cm) | | | CorrNE |
|---|---|---|---|---|---|---|---|---|
| | | | Horiz | Ellip | SD_N | SD_E | SD_h | (unitless) |
| Sunset Island | REEDY 2 AZ MK 3 | HU1256 | 0.48 | 0.90 | 0.21 | 0.18 | 0.46 | -0.067879 |
| Assateague State Park | ASIS HQ1 | DP9253 | 1.00 | 0.88 | 0.48 | 0.28 | 0.45 | -0.006116 |

Table S3.2. Aircraft and camera specifications.

| **Aircraft Specifications** | |
|---|---|
| Type | DJI Phantom 3 Professional |
| Takeoff weight | 1280 g |
| Max flight speed | 16 m/s |
| Max flight time | ≈12 min |
| Horizontal hovering accuracy | ±0.3 ÷ 1.5 m |
| Vertical hovering accuracy | ±0.1 ÷ 0.5 m |
| **Camera Specifications** | |
| Name | MicaSense RedEdge-M |
| Type | RGB + NIR |
| Focal length | 3.6 mm |
| 35 mm equiv. focal length | 20 mm |
| Image resolution | 1280 × 960 |
| Field of view | 84° |
| GSD at 40 m altitude | ≈1.8 cm |

Table S3.3. Residuals for four drone flights at Sunset Island and Assateague State Park.

| | | | | | | |
|---|---|---|---|---|---|---|
| Sunset Island | 2022 April | Average | 0.000 | 0.000 | 0.000 | 1.627 |
| | | Min Difference | -1.926 | -2.808 | -0.122 | 0.266 |
| | | Max Difference | 2.740 | 2.538 | 0.107 | 3.406 |
| | | RMSE | 1.349 | 1.477 | 0.073 | 2.002 |
| | 2023 May | Average | 0.704 | 0.683 | 0.755 | 0.757 |
| | | Min Difference | -0.513 | -0.919 | -0.426 | 0.402 |
| | | Max Difference | 1.741 | 1.812 | 2.406 | 3.197 |
| | | RMSE | 0.853 | 0.890 | 1.030 | 1.607 |
| Assateague State Park | 2022 April | Average | -0.001 | 0.001 | -0.015 | 1.865 |
| | | Min Difference | -1.604 | -4.689 | -0.466 | 0.128 |
| | | Max Difference | 5.734 | 1.440 | 0.755 | 7.422 |
| | | RMSE | 2.124 | 1.721 | 0.368 | 2.758 |
| | 2023 May | Average | 1.282 | 0.604 | 0.182 | 0.460 |
| | | Min Difference | -1.970 | -0.717 | -0.252 | 0.653 |
| | | Max Difference | 2.133 | 0.795 | 0.333 | 2.270 |
| | | RMSE | 1.431 | 0.633 | 0.199 | 1.577 |

*A.3. Supporting information for Chapter 4*

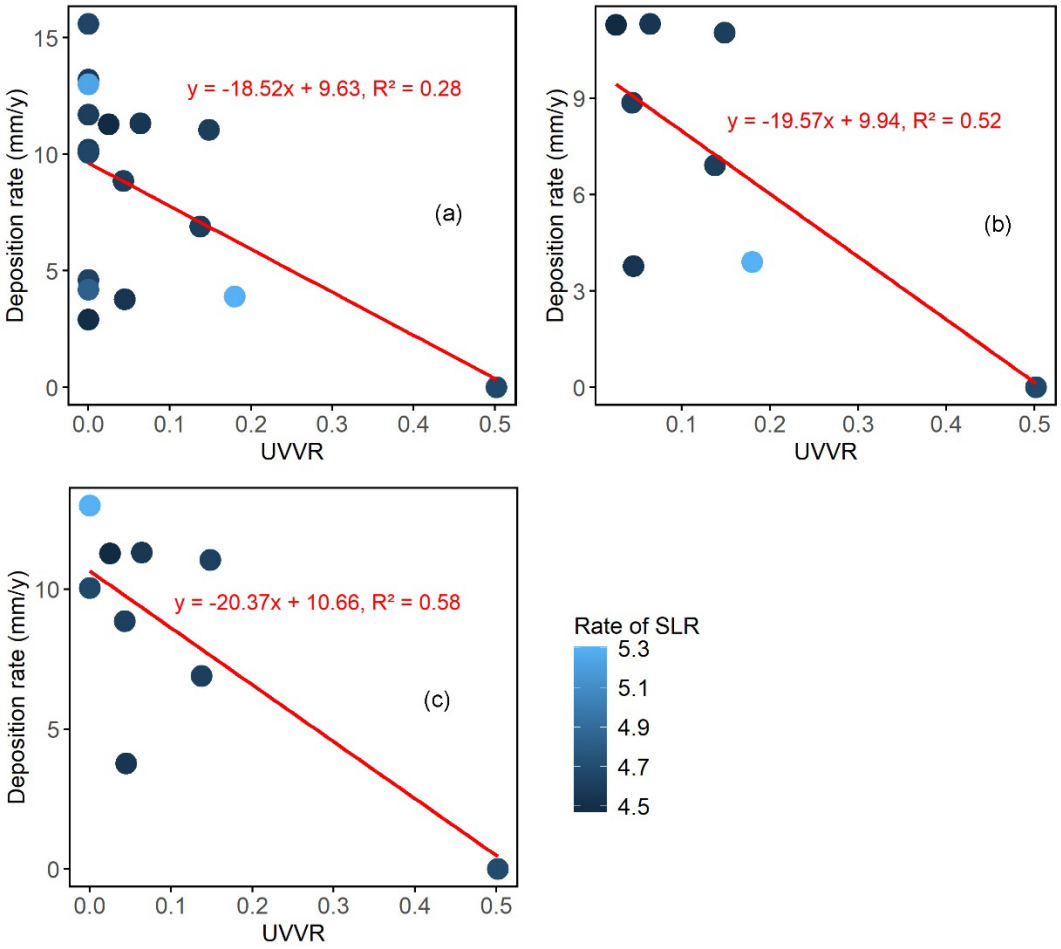


Figure S4.1. (a) Relationship between the Unvegetated/Vegetated Ratio (UVVR) and Sediment Deposition Rate (mm/y) excluding the outlier site, QL. (b) Relationship between UVVR and Sediment Deposition Rate for sites with UVVR > 0. (c) Relationship between UVVR and Sediment Deposition Rate for sites with segmented sills. Different colors indicate different rates of sea level rise (mm/y).

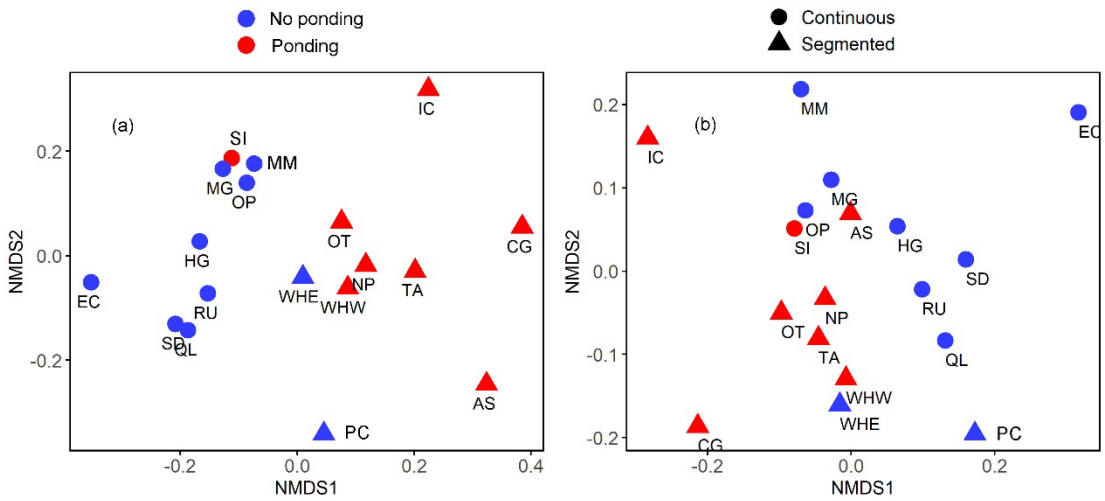


Figure S4.2. (a) Non-metric multi-dimensional scaling analysis for 18 living shorelines with representative variables including Gap/Rock (G/R) ratio, Sand percentage (%), Relative Exposure Index (REI), Stem density (num/m$^2$), and Deposition rate (mm/y); (b) Non-metric multi-dimensional scaling analysis for 18 living shorelines with representative variables including Elevation relative to Mean Sea Level (m), Sand percentage (%), Relative Exposure Index (REI), Stem density (num/m$^2$), and Deposition rate (mm/y).

# Bibliography

Alizad, K., Hagen, S.C., Morris, J.T., Bacopoulos, P., Bilskie, M.V., Weishampel, J.F., Medeiros, S.C., 2016. A coupled, two-dimensional hydrodynamic-marsh model with biological feedback. Ecological Modelling 327, 29–43.

Arkema, K.K., Guannel, G., Verutes, G., Wood, S.A., Guerry, A., Ruckelshaus, M., Kareiva, P., Lacayo, M., Silver, J.M., 2013. Coastal habitats shield people and property from sea-level rise and storms. Nature Climate Change 3, 913–918.

Baptist, M.J., 2005. Modelling Floodplain Biogeomorphology. Ph.D. thesis. Delft University of Technology ISBN 90-407-2582-9.

Baptist, M.J., Babovic, V., Rodríguez Uthurburu, J., Keijzer, M., Uittenbogaard, R.E., Mynett, A., Verwey, A., 2007. On inducing equations for vegetation resistance. Journal of Hydraulic Research 45, 435–450.

Bertness, M.D., Ellison, A.M., 1987. Determinants of pattern in a New England salt marsh plant community. Ecological monographs 57, 129–147.

Bilkovic, D.M., Mitchell, M., Mason, P., Duhring, K., 2016. The role of living shorelines as estuarine habitat conservation strategies. Coastal Management 44, 161–174. https://doi.org/10.1080/08920753.2016.1160201

Bilkovic, D.M., Mitchell, M.M., 2013. Ecological tradeoffs of stabilized salt marshes as a shoreline protection strategy: Effects of artificial structures on macrobenthic assemblages. Ecological Engineering 61, 469–481. https://doi.org/10.1016/j.ecoleng.2013.10.011

Booij, N., Ris, R.C., Holthuijsen, L.H., 1999. A third-generation wave model for coastal regions: 1. Model description and validation. Journal of Geophysical Research: Oceans 104, 7649–7666.

Borcard, D., Gillet, F., Legendre, P., 2018. Numerical Ecology with R, Use R! Springer International Publishing, Cham. https://doi.org/10.1007/978-3-319-71404-2

Boynton, W.R., Murray, L., Hagy, J.D., Stokes, C., Kemp, W.M., 1996. A comparative analysis of eutrophication patterns in a temperate coastal lagoon. Estuaries 19, 408–421.

Castagno, K.A., Jiménez-Robles, A.M., Donnelly, J.P., Wiberg, P.L., Fenster, M.S., Fagherazzi, S., 2018. Intense storms increase the stability of tidal bays. Geophysical Research Letters 45, 5491–5500.

Chesapeake Bay Foundation, 2007. Living Shorelines for the Chesapeake Bay Watershed, Annapolis, MD: Chesapeake Bay Foundation.

Chuang, W.-S., Boicourt, W.C., 1989. Resonant seiche motion in the Chesapeake Bay. Journal of Geophysical Research: Oceans 94, 2105–2110.

Coleman, D.J., Ganju, N.K., Kirwan, M.L., 2020. Sediment delivery to a tidal marsh platform is minimized by source decoupling and flux convergence. Journal of Geophysical Research: Earth Surface 125, e2020JF005558.

Currin, C., Davis, J., Baron, L.C., Malhotra, A., Fonseca, M., 2015. Shoreline change in the New River estuary, North Carolina: rates and consequences. Journal of Coastal Research 315, 1069–1077. https://doi.org/10.2112/JCOASTRES-D-14-00127.1

Currin, C.A., 2019. Living Shorelines for Coastal Resilience, in: Coastal Wetlands. Elsevier, pp. 1023–1053. https://doi.org/10.1016/B978-0-444-63893-9.00030-7

Defne, Z., Aretxabaleta, A.L., Ganju, N.K., Kalra, T.S., Jones, D.K., Smith, K.E.L., 2020. A geospatially resolved wetland vulnerability index: Synthesis of physical drivers. Plos One 15. https://doi.org/10.1371/journal.pone.0228504

Deltares, 2014. Delft3D-FLOW user manual (Version: 3.15. 34158): Simulation of multi-dimensional hydrodynamic flows and transport phenomena, including sediments.

Dolan, R., Lins, H.F., Stewart, J., 1980. Geographical analysis of Fenwick Island, Maryland, a middle Atlantic coast barrier island. US Government Printing Office.

Donatelli, C., Zhang, X., Ganju, N.K., Aretxabaleta, A.L., Fagherazzi, S., Leonardi, N., 2020. A nonlinear relationship between marsh size and sediment trapping capacity compromises salt marshes' stability. Geology 48, 966–970. https://doi.org/10.1130/g47131.1

Dugan, J.E., Airoldi, L., Chapman, M.G., Walker, S.J., Schlacher, T., Wolanski, E., McLusky, D., 2011. 8.02-Estuarine and coastal structures: environmental effects, a focus on shore and nearshore structures. Treatise on Estuarine and Coastal Science 8, 17–41.

Ezer, T., 2023. Sea level acceleration and variability in the Chesapeake Bay: past trends, future projections, and spatial variations within the Bay. Ocean Dynamics 73, 23–34. https://doi.org/10.1007/s10236-022-01536-6

Fagherazzi, S., Mariotti, G., Wiberg, P., McGlathery, K., 2013. Marsh collapse does not require sea level rise. Oceanography 26, 70–77. https://doi.org/10.5670/oceanog.2013.47

Firth, L.B., Thompson, R.C., Bohn, K., Abbiati, M., Airoldi, L., Bouma, T.J., Bozzeda, F., Ceccherelli, V.U., Colangelo, M.A., Evans, A., 2014. Between a rock and a hard place: Environmental and engineering considerations when designing coastal defence structures. Coastal Engineering 87, 122–135.

Fleri, J.R., Lera, S., Gerevini, A., Staver, L., Nardin, W., 2019. Empirical observations and numerical modelling of tides, channel morphology, and vegetative effects on accretion in a restored tidal marsh. Earth Surface Processes and Landforms 44, 2223–2235. https://doi.org/10.1002/esp.4646

Fonseca, M., Whitfield, P.E., Kelly, N.M., Bell, S.S., 2002. Modeling seagrass landscape pattern and associated ecological attributes. Ecological Applications 12, 218–237.

French, J.R., 2008. Hydrodynamic modelling of estuarine flood defence realignment as an adaptive management response to sea-level rise. Journal of Coastal Research 1–12.

Ganju, N., Defne, Z., Kirwan, M., Fagherazzi, S., D'Alpaos, A., Carniello, L., 2017. Spatially integrative metrics reveal hidden vulnerability of microtidal salt marshes. Nature Communications 8, 14156. https://doi.org/10.1038/ncomms14156

Ganju, N., Kroeger, K., Kirwan, M., Dickhudt, P., Guntenspergen, G., Cahoon, D., 2015. Sediment transport based metrics of wetland stability. Geophysical Research Letters 42, n/a-n/a. https://doi.org/10.1002/2015GL065980

Ganju, N., Testa, J., Suttles, S., Aretxabaleta, A., 2020. Spatiotemporal variability of light attenuation and net ecosystem metabolism in a back-barrier estuary. Ocean Science 16, 593–614.

Ganju, N.K., Couvillion, B.R., Defne, Z., Ackerman, K.V., 2022. Development and Application of Landsat-Based Wetland Vegetation Cover and UnVegetated-Vegetated Marsh Ratio (UVVR) for the Conterminous United States. Estuaries and Coasts. https://doi.org/10.1007/s12237-022-01081-x

Ganju, N.K., Defne, Z., Fagherazzi, S., 2020. Are elevation and open-water conversion of salt marshes connected? Geophysical Research Letters 47, e2019GL086703.

Ganju, N.K., Defne, Z., Fagherazzi, S., 2020. Are elevation and open-water conversion of salt marshes connected? Geophysical Research Letters 47. https://doi.org/10.1029/2019gl086703

Ganju, N.K., Suttles, S.E., Beudin, A., Nowacki, D.J., Miselis, J.L., Andrews, B.D., 2017. Quantification of Storm-Induced Bathymetric Change in a Back-Barrier Estuary. Estuaries and Coasts 40, 22–36.

Gittman, R.K., Fodrie, F.J., Popowich, A.M., Keller, D.A., Bruno, J.F., Currin, C.A., Peterson, C.H., Piehler, M.F., 2015. Engineering away our natural defenses: an analysis of shoreline hardening in the US. Frontiers in Ecology and the Environment 13, 301–307.

Gittman, R.K., Peterson, C.H., Currin, C.A., Joel Fodrie, F., Piehler, M.F., Bruno, J.F., 2016a. Living shorelines can enhance the nursery role of threatened estuarine habitats. Ecological Applications 26, 249–263. https://doi.org/10.1890/14-0716

Gittman, R.K., Scyphers, S.B., Smith, C.S., Neylan, I.P., Grabowski, J.H., 2016b. Ecological consequences of shoreline hardening: a meta-analysis. BioScience 66, 763–773.

Gong, W., Shen, J., Cho, K.-H., Wang, H.V., 2009. A numerical model study of barotropic subtidal water exchange between estuary and subestuaries (tributaries) in the Chesapeake Bay during northeaster events. Ocean Modelling 26, 170–189.

Hardaway Jr, C.S., Byrne, R.J., 1999. Shoreline management in Chesapeake Bay.

Hardaway Jr, C.S., Duhring, K., 2010. Living shoreline design guidelines for shore protection in Virginia's estuarine environments.

Hardaway Jr, C.S., Duhring, K., 2010. Living shoreline design guidelines for shore protection in Virginia's estuarine environments.

Hardaway Jr, C.S., Milligan, D.A., Duhring, K., Wilcox, C.A., 2017. Living shoreline design guidelines for shore protection in Virginia's estuarine environments. Gloucester Point, VA: Virginia Institute of Marine Science.

Hardaway Jr., A.R.J.B., 1999. Shoreline management In Chesapeake Bay. https://doi.org/10.21220/V5DB1X

Hardaway Jr., C.S., 1991. Chesapeake Bay shoreline study: Headland breakwaters and pocket beaches for shoreline erosion control final report. https://doi.org/10.21220/V5GB05

Hardaway Jr., C.S., 2017. Living Shoreline Design Guidelines for Shore Protection in Virginia's Estuarine Environments.

Hardaway, C.S., Milligan, D.A., Duhring, K., 2010. Living shoreline design guidelines.

Hardaway, Jr., C.S., Gunn, J.R., 2002. Shoreline protection: Design guidelines for pocket beaches in Chesapeake Bay, USA, in: Carbonate Beaches 2000. Presented at the First International Symposium on Carbonate Sand Beaches, American Society of Civil Engineers, Westin Beach Resort, Key Largo, Florida, United States, pp. 126–139. https://doi.org/10.1061/40640(305)10

Hobbs, C.H., Halka, J.P., Kerhin, R.T., Carron, M.J., 1992. Chesapeake Bay sediment budget. Journal of Coastal Research 8, 292–300.

Holmquist, J.R., Windham-Myers, L., 2022. A conterminous USA-scale map of relative tidal marsh elevation. Estuaries and Coasts 45, 1596–1614. https://doi.org/10.1007/s12237-021-01027-9

Hopkinson, C.S., Morris, J.T., Fagherazzi, S., Wollheim, W.M., Raymond, P.A., 2018. Lateral marsh edge erosion as a source of sediments for vertical marsh accretion. Journal of Geophysical Research: Biogeosciences 123, 2444–2465. https://doi.org/10.1029/2017JG004358

Isdell, R.E., Chambers, R.M., Bilkovic, D.M., Leu, M., 2015. Effects of terrestrial–aquatic connectivity on an estuarine turtle. Diversity and Distributions 21, 643–653.

Kang, X., Xia, M., 2020. The study of the hurricane-induced storm surge and bay-ocean exchange using a nesting model. Estuaries and Coasts 43, 1610–1624. https://doi.org/10.1007/s12237-020-00695-3

Kang, X., Xia, M., Pitula, J.S., Chigbu, P., 2017. Dynamics of water and salt exchange at Maryland Coastal Bays. Estuarine, Coastal and Shelf Science 189, 1–16.

Karimpour, A., Chen, Q., 2017. Wind wave analysis in depth limited water using OCEANLYZ, A MATLAB toolbox. Computers & Geosciences 106, 181–189.

Kirezci, E., Young, I.R., Ranasinghe, R., Muis, S., Nicholls, R.J., Lincke, D., Hinkel, J., 2020. Projections of global-scale extreme sea levels and resulting episodic coastal flooding over the 21st Century. Scientific Reports 10, 1–12.

Kissas, G., Yang, Y., Hwuang, E., Witschey, W.R., Detre, J.A., Perdikaris, P., 2020. Machine learning in cardiovascular flows modeling: Predicting arterial blood pressure from non-invasive 4D flow MRI data using physics-informed neural networks. Computer Methods in Applied Mechanics and Engineering 358, 112623.

Knutson, P.L., Brochu, R.A., Seelig, W.N., Inskeep, M., 1982. Wave damping in Spartina alterniflora marshes. Wetlands 2, 87–104.

Koch, E.W., Barbier, E.B., Silliman, B.R., Reed, D.J., Perillo, G.M., Hacker, S.D., Granek, E.F., Primavera, J.H., Muthiga, N., Polasky, S., 2009. Non-linearity in ecosystem services: temporal and spatial variability in coastal protection. Frontiers in Ecology and the Environment 7, 29–37.

Koontz, E., 2025. Evaluating the performance, stability, and impact of three living shoreline designs on submersed aquatic vegetation (SAV) in mesohaline Chesapeake Bay. [Master's thesis, University of Maryland, College Park]. *In prep.*

Lee, S.B., Li, M., Zhang, F., 2017. Impact of sea level rise on tidal range in Chesapeake and Delaware Bays. Journal of Geophysical Research: Oceans 122, 3917–3938. https://doi.org/10.1002/2016JC012597

Leone, A., Tahvildari, N., 2023. Comparison of Spectral Wave Dissipation by Two Living Shoreline Features in a Sheltered Tidal Bay. Estuaries and Coasts 46, 323–335.

Lera, S., Nardin, W., Sanford, L., Palinkas, C., Guercio, R., 2019. The impact of submersed aquatic vegetation on the development of river mouth bars. Earth Surface Processes and Landforms 44, 1494–1506.

Lesser, G.R., Roelvink, J. v, van Kester, J.T.M., Stelling, G.S., 2004. Development and validation of a three-dimensional morphological model. Coastal engineering 51, 883–915.

Li, X., Leonardi, N., Plater, A.J., 2019. Wave-driven sediment resuspension and salt marsh frontal erosion alter the export of sediments from macro-tidal estuaries. Geomorphology 325, 17–28. https://doi.org/10.1016/j.geomorph.2018.10.004

Li, X., Plater, A., Leonardi, N., 2018. Modelling the transport and export of sediments in macrotidal estuaries with eroding salt marsh. Estuaries and Coasts 41, 1551–1564. https://doi.org/10.1007/s12237-018-0371-1

Lin, W., Sanford, L.P., Suttles, S.E., 2002. Wave measurement and modeling in Chesapeake Bay. Continental Shelf Research 22, 2673–2686.

Liu, Y., MacCready, P., Hickey, B.M., Dever, E.P., Kosro, P.M., Banas, N.S., 2009. Evaluation of a coastal ocean circulation model for the Columbia River plume in summer 2004. Journal of Geophysical Research: Oceans 114.

Liu, Z., Fagherazzi, S., Cui, B., 2021. Success of coastal wetlands restoration is driven by sediment availability. Communications Earth & Environment 2, 44. https://doi.org/10.1038/s43247-021-00117-7

Mariotti, G., Canestrelli, A., 2017. Long-term morphodynamics of muddy backbarrier basins: Fill in or empty out? Water Resources Research 53, 7029–7054. https://doi.org/10.1002/2017WR020461

Mariotti, G., Carr, J., 2014. Dual role of salt marsh retreat: Long-term loss and short-term resilience. Water Resources Research 50, 2963–2974.

Medeiros, S., Hagen, S., Weishampel, J., Angelo, J., 2015. Adjusting lidar-derived digital terrain models in coastal marshes based on estimated aboveground biomass density. Remote Sensing 7, 3507–3525.

Millennium ecosystem assessment, M.E.A., 2005. Ecosystems and human well-being. Island press Washington, DC.

Miller, J.K., Kerr, L., Bredes, A., 2022. Living Shorelines Engineering Guidelines 2022 Update.

Miller, J.K., Kerr, L., Bredes, A., 2022. Living shorelines engineering guidelines. Stevens institute of Technology.

Miller, J.K., Rella, A., Williams, A., Sproule, E., 2015. Living shorelines engineering guidelines. Stevens institute of Technology.

Möller, I., Kudella, M., Rupprecht, F., Spencer, T., Paul, M., van Wesenbeeck, B.K., Wolters, G., Jensen, K., Bouma, T.J., Miranda-Lange, M., Schimmels, S., 2014. Wave attenuation over coastal salt marshes under storm surge conditions. Nature Geoscience 7, 727–731.

Nardin, W., Edmonds, D.A., 2014. Optimum vegetation height and density for inorganic sedimentation in deltaic marshes. Nature Geoscience 7, 722–726. https://doi.org/10.1038/NGEO2233

Nardin, W., Fagherazzi, S., 2018. The role of waves, shelf slope, and sediment characteristics on the development of erosional chenier plains. Geophysical Research Letters 45, 8435–8444. https://doi.org/10.1029/2018gl078694

Nardin, W., Larsen, L., Fagherazzi, S., Wiberg, P., 2018. Tradeoffs among hydrodynamics, sediment fluxes and vegetation community in the Virginia Coast Reserve, USA. Estuarine, Coastal and Shelf Science 210, 98–108. https://doi.org/10.1016/j.ecss.2018.06.009

Nardin, W., Lera, S., Nienhuis, J., 2020. Effect of offshore waves and vegetation on the sediment budget in the Virginia Coast Reserve (VA). Earth Surface Processes and Landforms 45, 3055–3068.

Nardin, W., Mariotti, G., Edmonds, D.A., Guercio, R., Fagherazzi, S., 2013. Growth of river mouth bars in sheltered bays in the presence of frontal waves. Journal

of Geophysical Research: Earth Surface 118, 872–886. https://doi.org/10.1002/jgrf.20057

Nardin, W., Taddia, Y., Quitadamo, M., Vona, I., Corbau, C., Franchi, G., Staver, L.W., Pellegrinelli, A., 2021. Seasonality and characterization mapping of restored tidal marsh by NDVI imageries coupling UAVs and multispectral camera. Remote Sensing 13, 4207. https://doi.org/10.3390/rs13214207

National Climatic Data Center, 1976. Maryland's climate. CLIMATOGRAPHY OF THE UNITED STATES NO. 60.

Nordstrom, K.F., Jackson, N.L., 2012. Physical processes and landforms on beaches in short fetch environments in estuaries, small lakes and reservoirs: a review. Earth-Science Reviews 111, 232–247.

Olsen, C.R., Larsen, I.L., Lowry, P.D., Cutshall, N.H., Nichols, M.M., 1986. Geochemistry and deposition of 7Be in river-estuarine and coastal waters. Journal of Geophysical Research: Oceans 91, 896–908.

Ondrusek, M., Stengel, E., Kinkade, C.S., Vogel, R.L., Keegstra, P., Hunter, C., Kim, C., 2012. The development of a new optical total suspended matter algorithm for the Chesapeake Bay. Remote Sensing of Environment 119, 243–254.

Palinkas, C.M., Bolton, M.C., Staver, L.W., 2023. Long-term performance and impacts of living shorelines in mesohaline Chesapeake Bay. Ecological Engineering 190, 106944. https://doi.org/10.1016/j.ecoleng.2023.106944

Palinkas, C.M., Engelhardt, K.A.M., 2016. Spatial and temporal patterns of modern (similar to 100 yr) sedimentation in a tidal freshwater marsh: Implications for

future sustainability. Limnology And Oceanography 61, 132–148. https://doi.org/10.1002/lno.10202

Palinkas, C.M., Engelhardt, K.A.M., Cadol, D., 2013. Evaluating physical and biological influences on sedimentation in a tidal freshwater marsh with Be-7. Estuarine Coastal And Shelf Science 129, 152–161. https://doi.org/10.1016/j.ecss.2013.05.022

Palinkas, C.M., Sanford, L.P., Koch, E.W., 2018. Influence of shoreline stabilization structures on the nearshore sedimentary environment in mesohaline Chesapeake Bay. Estuaries and Coasts 41, 952–965. https://doi.org/10.1007/s12237-017-0339-6

Patrick, C.J., Weller, D.E., Li, X., Ryder, M., 2014. Effects of shoreline alteration and other stressors on submerged aquatic vegetation in subestuaries of Chesapeake Bay and the Mid-Atlantic Coastal Bays. Estuaries and Coasts 37, 1516–1531. https://doi.org/10.1007/s12237-014-9768-7

Paul, M., Rupprecht, F., Möller, I., Bouma, T.J., Spencer, T., Kudella, M., Wolters, G., Van Wesenbeeck, B.K., Jensen, K., Miranda-Lange, M., Schimmels, S., 2016. Plant stiffness and biomass as drivers for drag forces under extreme wave loading: A flume study on mimics. Coastal Engineering 117, 70–78.

Polk, M.A., Eulie, D.O., 2018. Effectiveness of living shorelines as an erosion control method in North Carolina. Estuaries and Coasts 41, 2212–2222. https://doi.org/10.1007/s12237-018-0439-y

Polk, M.A., Gittman, R.K., Smith, C.S., Eulie, D.O., 2022. Coastal resilience surges as living shorelines reduce lateral erosion of salt marshes. Integrated Environmental Assessment and Management 18, 82–98.

Priest III, W.I., 2006. Design criteria for tidal wetlands. Management, Policy, Science, and Engineering of Nonstructural Erosion Control in the Chesapeake Bay 25–32.

Pritchard, D.W., 1960. Salt balance and exchange rate for Chincoteague Bay. Chesapeake Science 1, 48–57.

Prosser, D.J., Jordan, T.E., Nagel, J.L., Seitz, R.D., Weller, D.E., Whigham, D.F., 2018. Impacts of coastal land use and shoreline armoring on estuarine ecosystems: an introduction to a special issue. Estuaries and Coasts 41, 2–18. https://doi.org/10.1007/s12237-017-0331-1

Raposa, K.B., Wasson, K., Smith, E., Crooks, J.A., Delgado, P., Fernald, S.H., Ferner, M.C., Helms, A., Hice, L.A., Mora, J.W., 2016. Assessing tidal marsh resilience to sea-level rise at broad geographic scales with multi-metric indices. Biological Conservation 204, 263–275.

Rupprecht, F., Möller, I., Evans, B., Spencer, T., Jensen, K., 2015. Biophysical properties of salt marsh canopies — Quantifying plant stem flexibility and above ground biomass. Coastal Engineering 100, 48–57.

Russ, E.R., Palinkas, C.M., 2018. Seasonal-scale and decadal-scale sediment-vegetation interactions on the subaqueous Susquehanna River Delta, upper Chesapeake Bay. Estuaries and Coasts 41, 2092–2104. https://doi.org/10.1007/s12237-018-0413-8

Shipman, H., 2009. The geomorphic setting of Puget Sound: implications for shoreline erosion and the impacts of erosion control structures, in: Puget Sound Shorelines and the Impacts of Armoring—Proceedings of a State of the Science Workshop. pp. 19–34.

Shore Protection Manual vol. 1. 1975. Fort Belvoir: US Army Coastal Engineering Research Center.

Smith, C.S., Puckett, B., Gittman, R.K., Peterson, C.H., 2018. Living shorelines enhanced the resilience of saltmarshes to Hurricane Matthew (2016). Ecological Applications 28, 871–877. https://doi.org/10.1002/eap.1722

Smith, C.S., Puckett, B., Gittman, R.K., Peterson, C.H., 2018b. Living shorelines enhanced the resilience of saltmarshes to Hurricane Matthew (2016). Ecological Applications 28, 871–877.

Smith, K.M., 2006. Integrating habitat and shoreline dynamics into living shoreline applications. Management, Policy, Science, and Engineering of Nonstructural Erosion Control in the Chesapeake Bay 9–11.

Stoker, J., Miller, B., 2022. The accuracy and consistency of 3D elevation program data: A systematic analysis. Remote Sensing 14, 940. https://doi.org/10.3390/rs14040940

Sun, L., Palinkas, C.M., Nardin, W., 2024. Marsh boundary degradation into open-water in living shorelines under high-energy conditions. Ecological Engineering 202, 107232.

Sutton-Grier, A.E., Wowk, K., Bamford, H., 2015. Future of our coasts: The potential for natural and hybrid infrastructure to enhance the resilience of our coastal

communities, economies and ecosystems. Environmental Science & Policy 51, 137–148. https://doi.org/10.1016/j.envsci.2015.04.006

Suzuki, T., Zijlema, M., Burger, B., Meijer, M.C., Narayan, S., 2012. Wave dissipation by vegetation with layer schematization in SWAN. Coastal Engineering 59, 64–71.

Taddia, Y., Pellegrinelli, A., Corbau, C., Franchi, G., Staver, L.W., Stevenson, J.C., Nardin, W., 2021. High-resolution monitoring of tidal systems using UAV: a case study on Poplar Island, MD (USA). Remote Sensing 13, 1364.

Temmerman, S., Meire, P., Bouma, T.J., Herman, P.M., Ysebaert, T., De Vriend, H.J., 2013. Ecosystem-based coastal defence in the face of global change. Nature 504, 79–83.

US Army Corps of Engineers, 2002. Coastal Engineering Manual, Washington, D.C.: US Army Corps of Engineers.

van Maanen, B., Coco, G., Bryan, K.R., 2015. On the ecogeomorphological feedbacks that control tidal channel network evolution in a sandy mangrove setting. Proceedings of the Royal society A: Mathematical, physical and engineering sciences 471, 20150115.

Vona, I., Gray, M., Nardin, W., 2020. The impact of submerged breakwaters on sediment distribution along marsh boundaries. Water 12. https://doi.org/10.3390/w12041016

Vona, I., Nardin, W., 2023. Oysters' integration on submerged breakwaters offers new adaptive shoreline protection in low-energy environments in the face of

sea level rise. Journal of Geophysical Research: Earth Surface 128, e2023JF007249. https://doi.org/10.1029/2023JF007249

Vona, I., Palinkas, C.M., Nardin, W., 2021. Sediment exchange between the created saltmarshes of living shorelines and adjacent submersed aquatic vegetation in the Chesapeake Bay. Frontiers in Marine Science 8, 727080. https://doi.org/10.3389/fmars.2021.727080

Wang, H., Capurso, W.D., Chen, Q., Zhu, L., Niemoczynski, L., Snedden, G., 2021. Assessment of wave attenuation, current patterns, and sediment deposition and erosion during winter storms by living shoreline structures in Gandys Beach, New Jersey. US Geological Survey.

Wang, H., Wang, Z., Loftis, J.D., Teng, Y.C., 2013. Hydrodynamic and water quality modeling and TMDL development for Maryland's coastal Bays system. Final report submitted to Maryland Department of the Environment, TMDL Technical Development Program.

Wang, N., Chen, Q., Zhu, L., Wang, H., 2022. Data-driven modeling of wind waves in upper Delaware Bay with living shorelines. Ocean Engineering 257, 111669. https://doi.org/10.1016/j.oceaneng.2022.111669

Warner, J.C., Geyer, W.R., Lerczak, J.A., 2005. Numerical modeling of an estuary: A comprehensive skill assessment. Journal of Geophysical Research: Oceans 110.

Wasson, K., Ganju, N.K., Defne, Z., Endris, C., Elsey-Quirk, T., Thorne, K.M., Freeman, C.M., Guntenspergen, G., Nowacki, D.J., Raposa, K.B., 2019. Understanding tidal marsh trajectories: evaluation of multiple indicators of

marsh persistence. Environmental Research Letters 14, 124073. https://doi.org/10.1088/1748-9326/ab5a94

Wazniak, C., Wells, D., Hall, M., 2004. The Maryland coastal bays ecosystem. Maryland's coastal bays: ecosystem health assessment 1–9.

Wells, D.V., Conkwright, R.D., Hill, J.M., Park, M.J., 1994. The surficial sediments of Assawoman Bay and Isle of Wight Bay in Maryland: Physical and chemical characteristics. Coastal and Estuarine Geology File Report.

Wells, D.V., Hennessee, E.L., Hill, J.M., 2002. Shoreline erosion as a source of sediments and nutrients: Northern Coastal Bays, Maryland. Maryland Geological Survey, Resource Assessment Service.

Wiberg, P.L., Carr, J.A., Safak, I., Anutaliya, A., 2015. Quantifying the distribution and influence of non-uniform bed properties in shallow coastal bays. Limnology and Oceanography: Methods 13, 746–762.

Wiberg, P.L., Fagherazzi, S., Kirwan, M.L., 2020. Improving predictions of salt marsh evolution through better integration of data and models. Annual Review of Marine Science 12, 389–413.

Wiberg, P.L., Taube, S.R., Ferguson, A.E., Kremer, M.R., Reidenbach, M.A., 2019. Wave attenuation by oyster reefs in shallow coastal bays. Estuaries and Coasts 42, 331–347. https://doi.org/10.1007/s12237-018-0463-y

Willmott, C.J., 1981. On the validation of models. Physical Geography 2, 184–194.

Wong, M.C., 2018. Secondary production of macrobenthic communities in seagrass (Zostera marina, Eelgrass) beds and bare soft sediments across differing

environmental conditions in Atlantic Canada. Estuaries and Coasts 41, 536–548. https://doi.org/10.1007/s12237-017-0286-2

Xu, Y., Kalra, T.S., Ganju, N.K., Fagherazzi, S., 2021. Modeling the dynamics of salt marsh formation (preprint). Environmental Sciences. https://doi.org/10.1002/essoar.10507835.1

Zhu, L., Chen, Q., Wang, H., Capurso, W., Niemoczynski, L., Hu, K., Snedden, G., 2020. Field observations of wind waves in upper Delaware Bay with living shorelines. Estuaries and Coasts 43, 739–755. https://doi.org/10.1007/s12237-019-00670-7

Zhu, L., Chen, Q., Wang, H., Wang, N., Hu, K., Capurso, W., Niemoczynski, L., Snedden, G., 2023. Modeling surface wave dynamics in upper Delaware Bay with living shorelines. Ocean Engineering 284, 115207. https://doi.org/10.1016/j.oceaneng.2023.115207

Zhu, Q., Wiberg, P.L., 2022. The importance of storm surge for sediment delivery to microtidal marshes. Journal of Geophysical Research: Earth Surface 127. https://doi.org/10.1029/2022JF006612

Zhu, Q., Wiberg, P.L., 2024. Effects of seasonal variations in seagrass density and storms on sediment retention and connectivity between subtidal flats and intertidal marsh. Journal of Geophysical Research: Biogeosciences 129, e2023JG007785. https://doi.org/10.1029/2023JG007785

Zhu, Q., Wiberg, P.L., Reidenbach, M.A., 2021. Quantifying seasonal seagrass effects on flow and sediment dynamics in a back-barrier bay. Journal of Geophysical Research: Oceans 126, e2020JC016547.